Localization of Subsurface Targets using Optimal Maneuvers of Seismic Sensors

A Thesis
Presented to
The Academic Faculty

by

Mubashir Alam

In Partial Fulfillment
of the Requirements for the Degree
Doctor of Philosophy

School of Electrical and Computer Engineering
Georgia Institute of Technology
August 2006

Localization of Subsurface Targets using Optimal Maneuvers of Seismic Sensors

Approved by:

Dr. James H. McClellan, Chair
School of Electrical and Computer Engineering
Georgia Institute of Technology

Dr. Thomas E. Michaels
School of Electrical and Computer Engineering
Georgia Institute of Technology

Dr. Waymond R. Scott
School of Electrical and Computer Engineering
Georgia Institute of Technology

Dr. Laurence J. Jacobs
School of Civil Engineering
Georgia Institute of Technology

Dr. Russell M. Mersereau
School of Electrical and Computer Engineering
Georgia Institute of Technology

Date Approved: May 3, 2006

Abu Aur Ami Keh Naam....

This dissertation is dedicated to my parents, specially to my late father. Thank you for your love, affection and care, in good times and in bad times.

And also to rest of my family.

Thank you for your love, encouragement, and support.

ACKNOWLEDGEMENTS

It has been a long journey for me in the completion of this thesis. I was helped and influenced by many persons along the way. First of all, i would like to thank my advisor Dr James McClellan for giving me the freedom and support to discover the topic. Even after accomplishing so much, he is still the source of encouragement for many of his graduate students like me. His vast knowledge and insights has helped a lot in defining the work in this thesis. I also like to thank him for giving financial support for my studies, and for my travel expenses to so many conferences. Also, i want to mention the help and encouragement which i got from Dr Waymond Scott in understanding the seismic wave physics. His comments always helped me in improving my work. He was also on my dissertation committee. I would also like to thank other committee members, namely Dr. Russell M. Mersereau, Dr Thomas Michaels and Dr Laurence Jacobs, for taking time out of there busy schedule.

Also, special thanks to our project team, with whom i have the interaction for last three years during our weekly project meetings. I would like to thank Dr Gregg Larson, for generating all the experimental data used for examples in this thesis. His understanding of the data always helped me a lot. I would also like to thank Phelam Norville for generating the numerical data, and also in his comments. Special thanks to Dr Volkan Cevher for helping me in the developments of algorithm for optimal maneuvering. I would also like to thank other members of our research group, some of whom graduated and some are still on there way of completion. They are: Dr Ryan Hersey, Dr Yeo-Sun Yoon, Dr Qiang Lee, Sam Lee, Ali Cafer Gurbuz, Milind Borkar, Faisal Shah, Rajbabu Velmurugan and Yeongseon Lee. Best of luck to all of you, in completing your thesis. I was lucky to be part of CSIP (Center for Signal and Image Processing), during my stay here at Georgia Tech. The staff and other graduate students in this group are always so helpful.

During my long stay here in Atlanta and Georgia Tech, i was lucky to be in company of so many friends and a long list of room mates. I always learned a lot from them.

Thanks for being there in time of need. From Pakistani community i would like to thank Fawad Alam Khan, Zackaria Ajmal, Ambreen Zackaria, Muhammad Jamshid, Tariq Ali, Taimoor Saleem, Haris Rashid and my currents and former room-mates Mudassar Nisar, Irfan Ahmed, Ibrar-ul-Haque and Adnan Anayat.I would also like to thank Waseem Khan and Muhammad Intikhab Alam for helping me to settle down in the beginning. I would also like to thank long list of my German and other room-mates, namely Michael Decker, Rudiger Benz, Jochen Rieber, Mathias Maess, Michael Junge, Hemal Shah, Andy Song and many more. I shall always cherish there company. We have spend many evenings together either cooking, watching football and basketball games, or just talking. Thanks to all of you for making my stay here in Atlanta so memorable.

I would also like to thank Ministry of Education, Govt of Pakistan, for funding the initial three years of my studies. I am also very grateful to Dr David Hertling for providing me Graduate Teaching assistant for many years. I would also like to thank all of my former teachers, from whom i had learned a lot.

However, i would not be here and accomplished so much without such loving and caring parents, specially my late father (may rest in peace). Even though he is not here to share this with me, but his love, encouragement and support was and will always with me. I know i had the support and prayers of my mother with me all the time. I would also like to thank the rest of my family. Thank you for your love, care, prayers and support.

TABLE OF CONTENTS

LIST OF TABLES

LIST OF FIGURES

SUMMARY

The use of seismic waves to detect subsurface targets such as landmines is a very promising technology compared to existing methods like Ground Penetrating Radar (GPR) and Electromagnetic Induction (EMI) sensing. The fact that seismic waves induce resonance in man-made targets, and hence more scattering, gives this method a natural ability to discriminate landmines from common types of clutter like rocks, wood, etc. Reflection and resonance from the targets can be used in imaging to detect the location of targets. However, existing methods require a large number of measurements for imaging and detection, which are expensive and time consuming. To reduce the number of measurements and enable faster detections, a new sensing strategy is proposed based on optimally maneuvering sensors. The system would operate in two main modes. In search mode, the goal would be to move on top of a target using the minimum number of measurements. Once the target is found, the system would switch to a detection mode to make its final decision. The seismic sensor system is an active system, where a seismic source generates the probing pulse. The waves reflected from buried targets are collected by an array of sensors placed on the surface, and then an imaging algorithm is used to estimate the target position. The performance bounds for this position estimate are derived in terms of the Fisher information matrix (FIM). This matrix gives the dependence of the target position estimate on the array position. Based on the FIM, the next optimal array position is determined by using the theory of optimal experiments. The next array position will be the one that reduces the uncertainty of the target position estimate the most. The whole array is moved to this new position, where the same steps are repeated. In this way, the target can be localized in a few iterations.

CHAPTER I

INTRODUCTION

1.1 Origin of the Problem

The detection of buried landmines and subsurface structures has been investigated at Georgia Tech and elsewhere in recent years using seismic waves [21, 58, 62–64]. A seismic wave launched from a source travels through the soil and interacts with buried targets. The detection system exploits the large difference between the elastic properties of a mine and the surrounding soil. This difference causes seismic wave interactions in the vicinity of the mine to be quite distinctive. This distinctive behavior can be used to locate the buried landmines and also distinguish them from common types of clutter in the soil. Seismic waves that propagate in the medium can be divided into two main types, surface waves and body waves. The main surface waves are Rayleigh and Love waves. Body waves, such as shear and compressional waves, are present inside the medium. Rayleigh waves can be measured by placing the sensors on the surface. The interaction of Rayleigh waves with near-surface buried targets will be utilized in the detection.

Seismic techniques have been shown to be effective, even in the detection of low-metal anti-personnel (AP) mines [62, 63], because mines have mechanical properties that are significantly different from the surrounding soil. For example, the shear wave velocity is approximately 20 times higher in the explosive and plastics used in typical mines than in the surrounding soil [61]. In addition, mines are complex mechanical structures with a flexible case, a trigger assembly, air pockets, etc. This complex structure gives rise to structural resonances in mines, which are quite different from the response from clutter such as rocks. This structural resonance also gives rise to many reflections from a mine. The resonances and reflections can be used together to form an effective imaging algorithm to locate the mines [11].

The range of burial depths typically associated with anti-personnel (AP) and anti-tank

(AT) mines is 1 to 10 cm below the Earth's surface. AT mines are typically larger and more deeply buried than AP mines. These characteristics make classical seismic techniques ill-suited to the landmine detection problem, because classical seismic techniques are used for imaging deeper targets. The deeper targets are also much bigger than landmines and the seismic survey performed with these techniques is deployed over a large area. These techniques usually involve the generation and detection of bulk waves (shear or compressional waves) in the earth [19]. Surface-guided (Rayleigh) waves are problematic for classical seismic measurements because their displacements decay exponentially away from the Earth's surface. These waves do not interrogate the soil deeper than a few wavelengths, even though they have large surface displacement. However, these same features make the Rayleigh wave an excellent interrogation signal for detecting landmines. Targets at various depths can be detected by varying the frequency content of the interrogating signal.

The initial attempt to build a seismic landmine detection system using a pulse-echo scheme was reported in [64]. The seismic source generates a probing pulse, which travels through the soil, interacts with targets, and then gets reflected. This reflection can be measured by sensors placed on the surface. The collected data is then processed by a back-propagation algorithm to image and detect the location of mines. Other researchers have argued that instead of using this kind of setup, it's better to measure seismic motion at the mine [58,63]. The current prototype system is based on this idea, and it offers three distinct advantages over a remote-receiving array technique. First, since the reflected waves do not have to travel to a receiving array, one half of the geometric spreading and attenuation is eliminated. Second, problems caused by changes in the propagation properties of the intervening medium are mitigated, which reduces the uncertainty in the location estimate of the target. Third, it allows measurement directly above the buried mines for detecting the resonance.

The next sections describe the existing prototype system, the imaging algorithm used to localize the landmines, and some limitations of the existing processing.

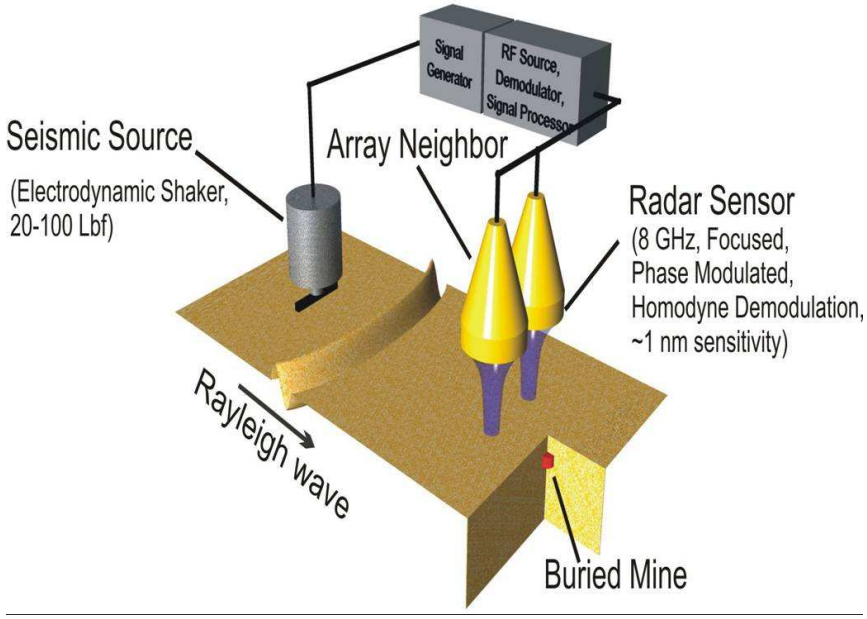

Figure 1: Prototype system using two radar sensors (other kinds of sensors can also be used) [62, 63].

1.1.1 Prototype Seismic Landmine Detection System

The mine detection system that has been used in experiments is depicted in Figs. 1 and 2. The system consists of a stationary seismic source and a movable receiving array [1] [62, 63]. The source is an electrodynamic shaker that has been coupled to the ground by a narrow foot and has been designed to generate Rayleigh waves. The receivers shown in Fig. 1 are radar sensors, which are non-ground-contacting sensors, capable of measuring the soil displacements of the order of 1 nm. This sensitivity is more than sufficient to measure the surface displacements of seismic waves that are on the order of 1 μm. The radar sensor is one type of sensors used for measuring soil displacements; however, other sensors are also used, including ground-contacting accelerometers, ultrasonic sensors, and passive air-acoustic sensors. Most of the experimental data used for the algorithms in this thesis are measured by radar sensor and accelerometers.

Laboratory testing has been conducted in a wedge-shaped tank, depicted in Fig. 3, filled

[1] Waymond Scott and Gregg Larson are creators of Figs. 1, 2 and 3

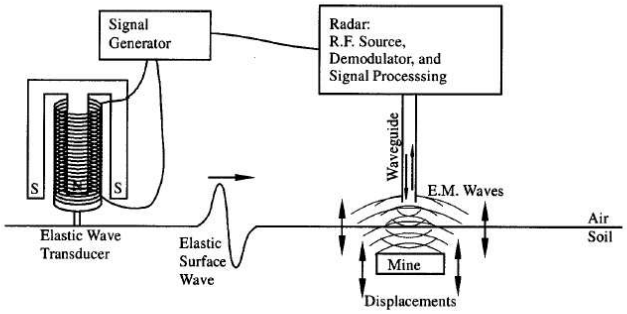

Figure 2: Configuration of seismic mine detection system [63].

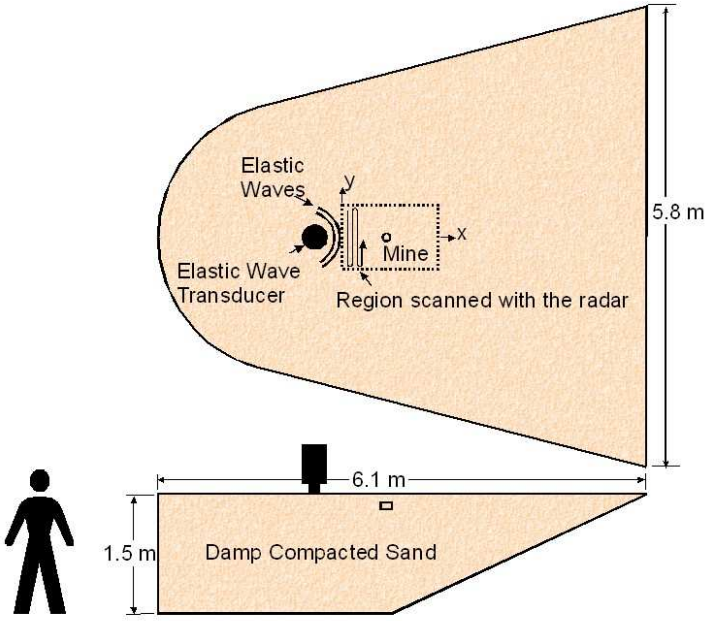

Figure 3: Experimental soil tank facility [63].

with damp compacted sand to simulate soil. The seismic source is located as indicated in Fig. 3 and is bidirective toward the search area and the back of the wall. Damp, compacted sand was chosen as a soil substitute because it can be dug up, refilled, and repacked with fairly good repeatability. Simulated mines, inert mines, and clutter such as rocks and sticks can be buried within a 2×2 m scannable region in the center of the tank. The typical scan region of 80×120 cm is outlined in Fig. 3. The scan region is sufficiently far from the tank walls that wall reflections can be time-gated out of the data. The sensor can be scanned over this region with a three degree-of-freedom positioner fixed above the tank.

Experiments in the tank indicate the presence of two measurable propagating wave types: a slow, large amplitude surface wave that propagates at 80 to 100 m/s (Rayleigh wave) and a smaller, faster bulk wave that propagates at 190 to 250 m/s (compressional wave). Data taken along a one-dimensional (1-D) scan away from the source and moving right on top of the mine is shown in Fig. 4. The seismic source is located at 80 cm from the first receiver position. In addition to the strong forward Rayleigh wave, we can also see the compressional wave, especially at the receiver positions with offset less than 60. The two scans in Fig. 4 are for a VS-1.6 (AT) mine buried at a depth of 5 cm and a TS-50 (AP) mine buried at a depth of 1 cm. In the case of the TS-50, which is an anti-personnel (AP) mine, there is strong resonance on top of the mine. For the VS-1.6, which is an anti-tank (AT) mine, there is a stronger reflection from the mine and less resonance because the VS-1.6 is buried deeper.

1.1.2 Existing Imaging Algorithm

Typically, the data are collected on a two-dimensional grid covering the entire scan region shown in Fig. 3. One example of such raw data for a TS-50 buried at a depth of 1 cm is shown in Fig. 5. This figure shows the interaction of waves with the TS-50 at four time instants. The first processing step is to apply an imaging algorithm to determine the exact locations of the mines. The imaging algorithm presented in [11] exploits two basic properties. The first property is that the incident forward wave is reflected when it arrives at a buried object and the second property is resonance. The reflection property is most useful for the case

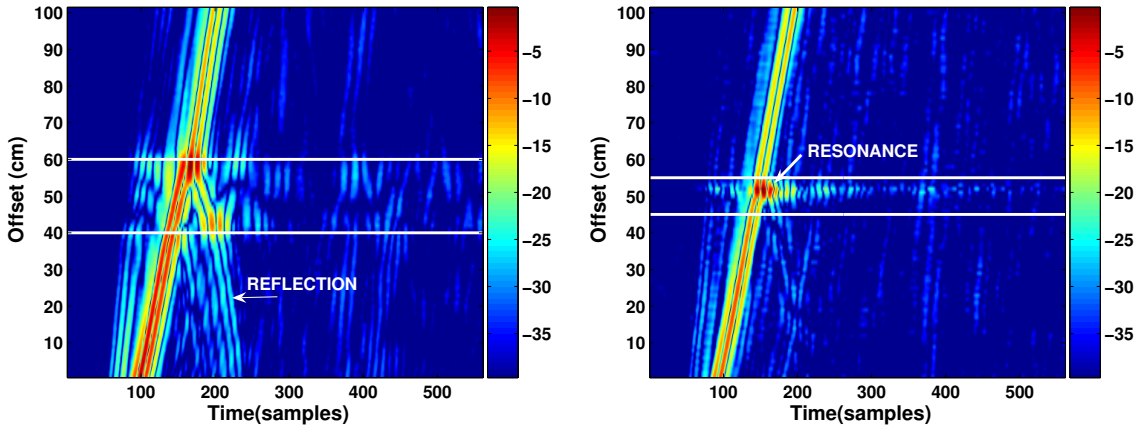

Figure 4: Typical scans made over the buried mines, showing displacement. Positions of the edges of the mines are shown by horizonal white lines (dB scale) [62, 63]. (a) VS-1.6 at 5 cm depth (20 cm diameter). (b) TS-50 at 1 cm depth (10 cm diameter).

of large anti-tank mines. The reflection from small mines such as anti-personnel mines is less; however, in these mines the structural resonance is very strong. For small mines, the imaging algorithm exploits the structural resonance to distinguish the mines from common types of clutter like rocks.

One way to define a reflector is to select the point where the first arrival of the incident wave is time coincident with the reflected wave. The resonance also starts at the first arrival of the incident wave to the mine. The basic idea behind the algorithm proposed in [11], is to compare the incident and reflected waves at each point in the region being imaged. Thus we calculate the time it takes for the wave to travel from the source to a point on the surface and then calculate the energy in the reflection and resonance around that point. The algorithm consists of the following steps [11]:

1. Separate the forward and reflected waves. This separation can be done most easily in the frequency-wavenumber domain.

2. Calculate the forward wave's group velocity, and calculate the time, $t(x, y)$, that the forward wave will take to reach a point (x, y) on the surface.

3. At each spatial position (x, y), form a window of length N across time, whose center is given by $t(x, y)$. Then calculate the energy in this windowed portion using only

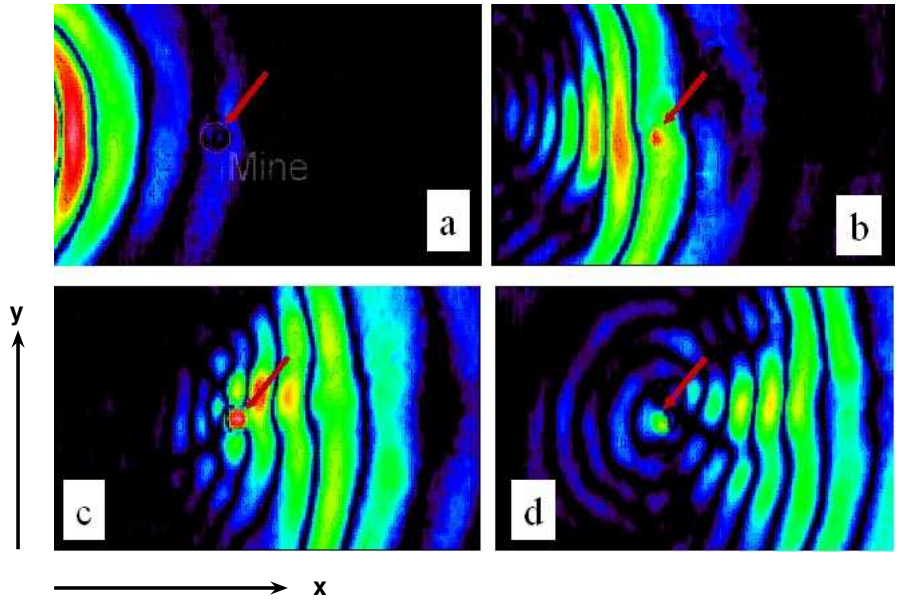

Figure 5: Surface displacements showing interaction of waves with TS-50 buried at a depth of 1 cm, at four instants [63]. Location of mine is indicated by an arrow (40 dB scale), (a) before wavefronts reach the mine (b) the main pulse interacts with mine (c) after the main pulse has passed the mine, resonance can be seen at mine location (d) reflections start coming from mine.

reflected waves. This is also weighted by energy which is reflected back from point (x, y).

The result of applying this algorithm for two different mines is shown in Fig. 6. The two mines are a VS-1.6 mine buried at a depth of 5 cm and a TS-50 mine buried at 1 cm. The data was collected over a 2-D grid of 100×100 cm, and a typical scan takes nearly 9 hours to complete. In both cases, the mine location can be seen clearly.

In the second example, multiple mines are buried at various depths and surrounded by rocks. There is a VS-1.6 AT mine surrounded by TS-50, butterfly, VS-50, and M-14 AP mines. The burial depths for the mines were 4.5 cm for the VS-1.6, 2 cm for the TS-50, the VS-50, and the butterfly, and 0.5 cm for the M-14. The burial depths for the rocks were 3.5 cm, 1.5 cm, 2 cm, and 1 cm (clockwise, starting with the upper left rock). The setup and the final image are shown in Fig. 7. The algorithm is able to locate the mines, with hardly any indication of rocks. This example demonstrates how effective this technique is

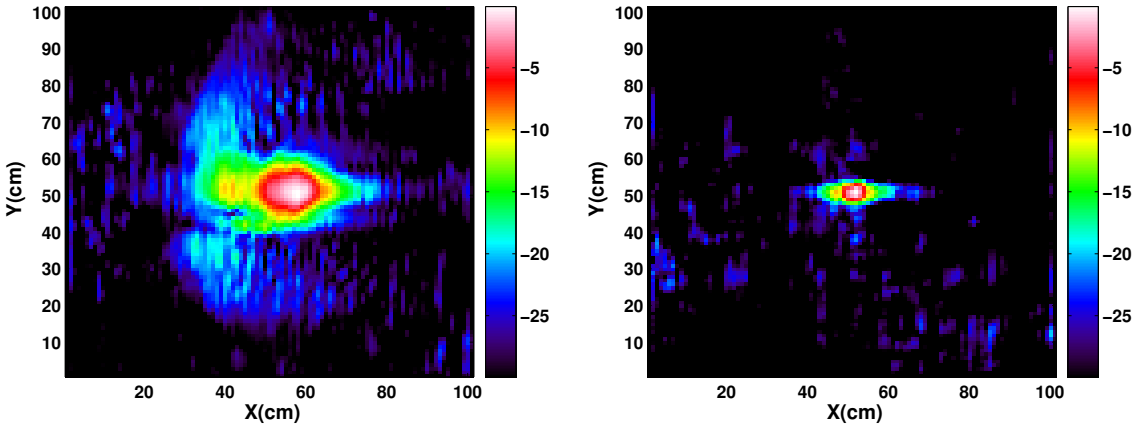

(a) (b)

Figure 6: Result of applying the imaging algorithm to the raw collected data (30 dB scale). (a) VS-1.6 at 5 cm depth (20 cm diameter). (b) TS-50 at 1 cm depth (10 cm diameter).

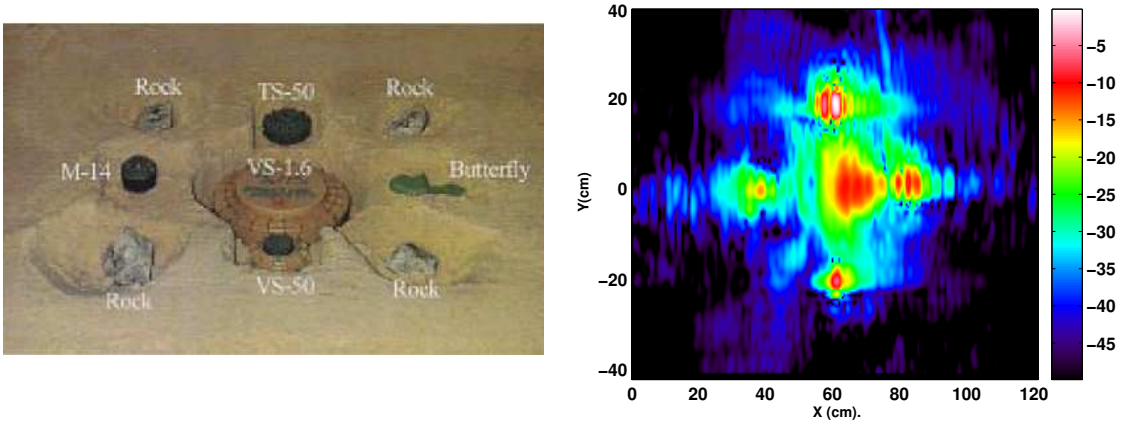

(a) (b)

Figure 7: Imaging in clutter. There are five mines (4 AP and 1 AT mine) buried at various depths, and surrounded by four rocks. (a) Actual setup. (b) Final image (50 dB scale).

in discriminating mines from clutter [63].

1.1.3 Main Drawback of the Existing Processing

The imaging algorithm presented in the previous section exhibits satisfactory mine detection performance. However, the data collection and processing are time consuming, and many expensive measurements must be taken over a 2-D grid with large apertures to have sufficient image resolution over the space of interest. In addition, the best way to make final confirmation is to use the structural resonance properties of mines, especially for smaller AP mines. For this it is necessary to move on top or very close to the mines. However, this position is not known a priori in actual situations. Therefore, to search even a small area of size 1 m^2, a large number of measurements is required. If we can reduce the number of measurements, then we can reach our goal of using a mobile platform for sensing the environment autonomously.

1.2 Proposed Solution

To reduce the number of measurements and the processing time, an adaptive sensing mechanism is proposed, in which the imaging and detection will be done by optimally maneuvering the receiving array [1–3]. To effectively image any single target, only a small subset of the measurements is actually required, but we do not know this subset ahead of time. Therefore, if we want to reduce the time or the resources needed to localize a target, one approach is to use a maneuvering receiver array to take measurements only when needed. This will be possible if we can develop an adaptive algorithm to find the best receiver positions for taking data. The strategy will be to make each new measurement so that we maximize the information gained about the target. In our case, we will use a maneuvering 3×3 array to detect and locate mines. In the method proposed, any one image, created during successive measurements, has low resolution (large uncertainty about the target position). However, as the array maneuvers, an imaging operation that uses the cumulative measurements would improve the resolution around the mine location.

The array movement will be based on the theory of optimal experiments [23]. Starting with a 2-D sensor array with known relative positions, an initial estimate of the target

location is made. Then, the variance of the location estimate is calculated by using the Fisher information matrix (FIM). Based on the expected value of the FIM, the next optimal array position is determined by using the theory of optimal experiments [23,45]. The search for the optimal array position maximizes the determinant of the Fisher information matrix. The two steps involved in the maneuver strategy for a mobile array of sensors are shown in Figs. 8(a) and 8(b).

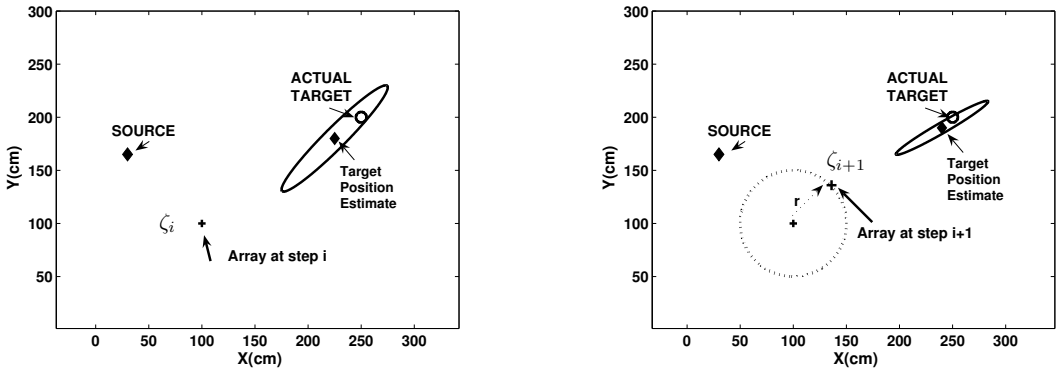

(a) (b)

Figure 8: Optimal maneuvering algorithm: (a) Source generates a probing pulse. The waves are reflected from the target and are collected at a receiving array. At step i, the target position z_i is estimated when the array center is at ζ_i. (b) Estimate the next array position ζ_{i+1} by using the estimated target position z_i and the Fisher information matrix measure.

The proposed mechanism for optimally maneuvering array consists of three major steps:

1. The maneuvering array has to work with only the reflected wave to locate the target. However, because the seismic source is also in the vicinity, the array will also record a very strong forward probing pulse. If the target is far away, we can time-gate the forward pulse, but in the vicinity of the target, it is very difficult to separate the two waves. Therefore, a robust algorithm is needed to first identify different wave types and then to separate them.

2. After the waves have been separated, the next step is to image the targets to locate their positions. The sensor array and source form an active array system. The data model that can be applied to this case must be derived. The big question is whether can we apply the model used in classical passive array design or whether another

model is needed. After forming the data model, the next step is to derive an imaging algorithm. Also, we have to decide whether processing has to be done in the time domain or the frequency domain. However, the nature of the seismic wave suggests that frequency domain processing is more suitable for this problem for two reasons. First, soil is an example of a highly dispersive medium, where propagation velocity varies with frequency. Second, targets at various depths can be imaged by varying the frequency content of the probing pulse. Since the propagation velocity varies with frequency, we have to formulate a propagation model and steering vectors that can be applied to this case.

3. The main goal is to place the array on a mobile platform, which can maneuver as it senses the environment. Therefore, the size of the array has to be small, which means a small aperture. This small aperture will result in low resolution or higher uncertainty about the position estimate of the target. One way to increase resolution is to increase the effective aperture by moving the array and forming a synthetic aperture. Finally, an algorithm has to be derived that can be used to determine the next optimal position for the array.

1.3 Contributions and Organization of the Thesis

The mechanics of optimal maneuvering require the interactions of three main steps, as described in the previous section. The first step deals with seismic wave identification and separation, the second deals with data models and imaging, and the third deals with optimal maneuvering to increase effective aperture. The interaction of all these three steps will result in a location estimate of the target with reduced uncertainty. The algorithms for all these steps needs to be formulated. In the end, we have to move on top of the target to extract resonance and make a final decision; therefore, another algorithm is required for this. The main contributions of this thesis are the formulation of the new algorithms for all these different steps, which are interdependent for making the final confirmation.

The basic background and some of the existing algorithms for the three steps of the proposed solution are presented in Chapter 2. The chapter includes a review of some of

the existing spatial spectrum analysis techniques. Also the theory behind optimal sensor placement is presented.

The new spatial spectrum analysis technique for surface waves is presented in Chapter 3. The parametric model is derived, and the Prony-based algorithm is presented for estimating the parameters of this model. The algorithm is also extended to a multi-channel case, which is useful in predicting the polarization behavior of the surface waves. The various modes of the surface waves could be identified and their parameters could be extracted. These various modes could also be reconstructed again in the time domain. All the algorithms are tested by using both numerical and field data. The spectrum analysis technique can also be used to separate the forward and reflected waves in the case of buried targets. This technique can also be used to estimate three different velocities for surface waves, namely, phase, group, and effective velocity. The dispersion curves obtained from this analysis could also be used in the inversion for determining the shear wave profile of the subsurface.

Two new imaging algorithms are proposed in Chapter 4 for the case of fixed linear arrays. The data model is derived, which will be used again in the imaging algorithm for optimal maneuvering. Both algorithms use a multi-static active array system, and all of the processing is done in the frequency domain. One algorithm is based on the near field DOA and range estimates, using a 2-D MUSIC algorithm, and second on the CLEAN/RELAX algorithm. The performance of these algorithms is demonstrated by using both numerical and experimental data. The performance of both algorithms is satisfactory in locating the targets, except that both require a large number of measurements.

To reduce the number of measurements and processing time, a new method for optimal maneuvering is proposed in Chapter 5. The idea is to place the array on a mobile platform that is capable of sensing the environment on its own. However, to perform this autonomous maneuverability, new algorithms are required. The data model, imaging algorithm for estimating target position, and the performance bound for this position estimate are derived. Next, based on the position estimate and performance bound, the algorithm for optimal maneuvering is presented. Two constraints for the movement are also defined from the physics of the problem. All the algorithms are tested by using experimental data collected

in a laboratory setting. A single TS-50 (AP) mine is used as a target in this example.

The real-time implementation for the optimal maneuvering is given in Chapter 6. A prototype array is built in a laboratory setting, consisting of three rows of 10 sensors (accelerometers) each. The movement of the array and its interface with Matlab is controlled by LabView. A multi-mode imaging algorithm is proposed, consisting of three modes. All the algorithms are tested using this array in realtime for cases with one and two targets. Also, the performance of the algorithm in the presence of common types of clutter like rocks is tested. Finally, the result of processing in the case of drunken waves is given. These waves are generated whenever there is a drastic change in the propagation properties of intervening medium. With a dramatic velocity change, waves take a curved route instead of propagating on a straight path.

In Chapter 7, we present an imaging and detector framework for confirmation. In this step, the array is acting in a detection mode. The exact location of the target has been identified by the optimal search mode. The array will move to this area and collect data along a straight line to the target. An imaging algorithm is presented that uses the extracted forward and reflected waves. A detector framework is also proposed, based on the Generalized Likelihood Ratio Test (GLRT) for making the final confirmation.

Finally, Chapter 8 concludes this thesis with the main contributions and future work.

CHAPTER II

THREE STEPS OF PROPOSED SOLUTION: BASIC BACKGROUND

As mentioned in the previous chapter, the proposed mechanism for optimal maneuvering of an array requires three steps. The first step deals with seismic surface wave identification, separation and velocity estimation by means of spatial spectrum analysis. The second step deals with data models and imaging algorithms, and the third deals with the optimal maneuvering of the array. In this chapter, we will explore some of the spatial spectrum analysis techniques that have been proposed along with their strengths and drawbacks. We will also explore some proposed models and imaging algorithms for near-surface buried targets. Finally, we will look at the theory of some of the algorithms that deal with optimal sensor placement for diverse applications ranging from direction-of-arrival (DOA) estimation to chemical vapor source localization to electromagnetic induction sensing.

2.1 Spatial Spectrum Analysis Techniques

In geophysics, Spectrum Analysis of Surface Waves (SASW) is a type of algorithm for determining the Rayleigh surface wave dispersion and attenuation curves, which are plots of phase velocity and material attenuation as a function of frequency, respectively [26, 36, 38]. After the dispersion and attenuation curves are estimated, an inversion algorithm determines the layered Earth shear and damping profile. Soil is an example of a highly dispersive medium, where propagation velocity varies with frequency. The result of dispersion is that the phase and group velocities for seismic waves are also different. Another important property of seismic wave propagation in a layered medium is the existence of several modes of propagation, the most dominant being the one related to the Rayleigh surface wave, which carries most of the seismic energy. In most cases the Rayleigh wave mode needs to be identified because it is important in our algorithm's implementation. The first reason is that most of

the imaging algorithms proposed and used in this thesis require an accurate propagation model, as given by the 2-D Green's function [2, 6, 7]:

$$G(r, r', \omega) = \frac{i}{4} H_0^{(1)}(\frac{\omega}{v(\omega)}|r - r'|) \tag{1}$$

where $H_0^{(1)}$ is the zero-order Hankel function of the first kind, and v is the Rayleigh wave velocity at the frequency ω. In this case, it is necessary first to identify the Rayleigh wave mode and then to estimate its velocity as a function of the frequency. The second factor is the use of the reflected Rayleigh wave in imaging. However, because the source is close to the receivers, the forward probing pulse is also recorded by the receivers. Therefore, some spatial filtering has to be done to separate the forward and reflected waves. This processing can be done in the frequency-wavenumber domain by first identifying the forward and reflected waves, and then separating them. An efficient algorithm based on spatial spectrum analysis techniques has been derived for this and will be presented in Chapter 3

The most common and traditional method for estimating the dispersion curve is the so-called two-station (point) method, which uses the time delay between two receivers located at some distance from the source [26, 36, 38]. Phase velocity as a function of frequency can be obtained from the phase of the average cross-power spectrum. Suppose the two signals at two receivers in the time domain are $y_1(t)$ and $y_2(t)$ respectively, with Fourier transform $Y_1(\omega)$ and $Y_2(\omega)$. Then, the cross-power spectrum is defined as

$$G_{12}(\omega) = Y_1(\omega) Y_2^*(\omega) \tag{2}$$

and the phase of the cross-power spectrum is

$$\Theta_{12}(\omega) = \angle G_{12}(\omega) \tag{3}$$

The time delay between receivers is

$$t(\omega) = \frac{\Theta_{12}(\omega)}{\omega} \tag{4}$$

Then, the phase velocity of the surface waves is

$$V_R(\omega) = \frac{D}{t(\omega)} \tag{5}$$

where D is the distance between the two receivers. This method is able to predict only the strongest mode. It is also affected by phase unwrapping in the cross-power spectrum. Some other methods are least-squares fitting of wavenumbers, and the multi-channel wave field transformation method, both of which suffer from the same problem as all two-station methods, i.e., they can predict only one mode and they rely solely on phase data [73].

If data is collected by an array of sensors, then frequency-wavenumber analysis can be used to identify the modes and estimate dispersion curves, using space-time data collected by an array of sensors. Any space-time signal can be represented as the superposition of monochromatic (single ω-$\mathbf{k}$) plane waves [20, 34]. If $s(\mathbf{x}, t)$ represents a signal that is a function of a spatial position $\mathbf{x}$ and time t, we can use a continuous 4-D Fourier transform to obtain the 4-D frequency-wavenumber spectrum $S(\mathbf{k}, \omega)$

$$S(\mathbf{k}, \omega) = \int_{-\infty}^{\infty} .. \int_{-\infty}^{\infty} s(\mathbf{x}, t) \exp[-j(\omega t - \mathbf{k}^T \mathbf{x})] d\mathbf{x} dt \tag{6}$$

The variable ω represents temporal frequency, and the variable $\mathbf{k}$ represents spatial frequency, defined as the number of waves per unit distance in each of three orthogonal spatial directions. Thus, $\mathbf{k} = (k_x, k_y, k_z)$ is a wavenumber vector, and $\mathbf{x} = (x, y, z)$ is the position vector. Signals of the form

$$e(\mathbf{x}, t) = \exp[j(\omega_0 t - \mathbf{k}_0^T \mathbf{x})], \tag{7}$$

represent propagating plane waves. The direction of propagation is $\frac{\mathbf{k}_0}{|\mathbf{k}_0|}$.By taking the Fourier transform of the signal $e(\mathbf{x}, t)$ using (6), we get

$$E(\mathbf{k}, w) = \delta(\mathbf{k} - \mathbf{k_0}) \delta(\omega - \omega_0) \tag{8}$$

which is a 4-D impulse (a Dirac delta function) in $(\mathbf{k}, \omega)$ space at a point, $\mathbf{k} = \mathbf{k_0}$ and $\omega = \omega_0$. Each point in $(\mathbf{k}, \omega)$ space thus corresponds to a plane wave in $(\mathbf{x}, t)$ space with a particular orientation and frequency.

Power spectral density (PSD) estimation in the spatial domain requires the design of a spectral filter with optimum capability of isolating a single ω - $\mathbf{k}$ pair. One way to isolate the waves is by using the 2D Fourier transform of the space-time data as explained above. However, this gives a low resolution ω - $\mathbf{k}$ spectrum. Several high-resolution algorithms

have also been proposed, based on modern spectrum estimation techniques like MUSIC, MVDL, etc [73]. Since seismic surface wave propagation tends to be dispersive and contain multiple modes, frequency domain spectrum estimation must be used. These high resolution techniques are based on forming a spatio-spectral correlation matrix using array data. Assume that we have a single channel space-time data, so that wavenumber k is a scalar. Suppose each sensor data vector $s(n)$ is of length N, which is divided into B blocks of length $L = N/B$. The cross power spectrum for each block is calculated and averaged for all sensor spatial lags as

$$R_{i,j}(\omega) = \frac{1}{B}\sum_{n=1}^{B} S_{i,n}(\omega)S^{*}_{j,n}(\omega) \tag{9}$$

where $R_{i,j}(\omega)$ is the cross power spectrum between the i^{th} and j^{th} sensors, $S_{i,n}(\omega)$ is the Fourier transform of the i^{th} sensor's data in the n^{th} block and $*$ indicates complex conjugation. Using (9), the spatio-spectral matrix at each frequency ω can be formed as [67, 73]

$$R(\omega) = \begin{bmatrix} R_{1,1}(\omega) & R_{1,2}(\omega) & \cdots & R_{1,p}(\omega) \\ R_{2,1}(\omega) & R_{2,2}(\omega) & \cdots & R_{2,p}(\omega) \\ \vdots & \vdots & \ddots & \vdots \\ R_{p,1}(\omega) & R_{p,2}(\omega) & \cdots & R_{p,p}(\omega) \end{bmatrix} \tag{10}$$

where p is the number of sensors. The matrix is Hermitian symmetric, is a function of frequency, and contains information about the spatial properties of the wavefield.

The conventional frequency domain beamformer output power is given by

$$P_{FDBF}(k,\omega) = \mathbf{a}^{H}(k)R(\omega)\mathbf{a}(k) \tag{11}$$

where P is the power and $\mathbf{a}(k)$ is the steering vector given by

$$\mathbf{a}(k) = [e^{-jkx_1} \quad e^{-jkx_2} \quad ... \quad e^{-jkx_p}]^{T} \tag{12}$$

The steering vector tries to align the array with plane waves propagating from a given direction with a given phase velocity, and if it is successful, a peak occurs in the ω - k spectrum estimate. Next is Capon's Minimum Variance Distortionless Look (MVDL) beamformer, whose output power is given by [16, 67, 73]:

$$P_{MVDL}(k,\omega) = \frac{1}{\mathbf{a}^{H}(k)R^{-1}(\omega)\mathbf{a}(k)} \tag{13}$$

The MVDL beamformer exhibits greater resolution in many cases due to the adaptive nature of the wavenumber filter. Next, we will look at some of the subspace methods of spatial spectrum estimation. These are based on decomposition of the correlation matrix into signal and noise subspaces, which are orthogonal to each other. The spatio-spectral correlation matrix may be expanded using its eigenvalue decomposition as

$$R(\omega) = \sum_{i=1}^{P} \lambda_i(\omega)\mathbf{v}_i(\omega)\mathbf{v}_i^H(\omega) \tag{14}$$

where $\mathbf{v}_i$ is the i^{th} eigenvector, corresponding to the i^{th} eigenvalue λ_i. Since the eigenvectors are orthogonal, this decomposition can be split into two orthogonal subspaces

$$R(\omega) = \sum_{i=1}^{N_s} \lambda_i(\omega)\mathbf{v}_i(\omega)\mathbf{v}_i^H(\omega) + \sum_{i=N_s+1}^{P} \lambda_i(\omega)\mathbf{v}_i(\omega)\mathbf{v}_i^H(\omega) \tag{15}$$

where N_s is the number of signals present and P is the number of sensors in the array. The first summation on the right includes the N_s largest eigenvalues and their corresponding eigenvectors and corresponds to the signal subspace, and the second sum on the right includes the $(P - N_s)$ smallest eigenvalues and their corresponding eigenvectors and corresponds to the noise subspace. The noise eigenvectors span the noise subspace, and the signal eigenvectors span the signal subspace. The first subspace method is based on the Pisarenko harmonic decomposition, which uses the eigenvector corresponding to the smallest eigenvalue [67, 73]. The power spectrum of this estimator is given by

$$P_{PHD}(k,\omega) = \frac{1}{|\mathbf{a}^H(k)\mathbf{v}_{min}(\omega)|^2} \tag{16}$$

This inner product will be zero at the locations of the frequency-wavenumber pairs corresponding to propagating signals, because of the fact that the signal and noise subspaces are orthogonal to each other. The most popular of the subspace methods is MUSIC, which stands for Multiple Signal Classification. In this method a truncated version of the spatio-spectral matrix is formed by using only the eigenvectors in the noise subspace [59, 67, 73]. The truncated matrix using the noise subspace is given by

$$R_{MUSIC}^{-1}(\omega) = \sum_{i=N_s+1}^{P} \mathbf{v}_i(\omega)\mathbf{v}_i^H(\omega) \tag{17}$$

The output power of the estimator is given by

$$P_{MUSIC}(k,\omega) = \frac{1}{\mathbf{a}^H(k) R^{-1}_{MUSIC}(\omega)\mathbf{a}(k)} \tag{18}$$

All the high resolution methods are based upon plane wave assumption, even though seismic waves obey a cylindrical wave model. Despite the mismatch it has been shown that the performance of plane wave estimators is satisfactory, except at very low frequencies [73]. The derivation of a cylindrical beamformer simply uses the Hankel transform rather than the Fourier transform. The steering vector is defined in this case as

$$\mathbf{h}(k) = e^{-j[\arg(H_0(kx_1)) \quad \arg(H_0(kx_2)) \quad ... \quad \arg(H_0(kx_p))]} \tag{19}$$

where arg denotes taking the phase, and H_0 is the zero order Hankel function of the first kind. A far-field (large kx) approximation for Hankel function is used as given by [12]:

$$H_0(kx) \approx \sqrt{\frac{2}{\pi kx}} e^{j(kx-\frac{\pi}{4})} \tag{20}$$

All these methods are able to give an estimate of dispersion curves, and some are able to estimate the multiple modes of surface waves, but no method has the ability to extract these different modes or to predict the polarization behavior of the surface waves. The separation of the forward and reflected waves is also an important preprocessing step for the imaging algorithms. These waves can be separated in the frequency domain by using a frequency-wavenumber filter. With a 2-D Fourier transform of space-time data, waves travelling in opposite directions can be mapped to different quadrants from which they can be separated [11, 15, 63]. However, the Fourier method cannot predict and identify the individual well-defined modes. On the other hand a parametric method can model these multi-mode surface waves, identify the waves with common modes and separate them, and then reconstruct them. One suitable method is an extension of the parametric method developed for sonic logging applications, which is a based on Prony's method [28, 39, 46, 47].

2.2 Imaging of Near-Surface Targets Using Seismic Waves

Seismic techniques in geophysics are typically used for imaging deeper targets. Also, these targets are much bigger than typical near-surface targets, like landmines. Rayleigh waves

are problematic for classical seismic measurements because their displacements decay exponentially away from the Earth's surface. These waves do not interrogate soil deeper than their wavelength, and they have large surface displacement. However, these features make the Rayleigh wave an excellent interrogation signal for the detection of near-surface landmines. The earliest example of imaging landmines using seismic waves is in [64]. The array setup is a multi-static configuration with multiple sources and receivers. Each source is activated one at a time and the reflected signal is recorded at each receiver to build up a multi-static data matrix. The imaging algorithm is based on the time domain back-propagation algorithm. Assuming n_s sources and n_r receivers, the distance from the j^{th} source to the k^{th} point in space (an image point) is Ds_{jk} and the distance from the image point to the i^{th} receiver is Dr_{ki}. Let $S_{ij}(t)$ be the data collected at receiver i when the signal is applied at source j. The travel time from the source to an image point and back to the receiver is

$$t_{kij} = \frac{Ds_{jk} + Ds_{jk}}{V_R} \tag{21}$$

where V_R is the Rayleigh wave velocity (assumed constant). The amplitude of the array output to be assigned to the k^{th} image point is

$$A_k = \sum_{j=1}^{n_s} \sum_{i=1}^{n_r} S_{ij}(t_{kij}) \tag{22}$$

The Rayleigh wave velocity (group velocity) is estimated by a radial scan, which is done at the middle of the search region. In this scan an array of equally spaced receivers are placed at some distance from the seismic source, and used to record the wave. From this scan first Rayleigh wave is identified by using polarization, and then its velocity is determined from the slope of Rayleigh wave arrivals in each receivers. However, there is a problem in estimating accurate velocity because of dispersion, and variability in the propagation properties of the medium. There was no need to separate the forward and reflected waves, as back-propagation is used for imaging. Because of the dispersion and other effects, the results were not accurate, especially for AP mines. Later on, instead of doing seismic sonar type of imaging, it was advocated that for detection, the structural resonance of the mines should be exploited, and for this it was necessary to be on top

of the target [11, 58, 63]. The system and imaging algorithm for this kind of setup was given in previous sections. This imaging algorithm is effective and the only drawback is that it requires a large number of measurements, which are costly, time consuming and slow. Imaging of scattered seismic waves is also done in [15], using an impedance function matching and minimizing an objective function. Again, the waves are separated in the frequency-wavenumber domain and the scattered wave is reconstructed in the time domain.

2.3 Optimal Sensor Placement

Optimal sensor placement comes into play in the context of a maneuvering sensor scenario. Most of these optimally maneuvering sensor examples use some form of the Fisher information matrix (from which the of Cramér-Rao bound is obtained). One theory that can be applied to optimal sensor placement is that of optimal experiments [23, 57]. This theory predicts the results of experiments based on information-theoretic concepts. In detection and estimation theory, uncertainties of states and observations are represented by probability distributions and the concept of information is introduced as a measure of how much information is contained in such distributions. There are two formal definitions of information, entropic information and Fisher information. Fisher information is used as the design criterion in the theory of optimal experiments. Various measures of Fisher information are used to formulate different design criteria like D-criterion, A-criterion, and E-criterion, etc [23, 57].

The Fisher information can be thought of as the amount of information that an observable random variable Y carries about an unobservable parameter θ upon which the probability distribution of Y depends. The Fisher information matrix is obtained from the log-likelihood of the random variable Y, given θ [40, 53, 69]:

$$F(\theta) = E_\theta \left[\left(\frac{\partial \ln p(Y;\theta)}{\partial \theta} \right)^2 \right] = -E_\theta \left[\left(\frac{\partial^2 \ln p(Y;\theta)}{\partial^2 \theta} \right) \right] \tag{23}$$

where $E(.)$ is the stochastic expected value with respect to data distribution. If y is a specific collected data set, then the observable or empirical Fisher information is obtained. For the case in which $\hat{\theta}$ is the unbiased estimator of θ, the so-called Cramér-Rao lower

bound (CRLB) is given by

$$var_\theta[\hat{\theta}(Y)] \geq \frac{1}{F(\theta)} \tag{24}$$

Thus, the higher the information content, the better the lower bound on estimation accuracy. If θ is a multi-component vector, the Fisher information is a matrix given by

$$F_{rc} = E_\theta \left[\frac{\partial \ln p(Y;\theta)}{\partial \theta_r} \frac{\partial \ln p(Y;\theta)}{\partial \theta_c} \right] = -E_\theta \left[\frac{\partial^2 \ln p(Y;\theta)}{\partial \theta_r \partial \theta_c} \right] \tag{25}$$

The matrix CR bound for unbiased estimators is given by

$$cov_\theta[\hat{\theta}(Y)] \geq F^{-1}(\theta) \tag{26}$$

The theory of optimal experiments uses different measures of the Fisher information matrix to come up with the design criteria. The most common is the so-called D-optimal design, which is equivalent to maximizing the determinant of the Fisher information matrix. Maximizing the determinant of the information matrix is the same as minimizing the determinant of the CRLB matrix. Let $\lambda_1, ..., \lambda_n$ be the eigenvalues of the Fisher information matrix, then the determinant is

$$|F| = \prod_{i=1}^{n} \lambda_i \tag{27}$$

As an example, for an estimator of two parameters, the so called confidence region is an ellipse called the ellipsoid of concentration, as shown in Fig. 9 [10, 23]. The major axis of this ellipse is given by $L_1 = \frac{2}{\sqrt{\lambda_1}}$, and minor axis by $L_2 = \frac{2}{\sqrt{\lambda_2}}$. The ellipsoid volume V_E is proportional to the product of the axis length. Therefore, it is proportional to the square root of the product of the matrix eigenvalues. This product is also the inverse of the matrix determinant $|F|$. Thus,

$$V_E = K(L_1 \times ..... \times L_p) = \frac{K}{\sqrt{\lambda_1 \times ..... \times \lambda_p}} \tag{28}$$

$$= \frac{K}{\sqrt{|F|}} \tag{29}$$

Thus, a D-optimal design ensures that the volume of the confidence region is minimized by increasing the determinant of the Fisher information matrix. Another common method is the A-optimal design, which uses the trace and is given by

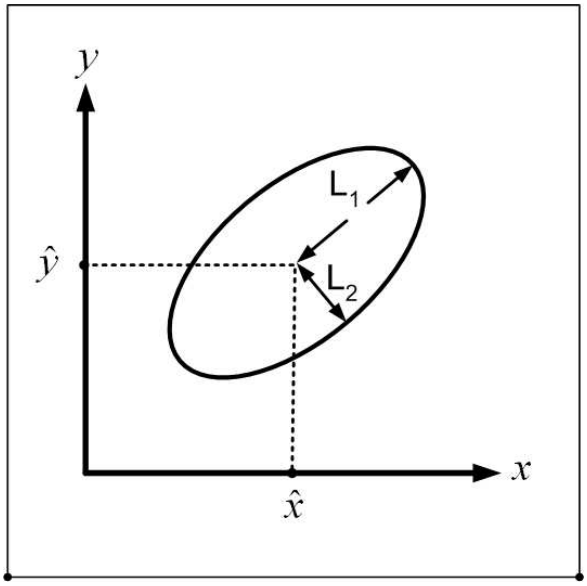

Figure 9: Ellipsoid of concentration for two parameters (x,y).

1. max trace(F)= $\sum_{i=1}^{n} \lambda_i$
2. min trace(F^{-1})=$\sum_{i=1}^{n} \frac{1}{\lambda_i}$

There is also an E-optimal design, which uses the maximum value along the diagonal of the CR matrix [57].

An example of using the method of optimal experiments for sensor placements can be found in [30, 31], which deals with the movement of sensors used in direction-of-arrival (DOA) estimation to localize the source. The optimality criterion is based on maximizing the determinant of the Fisher information matrix and minimizing the trace of the Cramér-Rao lower bound. In this case, the optimal observer (sensor) path is determined to localize a moving source. In [71], a single moving sensor is used to localize the vapor emitting source. In this case an estimate of the location of the source and its CR bound is calculated at each step. The sensor position at $n + 1$ is calculated so as to minimize the CR bound on the location errors, given the measurement up to and including $n + 1$. In [10] again, a D-optimal design is used for optimal sensor placement to solve an inverse problem. The

most recent example of D-optimal experiment design involves moving an electromagnetic induction (EMI) sensor to locate the buried target [45]. Here again, the Fisher information matrix is calculated for buried target parameters as a function of sensor position and probing frequency. The goal is to choose the next optimal sensor position that will maximize the determinant of the Fisher information matrix. The idea presented in this paper will be used for moving a seismic sensor to locate buried targets.

CHAPTER III

SPECTRUM ANALYSIS OF SURFACE WAVE AND ITS APPLICATIONS

3.1 Introduction

In geophysics, spectrum analysis of surface waves (SASW) refers to a non-invasive method for soil characterization. However, we use the term spectrum analysis in a wider sense to mean a method for determining and identifying various modes of seismic surface waves and their properties such as velocity, polarization, etc. Waves that propagate in a medium can be roughly divided into two main categories: body waves and surface waves. Surface waves are generated at a boundary and can be essentially of two types: Love waves and Rayleigh waves. Rayleigh waves are always generated when a free surface exists in a continuous body. In a vertically heterogeneous medium the phase velocity of the Rayleigh wave is a function of frequency and this dependence is strictly related to the mechanical parameters of the medium [26, 38, 51, 73]. Hence, if we can determine the dispersion curve (i.e., phase velocity vs. frequency), it is possible in principle to calculate the mechanical parameters of the medium. This technique of determining the dispersion curves is the basis of the SASW methods. Traditional methods are based on data collected at two receivers from which the phase of the average cross-power spectrum is used to calculate the phase velocity, as given in Section 2.1 [26,73]. One crucial step in this process is unwrapping the cross-power spectrum phase, because additive noise can produce fictitious jumps in the wrapped phase. Some high resolution techniques have also been developed based on frequency-wavenumber analysis in order to extract multi-modal dispersion curves [26, 73]. However, these techniques can't be used to separate these modes.

Our technique is based on the combination of a temporal Fourier transform followed by a pole-zero model across the spatial domain x [5, 9]. Using the amplitude and root estimates

from pole-zero modeling, it is possible not only to construct dispersion curves, but also to obtain insight into several other important parameters. One such property by which different types of surface waves can be identified is polarization. A surface wave consists of particle motion along a specific path, e.g., a Rayleigh wave involves particle motion along a retrograde elliptical path [22,26,61]. Hence, we can use polarization to identify these waves because we have extended our algorithm to the two-channel case. The array data is collected by means of tri-axial sensors, from which we use two channels that provide the horizontal and vertical particle motion (acceleration is actually measured). Polarization ellipses can be constructed by estimating the complex amplitudes of the measurements in these two channels. In addition to the complex amplitude, we can also estimate wavenumber and attenuation, which can be used to extract individual modes and reconstruct them in the space-time domain.

The next sections will describe the parametric model and spectrum analysis technique. The algorithm will be used to extract individual waves and their modes for numerical data as well as field data.

3.2 Parametric Model for Surface Wave-Vector Sensor Approach

The parametric model is based on the technique developed for borehole sonic logging applications [39,47]. For the single-channel case, the collected data $s(x,t)$ is a function of space and time, see Fig. 11. We can use a Fourier representation in the (k-ω) domain

$$s(x,t) = \frac{1}{4\pi^2} \int_{-\infty}^{\infty} \int_{-\infty}^{\infty} \hat{S}(k,\omega) e^{j(kx-\omega t)} dk\, d\omega, \tag{30}$$

where x is the spatial position, k is the spatial wavenumber, ω is the temporal frequency, and $\hat{S}(k,\omega)$ is a 2-D Fourier transform representation of the space-time signal $s(x,t)$. By taking a Fourier transform across t, we have

$$S(x,\omega) = \frac{1}{2\pi} \int_{-\infty}^{\infty} \hat{S}(k,\omega) e^{j(kx)} dk. \tag{31}$$

At each frequency ω, pole-zero modeling is done across the spatial dimension to get a model consisting of a sum of exponentials that represents propagating waves. In effect, we

approximate the integral in (31) with a sum

$$S(x,\omega) \approx \sum_{p=1}^{P} a_p(\omega) e^{jk_p(\omega)x}, \tag{32}$$

where P is the model order.

In the two-channel case the collected data $s(\mathbf{x},t)$ is a vector with two channels, i.e.,

$$\mathbf{s}(\mathbf{x},t) = \begin{bmatrix} s_x(x,t) \\ s_z(x,t) \end{bmatrix}, \tag{33}$$

where $s_x(x,t)$ is the horizontal displacement channel and $s_z(x,t)$ is the vertical displacement channel as in Fig. 11. If we do the processing as described above and estimate the poles and zeros separately for each channel, then we obtain two models like (32) consisting of P parameters

$$S_x(x,\omega) \approx \sum_{p=1}^{P} A_{xp}(\omega) e^{jk_{xp}(\omega)x} \tag{34}$$

$$S_z(x,\omega) \approx \sum_{p=1}^{P} A_{zp}(\omega) e^{jk_{zp}(\omega)x} \tag{35}$$

There is no guarantee that the wavenumber information for the two channels, $k_{xp}(\omega)$ and $k_{zp}(\omega)$, will match in the k-ω domain. If not, it will be very hard to align the vertical and horizontal complex amplitudes and calculate polarization.

3.2.1 Vector IQML

A better approach is to determine two models simultaneously so that they share the same poles [9]. The pole-zero modeling technique used in this paper is based on the Iterative Quadratic Maximum Likelihood (IQML) algorithm, which is also called the Steiglitz-McBride extension of Prony's method [14,48,66]. We have reformulated the IQML algorithm for the multi-channel case.

For a plane wave impinging on m two-channel sensors, we can take the temporal Fourier transform of the collected data (33) to obtain

$$\underline{\mathbf{S}}(\omega) = [\underline{\mathbf{S}}_1(\omega), \underline{\mathbf{S}}_2(\omega) \ldots, \underline{\mathbf{S}}_m(\omega)], \tag{36}$$

where

$$\underline{\mathbf{S}}_i(\omega) = \begin{bmatrix} S_x(x_i, \omega) \\ S_z(x_i, \omega) \end{bmatrix}. \tag{37}$$

The input data is the vector in (36) consisting of the complex amplitudes from both channels at a specific frequency ω. The IQML technique determines P estimates for the poles, which are the same for both channels, and then computes the best complex amplitudes which are different for the two channels. The resulting IQML model is an exponential model for the two channels

$$\underline{\mathbf{S}}(\omega) \approx \begin{bmatrix} \sum_{p=1}^{P} A_{xp}(\omega) e^{j\kappa_p(\omega)x} \\ \sum_{p=1}^{P} A_{zp}(\omega) e^{j\kappa_p(\omega)x} \end{bmatrix}. \tag{38}$$

The poles determine the exponent $\kappa_p(\omega)$whose real part is the wavenumber $k_p(\omega)$ and whose imaginary part is the attenuation $\alpha_p(\omega)$. Wavenumber is then converted to velocity via $v_p(\omega) = \omega/k_p(\omega)$, and then we can plot the magnitude of A_{xp}, or of A_{zp}, versus frequency and velocity as shown in Fig. 12(a). This type of plot makes it easy to obtain the dispersion curves of velocity vs. ω for the various modes that make up the signal. The complex amplitudes are used to determine the strength of different wave components, but they can also be used to obtain the parameters for polarization ellipses as discussed next.

3.2.2 Polarization Ellipses

The complex amplitudes obtained from two channels can be used to draw polarization ellipses [65]. If the x and z components of the vector complex amplitude are the two complex amplitudes A_x and A_z, then

$$\bar{\mathbf{A}} = A_x\hat{x} + A_z\hat{z} = A_x(\hat{x} + \alpha e^{j\varphi}\hat{z}),$$

Various parameters of the polarization ellipse can be obtained directly from α and φ. The tilt angle ψ (with respect to the x-axis) is given by

$$\tan(2\psi) = \frac{2\alpha}{1-\alpha^2}\cos(\varphi). \tag{39}$$

If major and minor axes are denoted by a and b, then the axial ratio is

$$\frac{b}{a} = \tan(\beta), \tag{40}$$

where β is

$$\sin(2\beta) = \frac{2\alpha}{1+\alpha^2}\sin(\varphi). \tag{41}$$

The major and minor axes of the ellipse are given by

$$a = \frac{1}{\sqrt{\alpha^2\cos^2(\psi) + \sin^2(\psi) - 2\alpha\sin(\psi)\cos(\psi)\cos(\varphi)}}. \tag{42}$$

$$b = \frac{1}{\sqrt{\alpha^2\sin^2(\psi) + \cos^2(\psi) + 2\alpha\sin(\psi)\cos(\psi)\cos(\varphi)}}. \tag{43}$$

In summary, the complex amplitudes derived via vector IQML modeling allow us to quickly calculate polarization parameters for the propagating waves.

3.2.3 Identifying and Reconstructing Modes

In Fig. 12(a) it is obvious that individual modes of $\mathbf{s}(\mathbf{x}, t)$ can be identified and sorted according to velocity $v_p(\omega)$ and frequency. Less obvious is the fact that polarization can also be used for sorting, but the expanded view of Fig. 12(b) shows that polarization is consistent versus frequency for an individual mode; in that case, the Rayleigh wave. Once we have sorted out a single mode in the velocity-frequency domain, the waveform for that mode can be reconstructed in the space-time domain by using the model

$$s_z(\mathbf{x}, t) = \sum_i A_z(\omega_i) e^{(\alpha(\omega_i)\mathbf{x} + j(\omega_i t + k(\omega_i)\mathbf{x}))}, \tag{44}$$

for the z channel; likewise, for the x channel.

3.3 Processing Data from Linear Arrays

Testing of this new algorithm has been carried out on both synthetic data and recorded field data.

3.3.1 Synthetic Data

Numerical data generated from a 3-D FDTD model can accurately model elastic wave propagation in a stratified medium [61]. The data simulate what the sensors would have measured on the surface with a known stratified medium specified in the model. The typical setup for data collection is shown in [2] Fig. 10, which shows a fixed seismic source

[2] Gregg Larson is the creator of Fig. 10

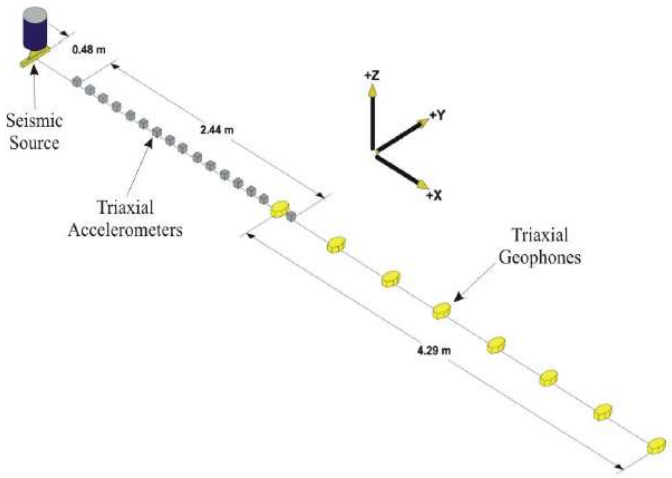

Figure 10: Setup for numerical and experimental data collection.

Table 1: Soil profile used in numerical data

Thickness (cm)	$V_s(m/sec)$	$V_p(m/sec)$	Density (kg/m^3)
2.5	60	250	1400
2.5	70	250	1400
2.5	80	250	1400
2.5	90	250	1400
∞	100	250	1400

and various types of sensors (accelerometers, geophones) arranged in the form of a linear array. Examples of synthetic data for the horizontal and vertical channels are shown in Fig. 11, where the horizontal axis is time and the vertical axis is sensor position (distance from the source). The first sensor lies 110 cm from the source and the inter-sensor distance is 0.5 cm. The total number of sensors is 60, covering an aperture of 30 cm. The soil profile used for this numerical data is given in Table 1.

Processing of this data set with the vector IQML algorithm and a model order of $P = 4$ yields the dispersion curves shown in Fig. 12(a). These multi-modal dispersion curves are typical for a layered media [26, 61]. Four different modes can be identified at the higher frequencies, with the strongest one being the Rayleigh wave. Traditional two-station

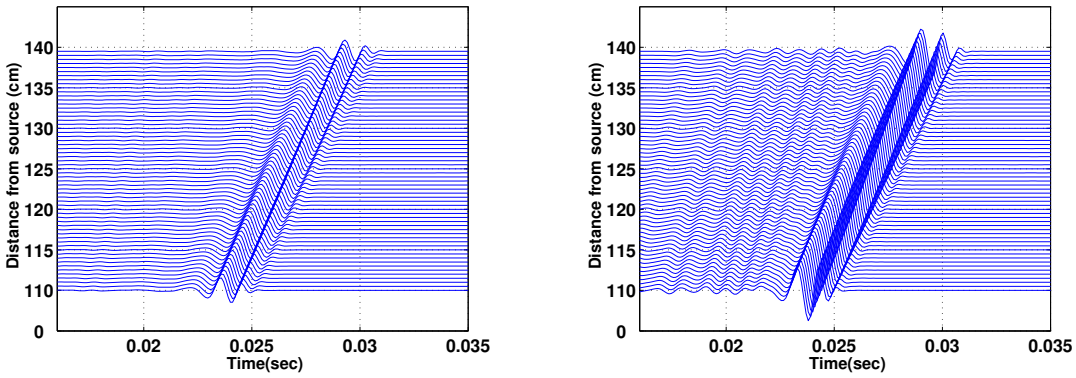

Figure 11: Space-time data for, (a) horizontal channel, (b) vertical channel.

methods would only be able to detect the dominant Rayleigh mode. Modes 1 through 3 are guided waves that are due to the layered soil properties used in the model and are essentially linearly polarized in the vertical direction [26,61]. The results obtained by IQML processing can be verified by comparing it to an analytical solution, which uses the subsurface profile as an input, and produces modes as output [36, 37]. The same profile is used to produce the space-time data in the previous example. This comparison is shown in Fig. 12(c), and the modes obtained from IQML processing follow the analytical solution very closely.

The predominant Rayleigh wave (Mode-0) exhibits an elliptical polarization, which has been calculated from the complex amplitude estimates and plotted in Fig. 12(b). At each frequency an ellipse is plotted at the corresponding phase velocity. The parameters for the ellipse, tilt angle (39), axial ratio (40), major axis (42), and minor axis (43), are obtained by using the complex amplitude estimates for the horizontal and vertical particle motion. The size of each ellipse is proportional to the complex amplitude values in the two channels. The size is also encoded in the thickness of the line displayed when plotting the ellipse, with the thickness being proportional to $\sqrt{|A_x|^2 + |A_z|^2}$. The vertical channel displacements are larger so the major axis of ellipse is tilted toward the vertical direction for the Rayleigh wave. The sign of the axial ratio is used to indicate the direction or particle motion, either retrograde or prograde. This polarization direction can be encoded with colors: a dark blue color indicating retrograde motion (as in the Rayleigh wave), and a light red color for prograde.

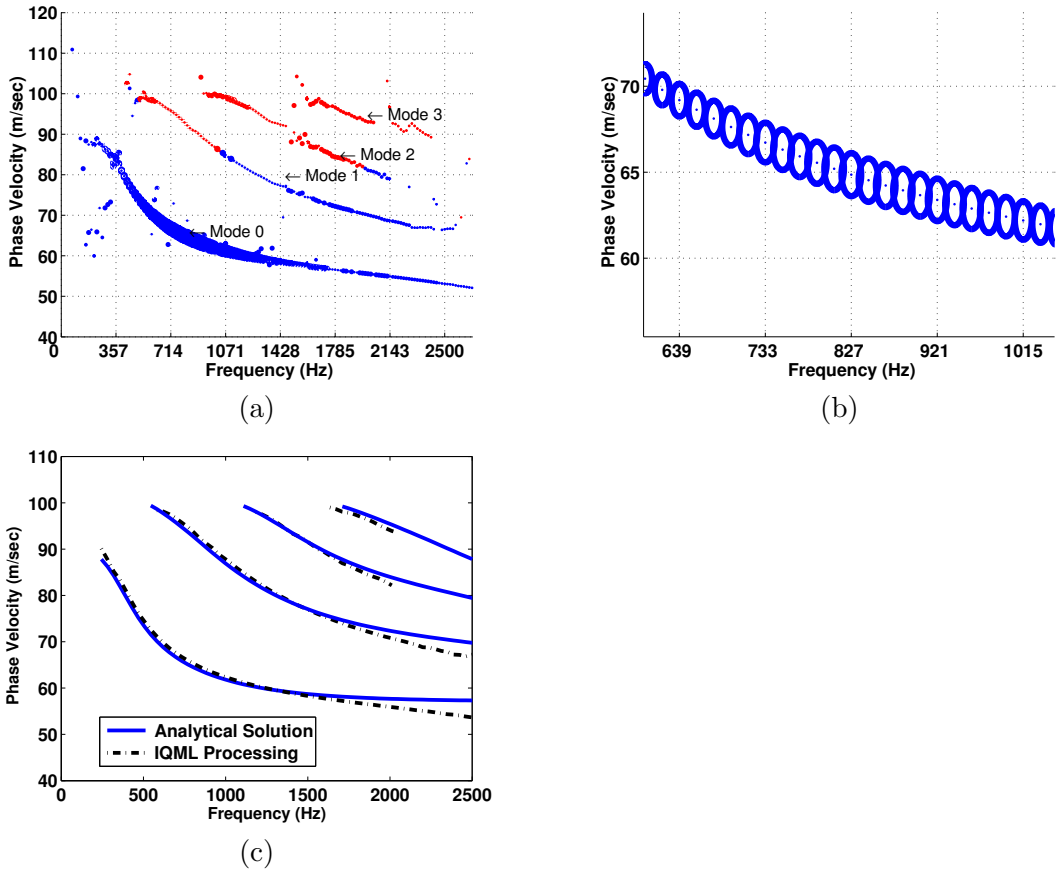

Figure 12: (a) Multi-modal dispersion curves. The model order (P) used in this processing was $P = 4$. (b) Expanded view of Mode-0 shows the polarization ellipses for the Rayleigh wave. (c) Comparison of analytical solution and IQML Processing.

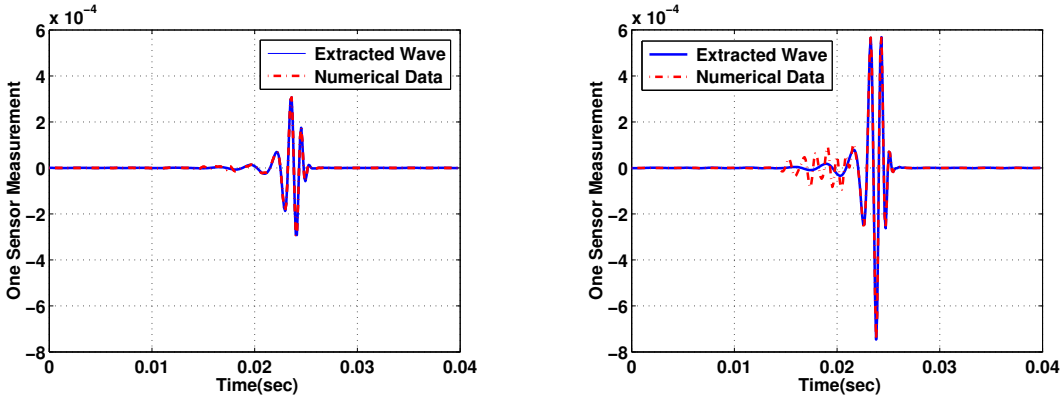

Figure 13: Extraction of Mode-0 versus the original: (a) horizontal channel, (b) vertical channel.

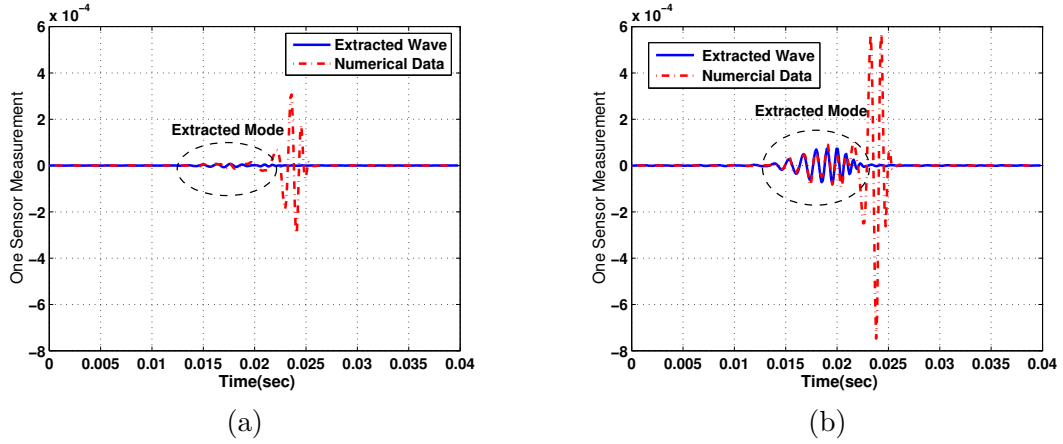

Figure 14: Extraction of Mode-1 versus the original:(a) horizontal channel, (b) vertical channel.

By extracting individual modes from these dispersion curves, along with their complex amplitudes, we can reconstruct signals in the time domain for each mode using (44). This sort of time domain re-synthesis for the fundamental mode is shown in Figs. 13(a) and (b) for the horizontal and vertical channels, respectively. The original numerical data is also shown for comparison. The reconstructed time domain plot is in close agreement with the original data especially near the main pulse. The leading edge in the reconstructed plot does not follow the original, suggesting that it is related to other higher-order modes. This fact is confirmed by the reconstruction in Fig. 14, which shows that the higher modes are related to the leading edges, especially for the vertical channel.

3.3.2 Processing for Field Data

The system used for data collection in the field is described in [11, 61–63]. A set of collected field data is shown in Figs. 15(a) and (b), for the horizontal and vertical channels, respectively. The first sensor is at a distance of 24 inches from the source with succeeding sensors one inch apart. Each sensor is a tri-axial accelerometer, but only the vertical and horizontal measurements were used. In the IQML processing, the total number of sensors was 85, and the model order was $P = 3$. In Fig. 16(a), there are two dispersion curves visible with Mode-0 being the stronger mode. The portion of the spectrum in the frequency range greater than 766 Hz and with velocities between 400 m/sec and 450 m/sec seems to be related to the pressure wave. The pressure wave is the fastest body wave, and should appear at higher frequencies. In Fig. 16(b), the polarization ellipses for the Rayleigh wave (mode-0) are shown. Mode-0 is the Rayleigh wave with a retrograde elliptical polarization as shown in Fig. 16(b). Mode-1 is a leaky surface wave with prograde elliptical polarization as in Fig. 16(c) [60].

The two modes are also extracted for a single sensor for both channels, and shown in Figs. 17 and 18, respectively. The collected original data is also plotted in these figures, to show which portion the extracted pulse belong to. The two modes were also extracted and reconstructed in the time domain for the first 60 sensor positions. The results are shown in Figs. 19(a) and (b) for the horizontal channel. By comparing to Figs. 15(a) and (b) we can see which portions of the original sensor data correspond to these two different modes. It seems clear that we are able to separate the Rayleigh wave from the collected data in both of the channels.

3.4 Applications

3.4.1 Processing in the Presence of Buried Landmines

The IQML processing has been applied to data collected in the presence of buried targets using a single-axis sensor that records only the vertical channel [61–63]. Consider the setup shown in Fig. 20(a), where the sensor array lies between the source and the target. The target in this case is a VS-1.6 AT land mine buried at a depth of 8 cm. The array consists

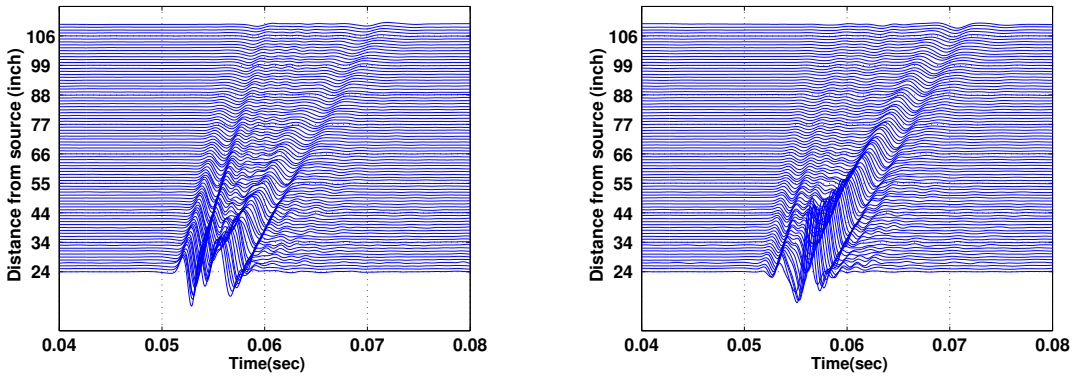

(a) (b)

Figure 15: Field data (space-time) for, (a) horizontal channel, $s_x(\mathbf{x}, t)$, (b) vertical channel, $s_z(\mathbf{x}, t)$.

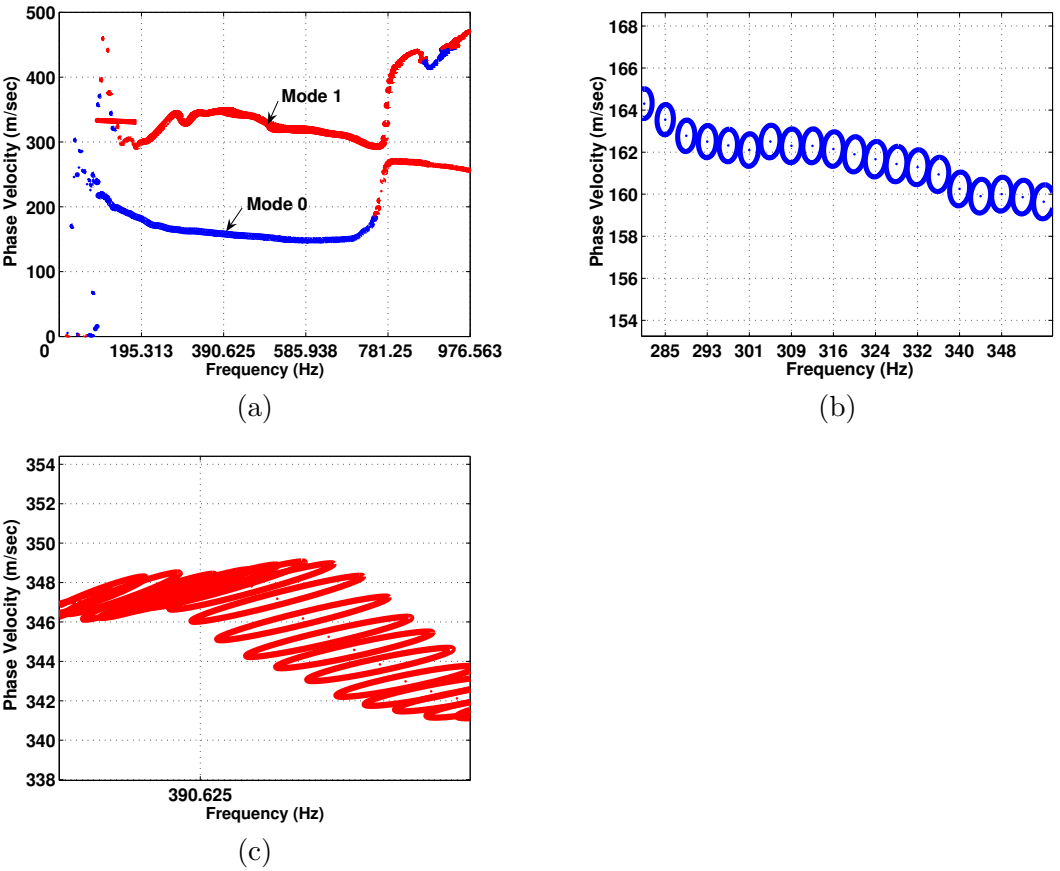

(a) (b)

(c)

Figure 16: (a) Multi-modal dispersion curves. (b) Polarization ellipses for Rayleigh wave (Mode-0). (c) Polarization ellipses for Leaky surface wave (Mode-1).

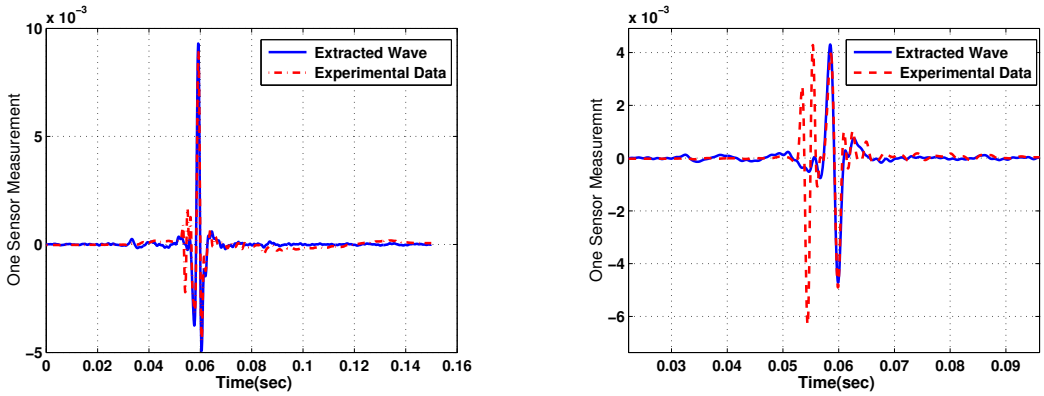

(a) (b)

Figure 17: Extraction of Mode-0 versus the original: (a) vertical channel, (b) horizontal channel.

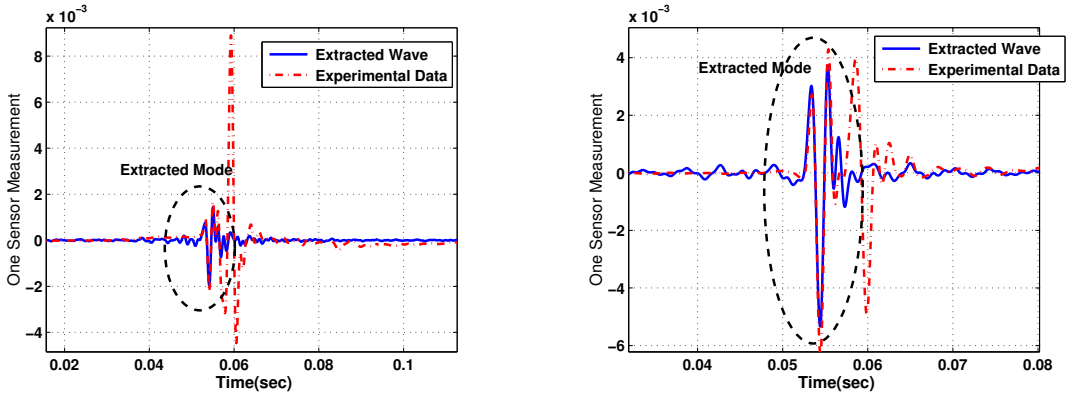

(a) (b)

Figure 18: Extraction of Mode-1 versus the original: (a) vertical channel, (b) horizontal channel.

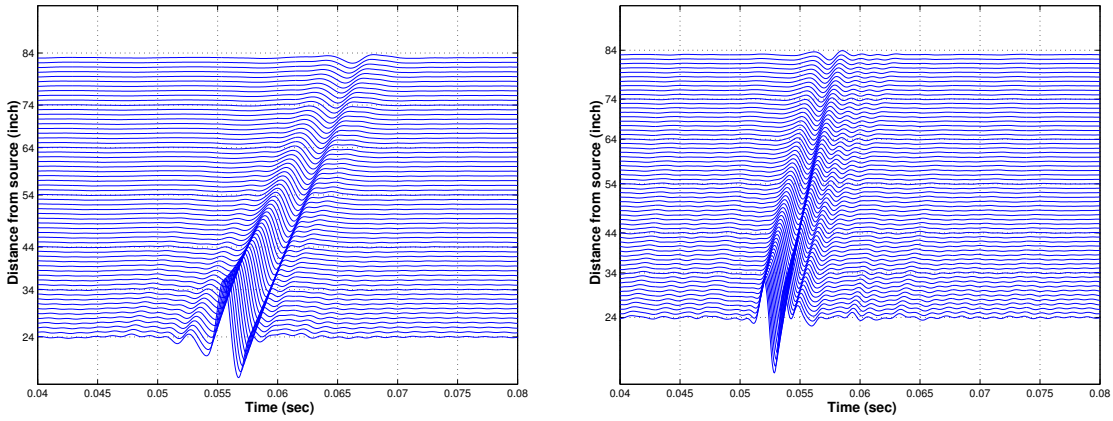

(a) (b)

Figure 19: (a) Horizontal channel reconstruction (Mode-0) for the first 60 sensor positions. (b) Horizontal channel reconstruction (Mode-1) for the first 60 sensor positions.

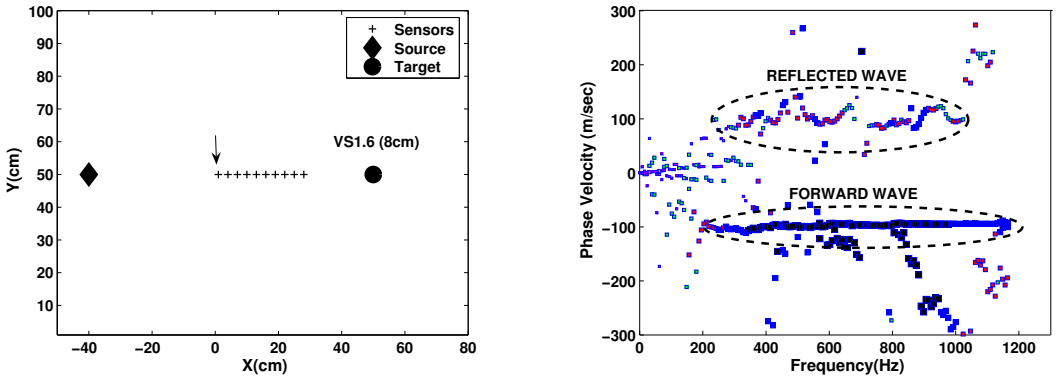

(a) (b)

Figure 20: (a) Array setup with linear array of sensors between the source and target. The first sensor position is indicated by the arrow. (b) IQML spectrum analysis: reflected waves have positive velocity; forward waves, negative velocity.

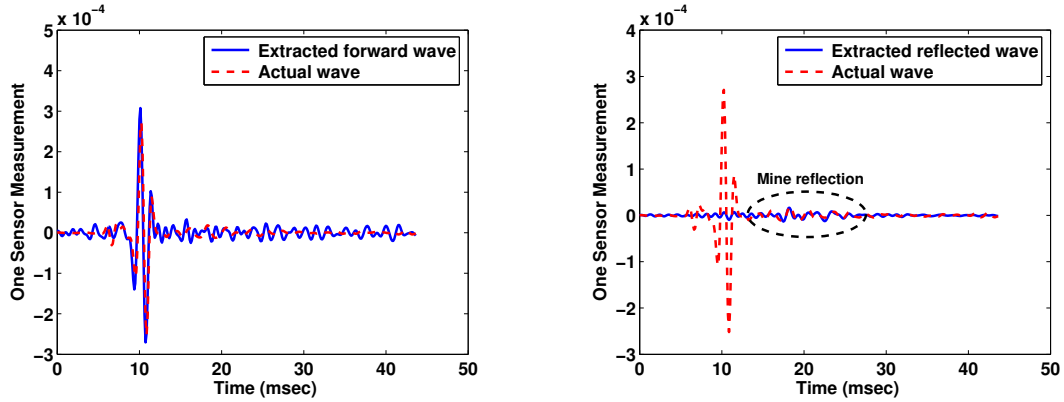

(a) (b)

Figure 21: Extracted wave at one sensor only: (a) Forward wave and original. (b) Reflected wave and original.

of ten sensors (ground contacting accelerometers) with an inter-sensor spacing of 3 cm. The IQML-derived spectrum analysis plot of this collected data is shown in Fig. 20(b). The IQML analysis easily separates the forward and reflected waves on the basis of positive and negative velocities, or equivalently, positive and negative wavenumbers. These waves are identified in velocity-frequency space, and then their individual parameters are extracted, followed by reconstruction in the space-time domain using (44). The extracted forward and reverse waves at the first sensor are shown in Fig. 21. These signal reconstructions show how well the IQML method is able to separate these waves.

The effectiveness of this extraction can be demonstrated with an another example using

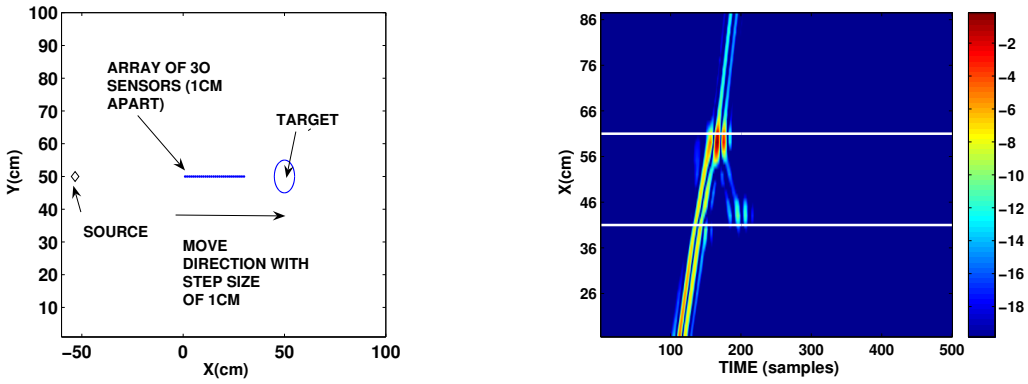

(a) (b)

Figure 22: (a) Array setup. (b) VS-1.6 mine (20 cm diameter) buried at a depth of 5 cm. Front and back edges of the mine are denoted by horizontal white lines (dB scale). Space-time plots of the collected data at the center sensor for all window positions.

a VS-1.6 anti-tank mine buried at a depth of 5 cm. In this example, a linear array consisting of 31 sensors is moved 1 cm at a time across the target, as shown in Fig. 22(a). At each array position the extracted waves are reconstructed at the middle sensor (the 16th) and are saved for use in the final plot. The collected data at the center sensor for all window position is shown in Fig. 22(b), where the front and back edges of the mine are shown by two horizontal lines. The VS-1.6 mine is an anti-tank (AT) mine with a diameter of 20 cm. The extracted forward wave is shown in Fig. 23(a), and the extracted reflected wave in Fig. 23(b). All the images are shown on a 20 dB scale, and each image is normalized to its own maximum value so that its peak corresponds to 0 dB. In this example, the extracted reflected wave shows a very strong reflection where the mine is located.

3.4.2 Rayleigh Wave Phase, Group and Effective Phase Velocity Estimates

One consequence of dispersion in surface waves is that the group and phase velocities are different, with the group velocity being slower than the phase velocity. The phase velocity is given by $\omega/k_p(\omega)$, and this has been used to plot dispersion curves. However, the group velocity can also be calculated directly from the IQML analysis. The group velocity is given by [26, 73],

$$V_g = \left(\frac{d}{d\omega} k(\omega) \right)^{-1} \tag{45}$$

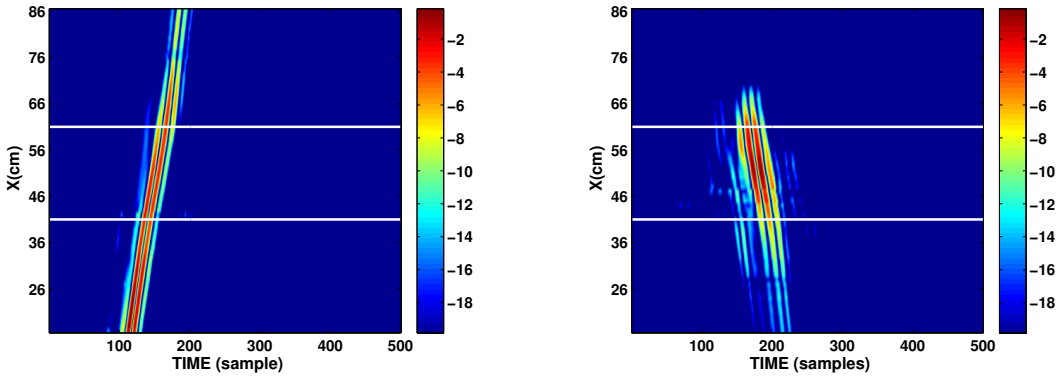

Figure 23: VS-1.6 mine (20 cm diameter) buried at a depth of 5 cm. Space-time plots on a dB scale (a) extracted forward wave (b) extracted reflected wave.

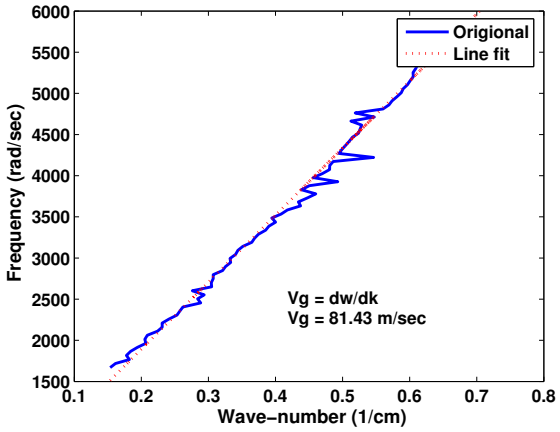

Figure 24: Group velocity estimate obtained from the IQML spectrum analysis.

where $k(\omega)$ is the wavenumber estimate at frequency ω. These values can be calculated directly from the IQML analysis. A line is fit to the mode-shape plot, and the slope of the line is the group velocity estimate. For the VS-1.6 example above, the (ω, k) plot is shown in Fig. 24. A line is fit to this plot and the slope of the line gives a value of 81.43 m/sec for the group velocity estimate.

Next we will look at the effective velocity calculation. For a heterogenous medium the mathematical formulation of the Rayleigh waves propagation is very complex. As shown in previous sections, that several Rayleigh wave modes may propagate in a vertically heterogenous medium at a given frequency ω. For the case of layered medium the phase velocity comes from the mode superposition and for this reason it is often called effective or apparent

Table 2: Inversely dispersive soil profile.

Thickness (cm)	$V_s(m/sec)$	$V_p(m/sec)$	Density (kg/m^3)
2.5	90	250	1400
2.5	60	250	1400
2.5	70	250	1400
2.5	100	250	1400
∞	110	250	1400

phase velocity [26, 36, 38]. The effective Rayleigh phase velocity can be found by using

$$\hat{V}_R(r,\omega) = 2\omega \frac{\sum_{i=1}^{M}\sum_{j=1}^{M}[A_i A_j \cos[r(k_i - k_j) + (\theta_i - \theta_j)]]}{\sum_{r=1}^{M}\sum_{s=1}^{M}[A_r A_s (k_r + k_s)\cos[r(k_r - k_s) + (\theta_r - \theta_s)]]} \tag{46}$$

where M is the number of modes, and r is the distance from the source. The complex amplitude and wavenumber obtained from IQML processing are used in calculating the effective velocity. The effective phase velocity is a function of distance r from the source. However, when estimating effective velocity averaging over a specific range of r is applied. Two profiles will be used for effective velocity calculations. The first is the normally dispersive profile given in Table 1, and the other is the inversely dispersive profile given in Table 2. The normal profile is the one in which stiffness is monotonically increasing with depth, and the inversely dispersive profile is the one in which there exist stiffer layers over softer ones. The effective velocity plots are shown in Figs. 25(a) and (b) for two profiles. For normally dispersive profile, the effective velocity is same as the fundamental (dominant) mode, and the behavior for inversely dispersive profile is different. In this effective phase velocity is same as fundamental mode velocity at lower frequencies, while as frequency increases and more modes participate to the definition of the wave field. The effective phase velocity is now a combination of the individual mode phase velocities.

3.4.3 Dispersion Curve based Inversion of Shallow Seismic Structures

Rayleigh waves are not dispersive in a homogenous isotropic linear halfspace, i.e. their velocity is a function of mechanical properties of the medium, but it is not a function of frequency. In a stratified medium, because of dispersion the phase velocity of Rayleigh

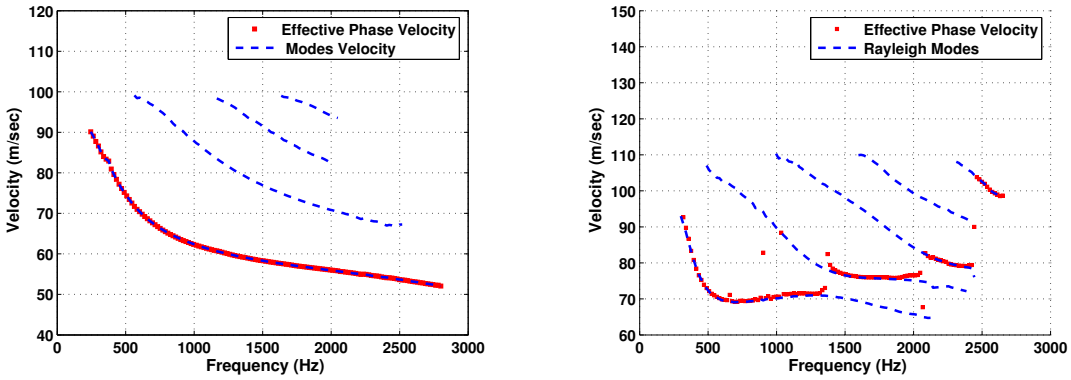

(a) (b)

Figure 25: Effective velocity estimation, (a) normally dispersive profile (Table 1), (b) inversely dispersive profile (Table 2)

.

wave is a function of frequency. A stratified medium is usually modeled as a stack of homogenous linear elastic layers. Each of the layers is characterized by its density and its S and P wave velocities. Given the set of medium parameters $[\rho(z), V_p(z), V_s(z)]$ defining the material properties of a site, the problem of determining the dispersion curve associated with that site is often referred to as the Rayleigh direct, or forward, problem. Conversely, if the dispersion curve is known, then the problem of determining the unknown medium parameters $[\rho(z), V_p(z), V_s(z)]$ defines the Rayleigh backward, or inverse, problem [26, 36, 38]. Thus the dispersion curve estimated by IQML processing can be used to determine the mechanical parameters of the medium by inversion [41]. From IQML we get multi-mode dispersion curves, however, the one related to the fundamental (dominant) mode is used for inversion. The inversion algorithm used is called Occam's algorithm [36, 38]. In this algorithm, it is assumed that number of layers in a stratified medium is known, and the parameters to be estimated are the P and S wave velocities, the density ρ, and the thickness h. This algorithm can be summarized as follows: given the dispersion curve and its associated uncertainty, find the smoothest profile of model parameters subject to the constraint of a specified misfit between observed and predicted data [36, 38]. Since the Rayleigh wave phase velocity is relatively insensitive to changes in P-wave velocity, only the S-wave velocity profile is determined by this algorithm.

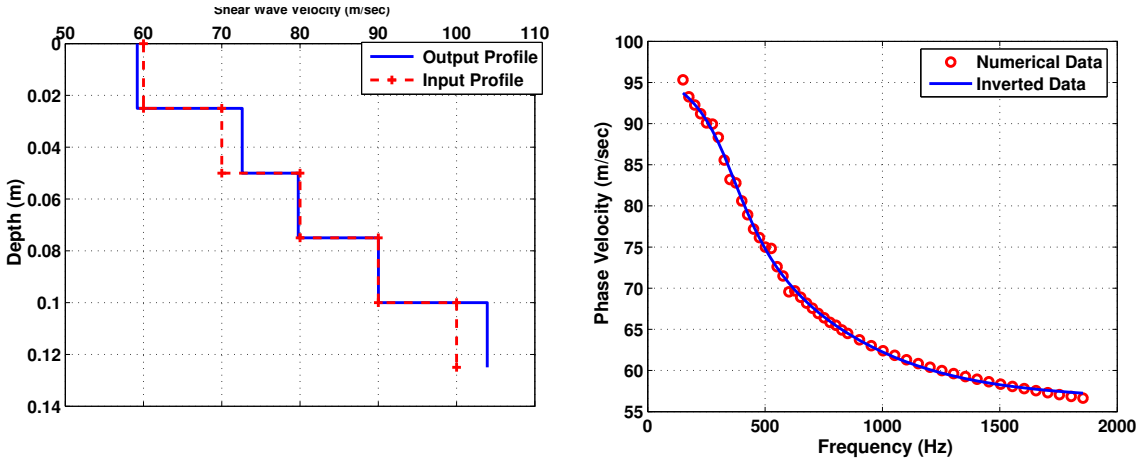

(a) (b)

Figure 26: Result of inversion for numerical data, (a) S-wave velocity profile vs. depth, (b) observed (circle) and predicted (solid line) dispersion curve for fundamental mode.

The inversion algorithm has been applied to the data whose soil profile is given by Table 1, and whose dispersion curve is shown in Fig. 12(a). The fundamental or dominant mode for this dispersion curve is extracted and it is used to determine the S-wave profile. The estimated S-wave velocity profile is shown in Fig. 26(a), and has a maximum error of 4 m/sec. The experimental and predicted phase velocity plots are in close agreement, as shown in Fig. 26(b).

The inversion algorithm was also performed for the fundamental mode of the experimental data whose dispersion curve is given by Fig. 16(a). In this case the layer thickness increases with depth. As the near-surface layers are interrogated by higher frequencies, and therefore shorter wavelengths, smaller layer thickness were assumed closer to the surface. The inverted S-wave profile is shown in Fig. 27(a), while the experimentally measured and inverted Rayleigh wave velocities as a function of frequency are compared in Fig. 27(b). The close agreement of two curves in Fig. 27(b) indicates that the inverted properties are within the prescribed accuracy of inversion process. On the other hand, the layer thickness estimates exhibit more variance.

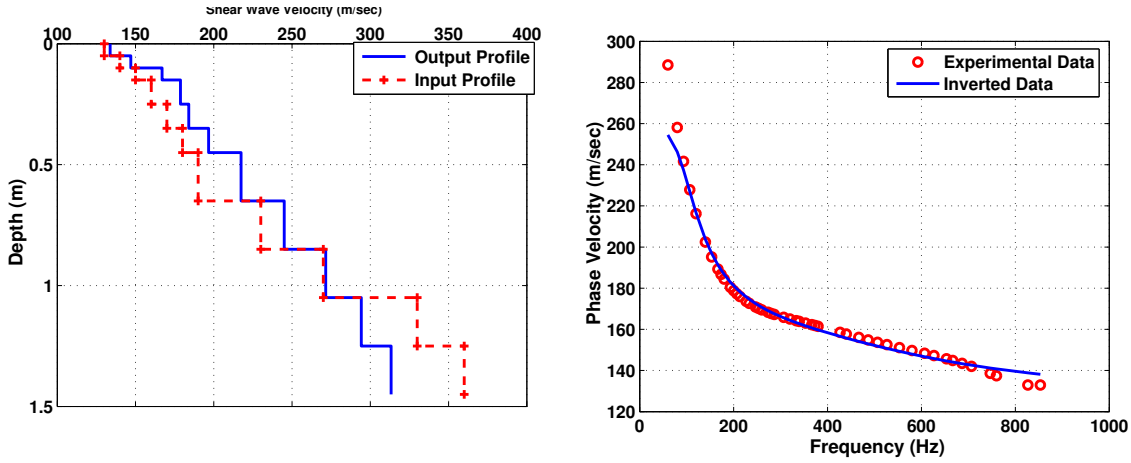

(a) (b)

Figure 27: Result of inversion for experimental data, (a) S-wave velocity profile vs. depth, (b) observed (circle) and predicted (solid line) dispersion curve for fundamental mode.

3.5 Conclusions

In this chapter, a new method is proposed for multi-channel spectrum analysis of surface waves using a vector form of the IQML algorithm. Using this method we are able to separate not only the different modes and their polarization behavior, but we can also reconstruct these modes in the space-time domain. From collected field data we have succeeded in identifying and reconstructing the mode that is the Rayleigh wave. For landmines, the same algorithm for single channel data has been applied successfully in recovering the reflected Rayleigh wave. The dispersion curves obtained from this analysis can be used in estimating various Rayleigh wave velocities, and in determining the mechanical parameters of a layered medium by inversion.

CHAPTER IV

NEW ARRAY PROCESSING BASED IMAGING ALGORITHMS FOR FIXED LINEAR ARRAYS

4.1 Introduction

The imaging algorithms presented in this chapter are based on the concept of seismic sonar. A seismic wave is launched from a source, travels through the soil and interacts with targets. The reflections from the targets can be measured by placing receiving sensors on the surface. This type of active array system, first proposed in [64], is shown in Fig. 28. This active array system has a multi-static setup, with an array of sources and receivers arranged in the form of a uniform linear array. This array can be mounted on a moving platform like a truck as shown in the Fig. 28. Both imaging algorithms in this chapter use a multi-static response matrix formed in the frequency domain [6, 7]. One algorithm is based on time-reverse imaging, and the other on the CLEAN algorithm. Both of these algorithms perform satisfactorily in detecting landmines. However, for good resolution both require a large receiver array aperture, which means more measurements. Moreover, they also require an array of sources to build up a multi-static response matrix.

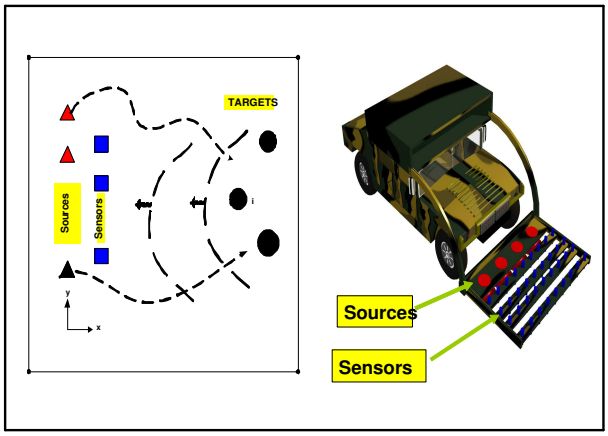

Figure 28: Active array system.

4.2 Imaging based on Near Field DOA and Range Estimate by using a 2-D MUSIC Algorithm

The first imaging algorithm is based on the theory of time reversal. Time reversal is the principle that most physical laws of nature are invariant for time reversal, i.e., when time t is replaced by $-t$, most physical laws remain unchanged. Physically this means that by time reversing, a particle will retrace its original path or trajectory [24]. Based on this fact, systems have been built to received reflections and focus them back to their source. The reflected data is recorded, time reversed and launched back into the medium. The principle of Time Reversal guarantees that it will focus back on the targets. This is the basis for experimental time reversal [25, 35, 52, 55]. Time-reverse imaging is somewhat different in the sense that scattering from targets is recorded on the sensors, but then back propagated numerically. Narrow-band or single frequency MUSIC-based time-reverse imaging algorithms have been proposed in the literature for point-like targets [13, 42, 54, 56]. For these systems, an active array system is used to probe the medium by launching a wave, and recording the waves scattered from targets at a receiver array. The goal is to detect and image the positions of targets by using the received reflections. The MUSIC-based algorithm requires an estimate of the Green's function of the medium. In signal processing terms, the Green's function corresponds to the impulse response. In wave theory, the Green's function is the solution to the Helmoholtz equation with constant wave speed. Most algorithms proposed in the literature assume a homogeneous medium, i.e., constant velocity. However, soil is an example of non-homogeneous medium, which is highly dispersive. In [8] we used an estimate of the Green's function based on the Rayleigh wave only, since this was the only wave that can be measured by sensors on the surface. This is an approximation for the Green's function, but it produces reasonable results.

We propose a different algorithm, which utilizes the same theory and setup as time reversal. In our setup, because of the attenuation and dispersion of surface elastic waves, the array cannot be placed very far from the targets, so we have a near field imaging problem. For passive array systems, several algorithms have been proposed for DOA and range estimates for near field sources. Most of these algorithms require an estimate of the

spatial covariance matrix obtained from the sensor data. Using an active array system a time-reversal matrix can be built, and recently it has been proven that this time-reversal matrix can be interpreted as a covariance matrix [13, 42, 56]. We exploit this link to derive a high resolution imaging algorithm based on a 2D-MUSIC algorithm already proposed for estimating the near field DOA and range parameters [32]. We will demonstrate that the method obtains the correct image for synthetic data generated from a FDTD simulation and also from experimental laboratory data [61, 63].

4.2.1 Time Reversal Matrix and Near Field DOA and Range Estimates

Using an active array system of N sources and N receivers, an $N \times N$ response matrix, $\mathbf{K}(\omega)$ can be formed after performing N separate transmit-receive operations. The system geometry is shown in Fig. 29. Measurements are made in the time domain, but processing is done in the frequency domain at a single frequency. The response matrix at a frequency ω can be given by [56],

$$\mathbf{K}(\omega) = \mathbf{H}_1(\omega)\mathbf{D}(\omega)\mathbf{H}_2(\omega) \tag{47}$$

where $\mathbf{H}_2(\omega)$, $\mathbf{D}(\omega)$ and $\mathbf{H}_1(\omega)$ model the propagation from the transmitter array to the targets, the scattering matrix, and the propagation from targets back to the receive arrays, respectively. If there is no multiple scattering then $\mathbf{D}(\omega)$ is a diagonal matrix. The elements of the propagation matrices are given by the Green's function. The time-reversal matrix is formed at a single frequency as $\mathbf{K}^H(\omega)\mathbf{K}(\omega)$. In [56], it was proved that the time reversal matrix can be interpreted as a covariance matrix used in standard passive array techniques. This interpretation led us to derive an imaging algorithm based on near field geometry. The singular vectors and singular values of the response matrix or the time-reversal matrix can be utilized to determine the number of targets and their locations. Singular vectors are used to form a MUSIC-based imaging algorithm. However as mentioned before, these imaging algorithms require an estimate of the Green's function of the medium.

In wide-band passive sensing the received signal at frequency ω is given by

$$X(\omega) = \mathbf{A}(\omega)S(\omega) + B(\omega) \tag{48}$$

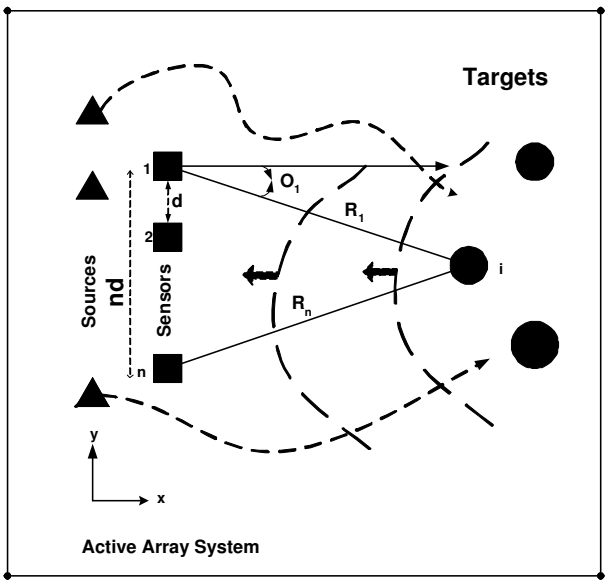

Figure 29: Near-field active array setup.

where $\mathbf{A}(\omega)$ is the steering vector matrix and $B(\omega)$ the noise matrix. For near field targets, the i^{th} column of the 3-D steering vector matrix is given by [32, 68],

$$a(r,\theta,\omega) = \left[\frac{1}{R_{i,1}}e^{j\frac{2\pi}{\lambda(\omega)}R_{i,1}}, ..., \frac{1}{R_{i,N}}e^{j\frac{2\pi}{\lambda(\omega)}R_{i,N}}\right]^T \tag{49}$$

where $R_{i,n}$ is the distance between n^{th} sensor and i^{th} target. Also from Fig. 29, the range to the i^{th} target from the n^{th} sensor with respect to the first reference sensor is

$$R_{i,n} = \sqrt{R_{i,1}^2 + n^2d^2 - 2ndR_{i,1}\sin\theta_{i,1}}, n = 2, ..., N \tag{50}$$

where d is the sensor spacing, and $(R_{i,1}, \theta_{i,1})$ are near-field parameters for target i with respect to the first sensor. If the array is steered with respect to first sensor, then

$$a(r,\theta,\omega) = \left[1, \rho_2 e^{j(\frac{2\pi}{\lambda(\omega)})(R_{i,2}-R_{i,1})}...., \rho_N e^{j(\frac{2\pi}{\lambda(\omega)})(R_{i,N}-R_{i,1})}\right]^T \tag{51}$$

where ρ_i depends on range. However, we are more interested in the phase terms. In an active array system, if a signal (impulse) is applied at transmitter n, the received scattering is the n^{th} column of $\mathbf{K}(\omega)$, and is given by

$$R_n(\omega) = \mathbf{H}_1(\omega)\mathbf{D}(\omega)H_{2n}(\omega) + B_n(\omega) \tag{52}$$

where $H_{2n}(\omega)$ is the n^{th} column of $\mathbf{H}_2(\omega)$ and $B_n(\omega)$ is the noise vector. The N columns of $K(\omega)$ are analogous to N snapshots of the target signal in passive detection. Thus,

in active arrays, the number of transmitters corresponds to the number of snapshots in passive arrays. A pseudo-covariance matrix can be built for the active array system using N measurements like (52); this interpretation as a passive sensor covariance and the link to the time-reversal matrix can be found in [56].

For the single target case, the matrix $\mathbf{H}_1(\omega)$ in (52) has only one column which is given by the illuminating Green's (steering) vector

$$\mathbf{g}(\mathbf{y}_t, \mathbf{x}, \omega) = [G(\mathbf{y}_t, \mathbf{x}_1, \omega), G(\mathbf{y}_t, \mathbf{x}_2, \omega)..., G(\mathbf{y}_t, \mathbf{x}_N, \omega)]^T \tag{53}$$

where $\mathbf{y}_t$ is the position of the target and $\mathbf{x}_i$ is the position of the i^{th} sensor. The Green's function G in 3-D is

$$G(r, r^{'}, \omega) = \frac{1}{|r - r^{'}|} e^{j\frac{\omega|r-r^{'}|}{v}} = Ke^{j\omega t^{'}} \tag{54}$$

where K is a constant, and $t^{'}$ is the time taken by a wave to travel a distance between r and $r^{'}$. The Green's vector can be written as:

$$\mathbf{g}(\mathbf{y}_t, \omega) = \left[A_1 e^{j\omega t_1}, A_2 e^{j\omega t_2}, ..., A_N e^{j\omega t_N}\right]^T \tag{55}$$

or, with respect to the first sensor (the reference sensor)

$$\mathbf{g}(\mathbf{y}_t, \omega) = \left[1, B_2 e^{j\omega(t_2 - t_1)}, ..., B_N e^{j\omega(t_N - t_1)}\right]^T \tag{56}$$

using $(R_k - R_1) = (t_k - t_1)v$, we can write (56) as

$$\mathbf{g}(\mathbf{y}_t, \omega) = \left[1, B_2 e^{j\frac{2\pi}{\lambda(\omega)}(R_2 - R_1)}, ..., B_N e^{j\frac{2\pi}{\lambda(\omega)}(R_N - R_1)}\right]^T \tag{57}$$

Thus for a single target case, the scattering received at the n^{th} column of the response matrix, corresponding to a pulse from the n^{th} transmitter is

$$R_n(\omega) = \mathbf{g}(\mathbf{y}_t, \omega)\xi(\omega)H_{2n}(\omega) + B_n(\omega) \tag{58}$$

where $\xi(\omega)$ is the scattering coefficient of the target and $\xi(\omega)H_{2n}(\omega)$ represents the scattered energy from the target. Equation (58) is analogous to (48), with $\xi(\omega)H_{2n}(\omega)$ interpreted as the target signal, and the steering vector given by (57) is the same as (51) (in term of phase), proving the link between near field active and passive sensor systems.

4.2.2 Algorithms for Near-Field DOA and Range Estimates based on Time-Reversal Matrix

After establishing the link between near field passive and active sensing, the next step is forming an estimate of the DOA and range of targets using the sensor measurements. One possible approach is to use the Fresnel approximation to rewrite the signal as a chirp signal. Then the imaging algorithm reduces to estimating the parameters of the chirp. The time-reversal matrix at a single frequency is used in place of covariance matrix, and the algorithm proposed in [68] is carried out. This algorithm produces reasonable results with small errors, but the method involves an approximation that gets worse when the target is extremely close to the array.

Another algorithm is based on a 2-D MUSIC approach for near field DOA and range estimates [32]. This algorithm gives the best results for our setup. The algorithm uses the singular value decomposition of the time-reversal matrix, $\mathbf{K}^H(\omega)\mathbf{K}(\omega)$, and searches for R_1 and θ_1. The steps are as follows:

1. Form the the response matrix $\mathbf{K}(\omega)$ and the time-reversal matrix $\mathbf{K}^H(\omega)\mathbf{K}(\omega)$ at a single frequency.

2. Perform the SVD of $\mathbf{K}^H(\omega)\mathbf{K}(\omega)$.

3. Determine the number of targets M, from the number of significant singular values of the time-reversal matrix

4. Form the noise singular vector matrix

   $\mathbf{W}(\omega) = [\mathbf{u}_{M+1}, ..., \mathbf{u}_N]$

   where $\mathbf{u}_i$ are the singular vectors of the time-reversal matrix.

5. Form the steering vector given by (51) with respect to first sensor, as a function of $[R_1, \theta_1]$, with $\rho_i = 1$

6. The M peaks of the following 2-D orthogonality measure are the estimates of the near-field parameters for M targets:

   $$\mathbf{P}(r, \theta, \omega) = \frac{1}{\mathbf{a}^H(r, \theta, \omega)\mathbf{W}\mathbf{W}^H\mathbf{a}(r, \theta, \omega)}$$

7. Repeat these steps for a band of frequencies, determined by the amplitude of the Rayleigh wave, and then average over frequency. This yields a wide-band solution.

The estimate of M, the number of targets, can be determined from the number of significant singular values, when plotted as a function of frequency. The original time reversal theory was developed for point-like targets, so there should be a one-to-one correspondence between the number of targets and the significant singular values, However for extended targets, this correspondence breaks down, and it has been shown that up to four singular values can be related to one extended target [56].

4.2.3 Numerical Simulation Results

An FDTD simulation has been used to generate data for a scenario with two different targets (landmines) buried at a depth of 2 cm in a vertically stratified soil [61]. The active array consists of 15 seismic sources (transmitters), spaced 6 cm apart, and 23 receivers, spaced 4 cm apart. The transmitted pulse is a differentiated Gaussian pulse centered at 450 Hz. A response matrix is formed by probing the medium with pulses launched from each of the transmitters, and recording the reflections which are mainly the Rayleigh wave measured at the receivers. The algorithm requires an estimate of velocity or wave-length for the Rayleigh wave versus frequency, which can be estimated very accurately using the method in Chapter 3 [9]. The number of targets can be estimated from the singular values of the response matrix, as shown in Fig. 30. A value of $M = 2$ is used for this case. Processing is done for the frequency band from 830 Hz to 1050 Hz, and then averaging is done to obtain the final estimates. This frequency range was chosen from the amplitude of the Rayleigh wave. The spectrum obtained after applying the 2-D MUSIC algorithm is shown in Fig. 31(a). The spectrum will peak at the corresponding range and DOA estimates for the two targets. These values can be extracted from the spectrum by searching over a grid for the peaks. Then the extracted values are used to obtain range and DOA estimates with respect to the first sensor, which is the reference sensor in this case. The estimated target positions are shown in Fig. 31(b).

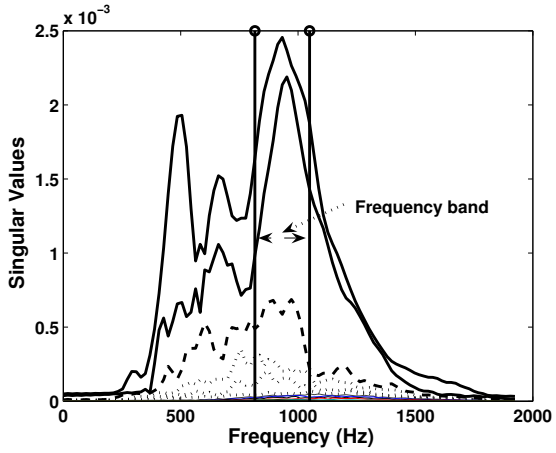

Figure 30: Singular values versus frequency (numerical). The frequency range used in the processing is shown by two vertical lines.

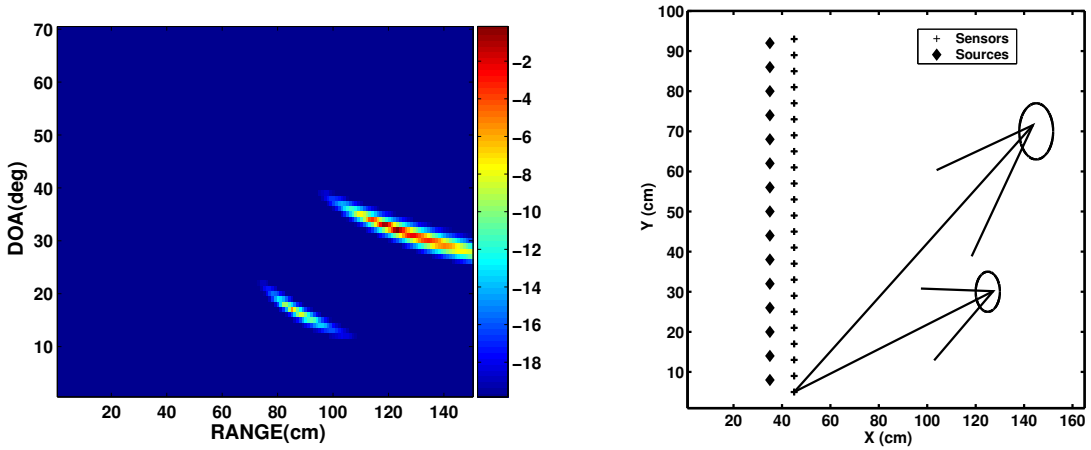

(a) (b)

Figure 31: Processing for numerical data (a) 2-D MUSIC spectrum (polar coordinate) (dB scale) (b) Target location estimates (rectangular coordinates).

4.2.4 Experimental Data Results

The new technique has also been applied to experimental data obtained in a laboratory setting [63]. The data collection scenario consists of inert landmines buried in a large sandbox; in this case, an anti-personnel mine (AP) and an anti-tank (AT) mine were buried in the sand. The AP mine is buried at a depth of 1.5 cm and the bigger AT mine is buried at 5 cm. There are 8 sources (shakers), spaced 15 cm apart. A radar-based sensor is used as a receiver, which is capable of measuring soil displacements as small as 1 nm. There are 51 receiving points, 2 cm apart. The value of M is determined from the singular values and it is found to be 4 as shown in singular values plot in Fig. 33. The estimated amplitude and phase velocity of the Rayleigh wave as a function of frequency are shown in Figs. 32(a) and (b) [9]. The plots also show the frequency range of the Rayleigh wave which is then chosen for the processing. The penetration depth of a seismic wave depends on its wavelength, with lower frequencies penetrating deep, and higher frequencies shallow. Since we have two targets at different depths, it is important that the processing range used should cover both higher and lower frequency bands. The frequency range used is 350 Hz – 820 Hz (60 discrete frequencies), and then averaging is done. The estimated 2-D MUSIC spectrum in polar coordinates is shown in Fig. 34(a). The peak values of the 2-D polar MUSIC spectrum can be used to determine the exact location of targets, as shown in Fig. 34(b).

4.2.5 Conclusions

This section shows how the link between passive and active array processing can be exploited to derive general imaging algorithms. The theory of array processing which has been developed for passive sensing, can be used for the problems of active sensing. Also the need to have a Green's function estimate which the time reverse imaging algorithm require can be eliminated. We also verified the imaging algorithm using both numerical simulation and experimental data. The algorithm successfully estimated the locations of buried targets.

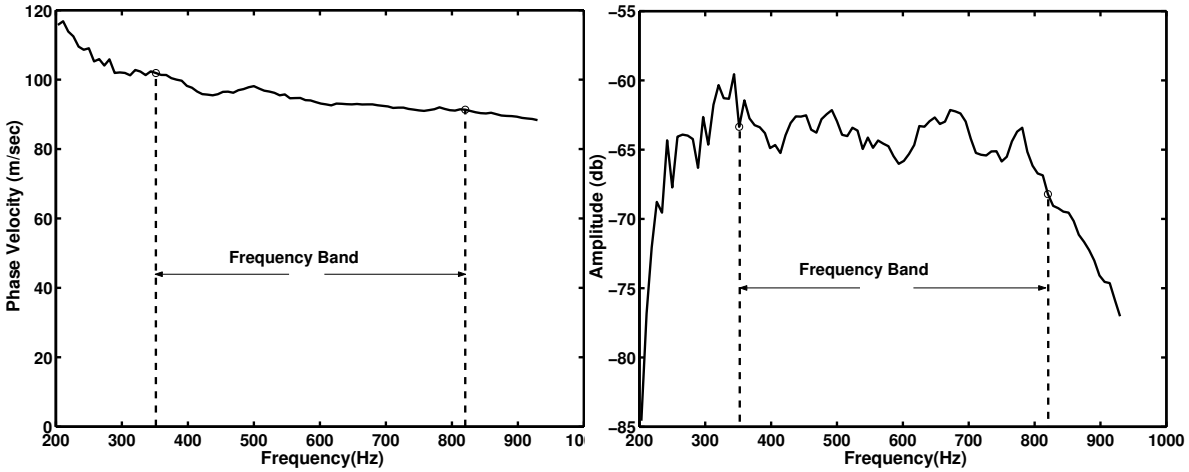

(a) (b)

Figure 32: Estimated Rayleigh wave parameters, (a) Phase velocity and (b) Amplitude versus frequency.

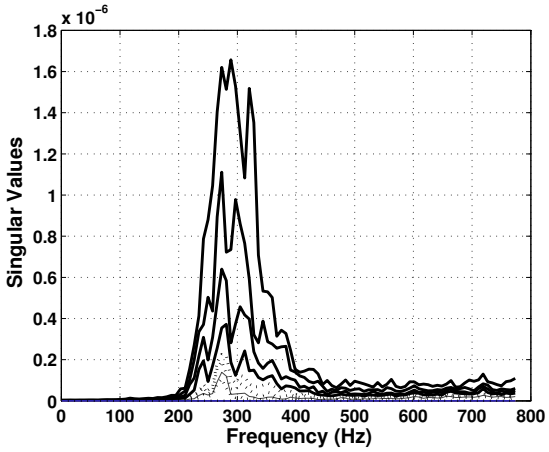

Figure 33: Singular values versus frequency for experimental data. A value of $M = 4$ is chosen from this for processing.

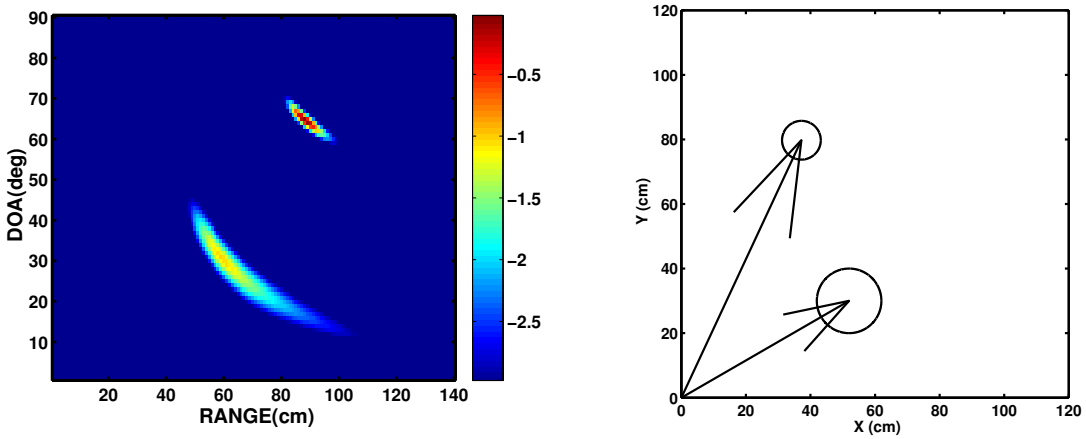

(a) (b)

Figure 34: (a) 2-D MUSIC spectrum (dB scale) (b) Target location estimates.

4.3 Imaging based on Wide-Band CLEAN/RELAX Algorithms

The CLEAN algorithm was first used in radio astronomy [29]. Later on, CLEAN and its high resolution version RELAX were modified to work for the case of wide-band DOA estimation [43,44]. Another version was also developed for aero-acoustic imaging, to detect the position of near field sources in passive sensing [70]. The same algorithm can be modified to work for the case of active detection of buried targets. Although a single source could be used, it is more robust to use an array of sources to have multiple looks at the same target. Because the problem is also a wide-band, we can exploit the fact that seismic waves penetration depth is dependent upon the wave-length. The following sections will explore the link between the array models for passive and active sensing. After establishing the link, it will be shown how the RELAX/CLEAN algorithm can be modified to work for the multi-static array case. In the end, the new imaging algorithm will be applied to experimental data collected in a laboratory setting [63].

4.3.1 Response Matrix and Link between Active and Passive Sensing

Using an active array system of N sources and N receivers, an $N \times N$ response matrix, $\mathbf{K}(\omega)$, can be formed after performing N separate transmit-receive operations. The system geometry is shown in Fig. 35. Measurements are made in the time domain, but processing

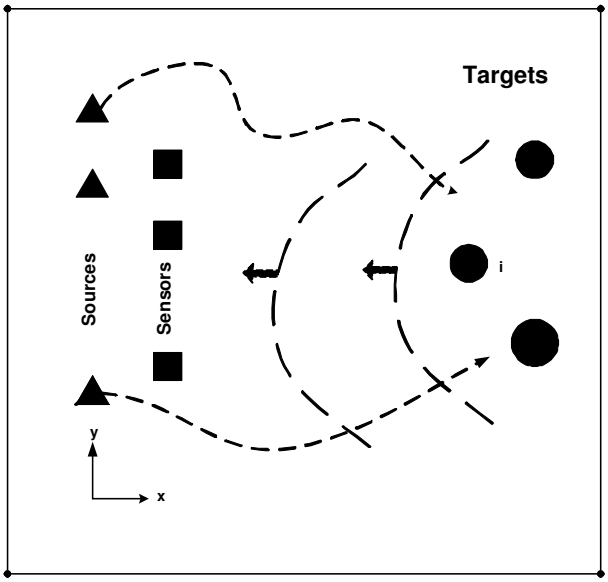

Figure 35: Near-field active array setup

is done in the frequency domain at a single frequency. A simplified response matrix model at a frequency ω can be given by [56],

$$\mathbf{K}(\omega) = \mathbf{H}_1(\omega)\mathbf{D}(\omega)\mathbf{H}_2(\omega) \tag{59}$$

where $\mathbf{H}_2(\omega)$ models the propagation from the transmitter array to the targets, $\mathbf{D}(\omega)$ the scattering matrix, and $\mathbf{H}_1(\omega)$ the propagation from targets back to the receive array. With no multiple scattering, $\mathbf{D}(\omega)$ is a diagonal matrix. The elements of the propagation matrices are given by the Green's function.

In passive sensing the received signal at frequency ω is given by

$$X(\omega) = \mathbf{A}(\omega)S(\omega) + B(\omega) \tag{60}$$

where $\mathbf{A}(\omega)$ is the steering vector matrix, $S(\omega)$ is signal from the target, and $B(\omega)$ the noise vector. For near field targets, the i^{th} column of the steering vector matrix (3-D) is given by [70],

$$a(r,\theta,\omega) = \left[\frac{1}{R_{i,1}}e^{j\frac{2\pi}{\lambda(\omega)}R_{i,1}}, ..., \frac{1}{R_{i,N}}e^{j\frac{2\pi}{\lambda(\omega)}R_{i,N}}\right]^T \tag{61}$$

where $R_{i,n}$ is the distance between the n^{th} sensor and the i^{th} target.

In an active array system, if a signal (an impulse) is applied at the n^{th} source, the

received scattering is the n^{th} column of $\mathbf{K}(\omega)$, and is given by

$$R_n(\omega) = \mathbf{H}_1(\omega)\mathbf{D}(\omega)H_{2n}(\omega) + B_n(\omega) \tag{62}$$

where $H_{2n}(\omega)$ is the n^{th} column of $\mathbf{H}_2(\omega)$ and $B_n(\omega)$ is the noise vector.

For the single target case, the matrix $\mathbf{H}_1(\omega)$ in (62) has only one column which is given by the illuminating Green's vector

$$\mathbf{g}(\mathbf{y}_t, \mathbf{x}, \omega) = [G(\mathbf{y}_t, \mathbf{x}_1, \omega), G(\mathbf{y}_t, \mathbf{x}_2, \omega)..., G(\mathbf{y}_t, \mathbf{x}_N, \omega)]^T \tag{63}$$

where $\mathbf{y}_t$ is the position of the target and $\mathbf{x}$ is the position of the receivers. The Green's function G for a 3-D space is

$$G(r, r^{'}, \omega) = \frac{1}{|r - r'|} e^{j\frac{2\pi}{\lambda(\omega)}|r-r^{'}|} \tag{64}$$

Thus for the single target case, the scattering received at the n^{th} column of the response matrix, corresponding to a pulse from the n^{th} transmitter is

$$R_n(\omega) = \mathbf{g}(\mathbf{y}_t, \omega)\xi(\omega)H_{2n}(\omega) + B_n(\omega) \tag{65}$$

where $\xi(\omega)$ is the scattering coefficient of the target and $\xi(\omega)H_{2n}(\omega)$ represents the scattered energy from the target. Equation (65) is analogous to (60), with $\xi(\omega)H_{2n}(\omega)$ interpreted as the target signal; the steering vectors as given by (61) and (63) have the same form, thus proving the link between near field active and passive sensor systems.

4.3.2 Wideband Multi-Static RELAX/CLEAN Algorithms

We will start by defining a multi-static response matrix at frequency ω. A simplified model is

$$\mathbf{K}(\omega) = \mathbf{H}_1(\mathbf{p}, \omega)\mathbf{S}(\omega) \tag{66}$$

where we have replaced $\mathbf{D}(\omega)\mathbf{H}_2(\omega)$ by the target signal $\mathbf{S}(\omega)$, and $\mathbf{p}$ is the position vector that we are trying to estimate. Using the l frequencies in the range where the Rayleigh wave has enough energy [9], a least-squares criterion can be formed [70]

$$C = \sum_{l=1}^{L} [\|\mathbf{K}(\omega_l) - \mathbf{H}_1(\mathbf{p}, \omega_l)\mathbf{S}(\omega_l)\|_F]^2 \tag{67}$$

where $\|.\|_F$ denotes the Euclidean norm (Frobenius norm), since $\mathbf{K}(\omega)$ is a matrix. Another version of multi-look RELAX (M-RELAX) was also proposed in [27] by treating each look direction independently and then summing them to form the final solution. However, in this algorithm all the look directions are combined in a single response matrix. The positions of targets which are embedded in the propagation model $\mathbf{H}_1(\omega)$ can be estimated as a solution of this minimization problem. However, it is also necessary to estimate the target signal. To minimize C, first we fix the position $\mathbf{p}$ and solve for target signals $s(\omega_l)$ at each of the l frequencies. If there are N sources, then there will be N versions of these target signals. The least-squares estimate for each target signal is given by

$$\hat{\mathbf{S}}(\omega) = (\mathbf{H}_1(\mathbf{p},\omega)\mathbf{H}_1(\mathbf{p},\omega))^{-1}\mathbf{H}_1(\mathbf{p},\omega)\mathbf{K}(\omega) \tag{68}$$

Then we substitute this estimate into (67), and form the following minimization problem

$$\hat{\mathbf{p}} = \arg\min_{\mathbf{p}} \sum_{l=1}^{L} \|[\mathbf{I} - \frac{\mathbf{H}_1(\mathbf{p},\omega_l)\mathbf{H}_1^H(\mathbf{p},\omega_l)}{\mathbf{H}_1^H(\mathbf{p},\omega_l)\mathbf{H}_1(\mathbf{p},\omega_l)}]\mathbf{K}(\omega_l)\|_F^2 \tag{69}$$

The RELAX/CLEAN algorithm can be used to perform this minimization, see [70] for details.

4.3.3 Processing of the Experimental Data

The algorithm has been applied to experimental data obtained in a laboratory setting. In this case, an anti-personnel mine (AP) and an anti-tank (AT) mine were buried in the sand. The active array setup, target position and frequency range used in processing is the same as in Section 4.2.4.

Since the setup has a 2-D geometry, the propagation model uses a 2-D Green's function given by

$$G(r, r', \omega) = \frac{i}{4} H_0^{(1)} \left(\frac{\omega}{v(\omega)} |r - r'| \right) \tag{70}$$

where $H_0^{(1)}$ is the Hankel function of zero order and first kind. For the RELAX algorithm the number of targets used is two, and the algorithm was run for ten iterations, but it seems to converge in just a few iterations, with location estimates obtained as the minimizer of (69). The target location estimates, and also the coordinates of targets obtained in each

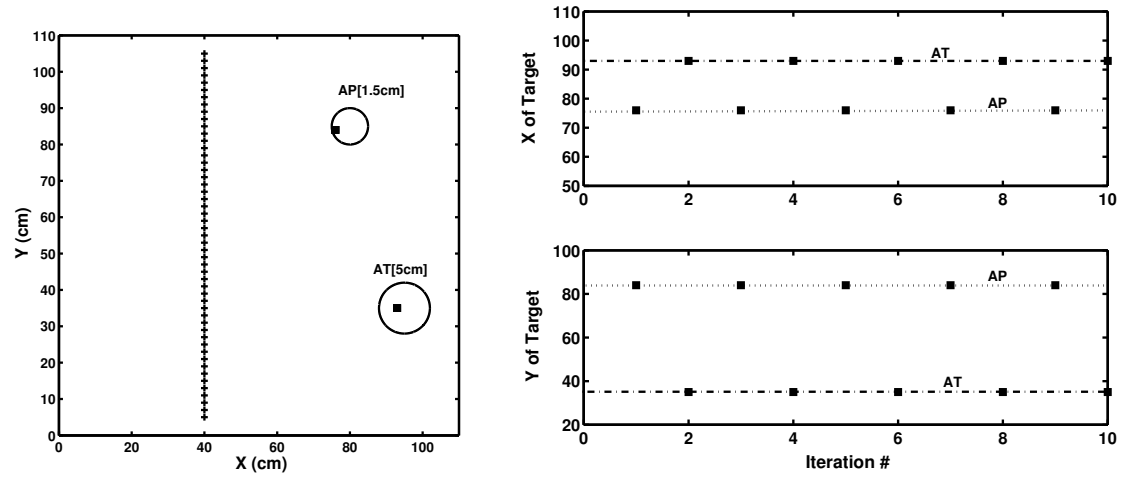

(a) (b)

Figure 36: RELAX (a) Location estimates for two target case (b) Target coordinates. At each iteration algorithm find one target position, and at next it find the other. Correct center position of the target is shown by dotted line, and estimates are given by squares.

iteration are shown in Figs. 36(a) and (b). The grid size used in the search is (60×100) cm, with a step size of 1 cm. The algorithm was run for 60 frequencies, and the minimum was found within this search area. The results for the CLEAN algorithm are shown in Figs. 37(a) and (b). CLEAN is an iterative algorithm, in which at each iteration some fraction (0.1) of the previously estimated signal is subtracted out. The results in Fig. 37(b) indicate that algorithm tends to diverge if run for too many iterations, e.g., after only five iterations. At each iteration the algorithm gives the coordinate of the strongest target, and then removes all (RELAX) or some portion (CLEAN) of this target contribution. Therefore, at the next iteration the algorithm finds the next strongest target (if one exists). This causes an alternating behavior in the coordinate estimate as shown in Figs. 36(b) and 37(b), respectively.

Another interesting result is obtained when the landmine is surrounded by buried rocks. A small AP mine was buried at the depth of 1.5 cm surrounded by some rocks. Figure 38(a) shows the mine and rock locations with sand removed. The image can be formed of the surface as a function of position $\mathbf{p}$ as

$$\mathbf{SURF}(\mathbf{p}) = \sum_{l=1}^{L} \left\| \left[\mathbf{I} - \frac{\mathbf{H}_1(\mathbf{p},\omega_l)\mathbf{H}_1^H(\mathbf{p},\omega_l)}{\mathbf{H}_1^H(\mathbf{p},\omega_l)\mathbf{H}_1(\mathbf{p},\omega_l)} \right] \mathbf{K}(\omega_l) \right\|_F^2$$

The minimizer of this function (over a grid) is the location estimate. The inverse of this

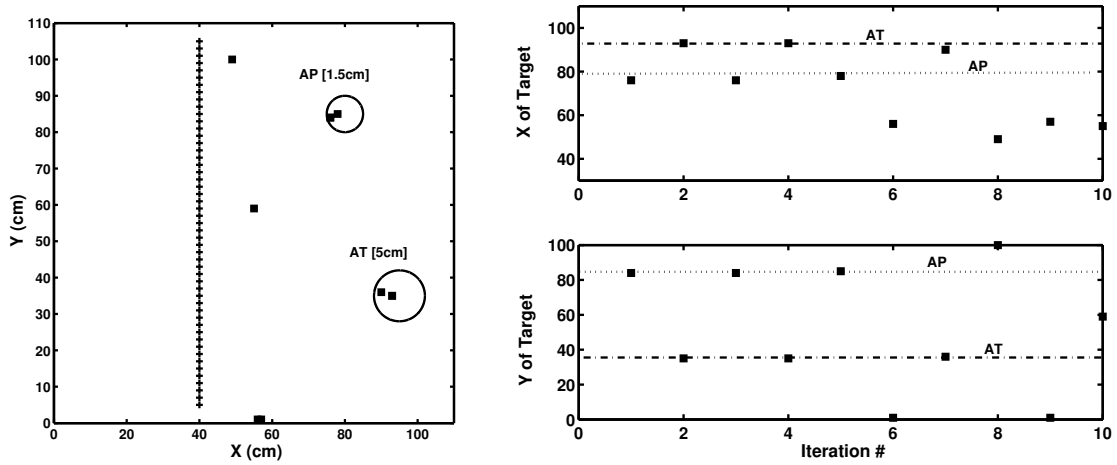

(a) (b)

Figure 37: CLEAN (a) Location estimates for two target case (b) Target coordinates. At each iteration algorithm find one target position, and at next it find the other. Correct center position of the target is shown by dotted line, and estimates are given by squares.

surface is plotted in Fig. 38(b), at the first iteration of the CLEAN algorithm. The peak location at the coordinates (36,46) cm is the correct estimate of the target's location, even in the presence of rocks. The CLEAN algorithm is ran for ten iterations, and location estimates for these iterations are shown in Fig. 38(c). Only first two or three estimates are correct, before the algorithm has completely removed the contribution from the array of the most dominant target, which is mine in this case.

4.3.4 Conclusions

In this section, we modified the RELAX and CLEAN algorithms to work for the detection of passive buried targets using seismic waves. In addition, we have shown how the methods work for a multi-static active array system. Finally, the algorithm was successfully applied to experimental data obtained in a laboratory setup.

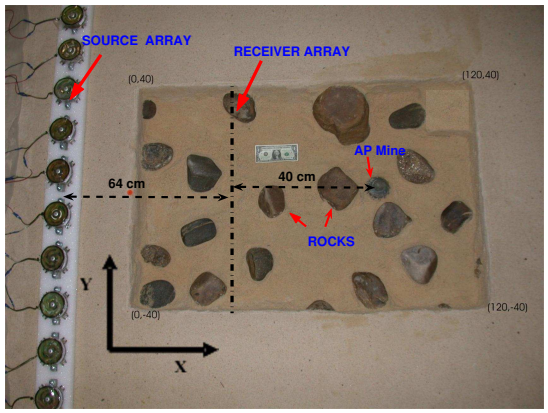

(a)

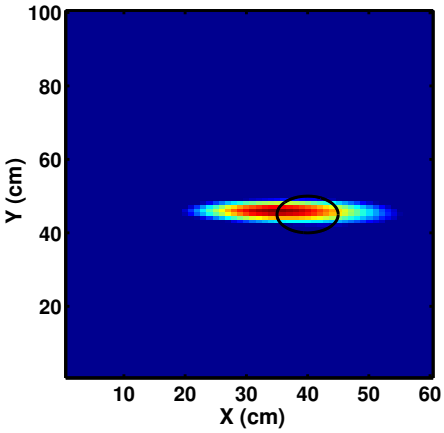

(b)

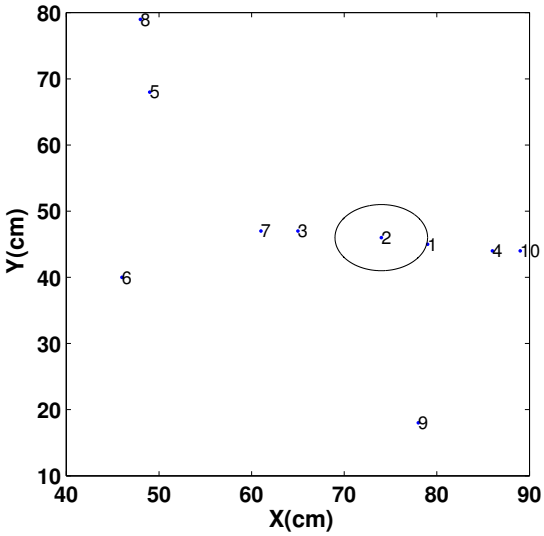

(c)

Figure 38: Processing in the presence of rocks. (a) Experimental setup showing position of the source and receiver arrays. The AP mine is surrounded by many rocks. (b) CLEAN function over the search grid at the first iteration. (c) The target location estimates for first ten iterations of CLEAN. Only first two or three gives the true location estimates, before algorithm diverges.

CHAPTER V

ALGORITHM FOR OPTIMAL MANEUVERING OF SEISMIC SENSORS

5.1 Introduction

In the previous chapters, we have introduced existing imaging algorithms and proposed some new ones to locate the landmines using seismic waves. These methods present solutions with satisfactory mine detection probabilities. However, all these imaging methods are time consuming, and expensive measurements are taken over either a large 2-D grid, or with uniform linear array. Both need large apertures to have sufficient image resolution over the space of interest, which means more measurements. The existing imaging algorithm is introduced in Section 1.1.2. In this, once a complete image is formed from a large data set, it is then searched to find targets [11]. However, to image any single target, only a small subset of the measurements is actually required, but we do not know this subset ahead of time. Therefore, if we want to reduce the time or resources needed to localize a target, we can use maneuvering receiver(s) to take the minimum number of measurements needed, if we can develop an adaptive algorithm to find the best receiver positions. With each new measurement, we want to maximize the information gained about the target. In our case, we use a maneuvering 3×3 array to create an efficient system to detect and locate mines. In the method proposed here, any one image, created at successive measurements, has low resolution. However, as the array maneuvers, the cumulative imaging operation improves the resolution around the true mine location. Hence, even with a small array we can overcome the problem of low resolution, by increasing the effective aperture by using cumulative imaging.

The array movement is based on the theory of optimal experiments [23]. Starting with a 2-D sensor array with known relative positions, an initial estimate of the target location is

made. Then, the variance of the location estimate is calculated from the Fisher information matrix (FIM). Based on the expected value of the FIM, the next optimal array position is determined by using the theory of optimal experiments [23, 45]. The search for the optimal array position maximizes the determinant of the Fisher information matrix. The two steps involved in the maneuver strategy for a mobile array of sensors are shown in Figs. 39 a and b.

The organization of this chapter is as follows. Section 5.2 formulates the problem and the data model for seismic signals. Section 5.3 describes the algorithm for estimating the target position along with performance bounds. Section 5.4 describes how the theory of optimal experiments is used to find the next array position. Section 5.5 describes the results of applying the algorithm to experimental data collected in a laboratory settings [63].

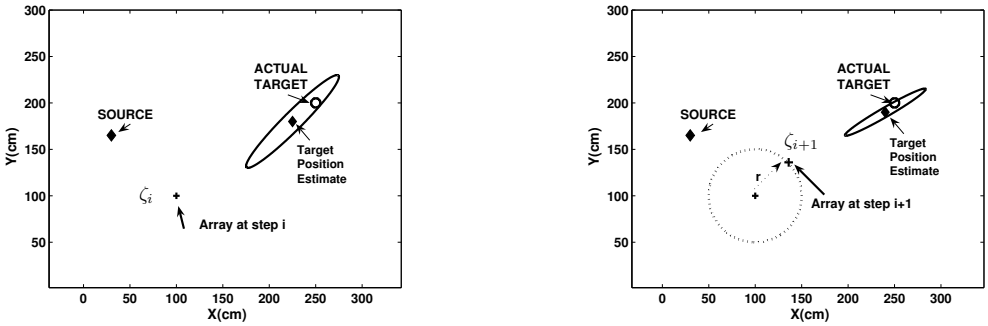

Figure 39: Algorithm mechanics illustrated: (a) Source generates a probing pulse. The waves are reflected from a target and are collected by means of an array. At step i, the target position z_i is estimated when the array center is at ζ_i (b) Estimate the next array position ζ_{i+1} by using the estimated target position z_i and the constrained cumulative Fisher information matrix measure.

5.2 Data Model for active sensing

Consider a single seismic source and an array of P seismic receivers, where the source and receivers lie in the same surface plane. Assume that there are K targets. We model the soil as a highly dispersive medium with frequency dependent velocity. Hence, the signal processing is done in the frequency domain, even though the measurements are taken in the time domain.

The received seismic data at frequency ω can be written as

$$\mathbf{y}(\omega) = \mathbf{G}(\omega)\mathbf{D}(\omega)\mathbf{g}_1(\omega) + \mathbf{n}(\omega), \tag{71}$$

where $\mathbf{g}_1(\omega)$ is a $K \times 1$ vector that models the propagation from the single seismic source to the targets, $\mathbf{D}(\omega)$ is a $K \times K$ diagonal matrix whose diagonal elements represents scattering coefficients, $\mathbf{G}(\omega)$ is a $P \times K$ matrix that represents the propagation from targets back to the receiver array, and $\mathbf{n}(\omega)$ the additive noise vector [6–8,56]. The elements of the propagation matrices are given by the 2-D Green's function. Since only the signal reflected from the target is of interest, the active system in (71) can be simplified to the following passive system

$$\mathbf{y}(\omega) = \mathbf{G}(\omega)\mathbf{s}(\omega) + \mathbf{n}(\omega), \tag{72}$$

where $\mathbf{D}(\omega)\mathbf{g}_1(\omega)$ has been replaced by a $K \times 1$ signal vector $\mathbf{s}(\omega)$ that represents the reflected signal from targets. Equation (72) has the same mathematical form as the narrow-band data model used in conventional array signal processing [34] and this similarity will be exploited while calculating the likelihood statistics for the seismic problem.

In the seismic problem, the elements of the propagation matrix $\mathbf{G}(\omega)$ are given by the illuminating Green's vector (steering vector) [6–8, 13],

$$\mathbf{g}(\mathbf{z}, \mathbf{x}, \omega) = \left[\tilde{g}(\mathbf{z}, \mathbf{x}_1, \omega), \tilde{g}(\mathbf{z}, \mathbf{x}_2, \omega), \ldots, \tilde{g}(\mathbf{z}, \mathbf{x}_P, \omega)\right]^T, \tag{73}$$

where $\mathbf{z}$ is the target position, $\mathbf{x}_i$ represents the i^{th} sensor position in the 2D plane, and the function $\tilde{g}$ is the 2D Green's function, whose analytical form is [12],

$$\tilde{g}(r, r', \omega) = \frac{i}{4} H_0^{(1)}\left(\frac{\omega}{v(\omega)}|r - r'|\right), \tag{74}$$

where $H_0^{(1)}$ is the zero-order Hankel function of the first kind, and $v(\omega)$ is the frequency-dependent Rayleigh wave velocity.

The method of spectrum analysis of surface waves which was introduced in Chapter 3, will be used to determine the velocity vs. frequency [9]. To minimize confusion when we refer to the existing array processing literature results, we change the notation for the propagation matrix $\mathbf{G}$ to $\mathbf{A}$ (known as the steering matrix in array signal processing problems). The

final form of the data model becomes [34],

$$\mathbf{y}(\omega) = \mathbf{A}(\zeta, \mathbf{z}, \omega)\mathbf{s}(\omega) + \mathbf{n}(\omega), \tag{75}$$

where $\mathbf{y}(\omega) \in \mathcal{C}^{P\times 1}$ is the noisy array output vector, $\mathbf{n}(\omega) \in \mathcal{C}^{P\times 1}$ is a complex additive noise, and $\mathbf{s}(\omega) \in \mathcal{C}^{K\times 1}$ is the signal vector. The array manifold $\mathbf{A}(\zeta, \mathbf{z}, \omega)$ has elements given by the Green's function (73), which depends on the array center position ζ and the (unknown) target position $\mathbf{z}$. Note that the individual receiver positions $\mathbf{x}_i$ can be related to ζ via the known array geometry. Consequently, our objective is to determine the target position $\mathbf{z}$ given the received array data $\mathbf{y}(\omega)$.

5.3 Target Location Estimation

5.3.1 Position Parameters Estimate

Let $\mathbf{Y}_t = \left[\ \mathbf{y}_t^T(\omega_1)\ ,\ \ldots\ ,\ \mathbf{y}_t^T(\omega_N)\ \right]^T$, $\mathbf{Y}_t \in \mathcal{C}^{PN\times 1}$, be the data vector, formed by aggregating the Fourier transform at frequencies ω_i of the received data $\mathbf{y}_t$ at each seismic sensor during the batch period t, where $\omega_i, i = 1, 2, \ldots, N$ are N frequencies used in processing. These frequencies could be obtained from spectrum analysis plots. Under the *i.i.d.* Gaussian noise assumption, the probability density function for the current received data is given by [17, 18, 72],

$$p(\mathbf{Y}_t) = \prod_{l=1}^{N} \frac{1}{\pi^P \sigma_t^{2P}} \exp\left\{-\frac{1}{\sigma_t^2}||\mathbf{y}_t(\omega_l) - \mathbf{A}_t(\omega_l)\mathbf{s}_t(\omega_l)||^2\right\} \tag{76}$$

Using (76), one can calculate the negative log-likelihood function of the data

$$L^- = NP\log(\pi\sigma_t^2) + \frac{1}{\sigma_t^2}\sum_{l=1}^{N}||\mathbf{y}_t(\omega_l) - \mathbf{A}_t(\omega_l)\mathbf{s}_t(\omega_l)||^2. \tag{77}$$

The ML estimate, maximizing the log-likelihood, can be determined by minimizing L^-. In (77), both the target signal and the noise variance are unknown. Therefore, we first estimate the noise variance by fixing the target position in $\mathbf{A}_t(\omega)$ and the source signal $\mathbf{s}_t(\omega)$. The ML estimate of the noise variance σ_t^2 is given by

$$\hat{\sigma}_t^2 = \frac{1}{NP}\sum_{l=1}^{N}||\mathbf{y}_t(\omega_l) - \mathbf{A}_t(\omega_l)\mathbf{s}_t(\omega_l)||^2. \tag{78}$$

When the estimated noise variance is used in conjunction with (77), the ML target signal estimate can be calculated

$$\hat{s}_t(\omega_l) = \left(\mathbf{A}_t^H(\omega_l)\mathbf{A}_t(\omega_l)\right)^{-1}\mathbf{A}_t^H\mathbf{y}_t(\omega_l). \tag{79}$$

Substituting (78) and (79) in (77), one can determine the ML cost function to minimize as a function of $\mathbf{z}$

$$J_t(\mathbf{z}) = \sum_{l=1}^{N}\left|\left|\left\{I - \mathbf{A}_t(\omega_l)\left(\mathbf{A}_t^H(\omega_l)\mathbf{A}_t(\omega_l)\right)^{-1}\mathbf{A}_t^H(\omega_l)\right\}\mathbf{y}_t(\omega_l)\right|\right|^2 = \sum_{l=1}^{N}\text{trace}\left\{P_A^{\perp}(\omega_l)R_y(\omega_l)\right\}, \tag{80}$$

where $P_{A_t}^{\perp}(\omega_l) = I - \mathbf{A}_t(\omega_l)\left(\mathbf{A}_t^H(\omega_l)\mathbf{A}_t(\omega_l)\right)^{-1}\mathbf{A}_t^H(\omega_l)$, is the projection onto the null space of $\mathbf{A}_t^H(\omega_l)$ and $R_y(\omega_l) = \mathbf{y}_t(\omega_l)\mathbf{y}_t^H(\omega_l)$ is the single snapshot covariance matrix estimate at the frequency ω_l. The target location estimate is then given by the minimum of the cost function (80)

$$\mathbf{z} = \arg\min_{\mathbf{z}} J_t(\mathbf{z}), \tag{81}$$

where the array location is assumed known.

5.3.2 Cramér-Rao Lower Bound for the Estimate of z

The Cramér-Rao lower bound (CRLB) is an information theoretic inequality, which provides a lower bound for the variances of unbiased estimators. If an estimator achieves the CRLB, then it is also a solution of the likelihood equation [40,53,69]. The Cramér-Rao lower bound is the inverse of the Fisher information matrix (FIM). Assuming that the variance of the additive noise in (71) is known, the log-likelihood function for a single target can be written as

$$L(\zeta_t, \mathbf{z}) \doteq -\frac{1}{\sigma_t^2}\sum_{l=1}^{N}||\mathbf{y}_t(\omega_l) - \mathbf{a}_t(\zeta_t, \mathbf{z}, \omega_l)s_t(\omega_l)||^2, \tag{82}$$

where $\mathbf{a}_t(\zeta_t, \mathbf{z}, \omega)$ is the propagation (steering) vector from the array center to the target position. The $(i,j)^{\text{th}}$ element of the FIM is given by the partial derivative of (82) with respect to the i^{th} and j^{th} parameters of the vector $\mathbf{z}$ [17],

$$\mathbf{F}_{i,j}(\mathbf{z}, \zeta_t) = E_y\left\{\frac{\partial^2 L(\mathbf{z}, \zeta_t)}{\partial z_i \partial z_j}\right\} = -\frac{2}{\sigma_t^2}\sum_{l=1}^{N}\Re\left\{\left(\frac{\partial \mathbf{a}_t(\mathbf{z}, \zeta_t, \omega_l)}{\partial z_i}\right)^H\frac{\partial \mathbf{a}_t(\mathbf{z}, \zeta_t, \omega_l)}{\partial z_j}\right\}, \tag{83}$$

where $E_y\{.\}$ denotes the expected value, and $\mathbf{F}$ is the Fisher information matrix (FIM) as a function of the target position $\mathbf{z}$ and the array center ζ. The elements of steering vector are given in terms of 2-D Green's function in (74). The partial derivative of the steering vector is calculated with respect to the target coordinates for a fixed array center.

5.4 Movement of the Seismic Array via Optimal Experiments

In the previous sections, we described how to determine the target position and its FIM that represents the uncertainty about the estimates as a function of the array center position. Note that the sensors in the 2D array has known locations with respect to the array center ζ. Suppose that we have estimated the target location at batch t, and now we are interested in determining the next optimal array center position candidate for the batch $t+1$. Our approach in selecting the new sensor position reduces the expected uncertainty in the estimated target coordinates by minimizing the determinant of the CRLB. Hence, to minimize the CRLB determinant, we must maximize the determinant of the FIM as a function of the array center. In the optimal experiment literature this technique is called D-optimal design [23]. A similar approach is used in [45] for magnetic sensors. Other approaches might minimize the trace of the CRLB or minimize the maximum eigenvalue of the CRLB.

Let q represent the determinant of the FIM. The cumulative effect of the measurements up to batch t can be written as:

$$q\left(\{\zeta_1,\ldots,\zeta_t\}\right) = |F(\zeta_1,\ldots,\zeta_t)| = \left|\sum_{j=1}^{t} F(\zeta_j)\right|, \tag{84}$$

where $|.|$ stands for determinant and F_t represents the Fisher information matrix at batch t. The logarithmic increase due to the additional measurements at batch $t+1$ is given by

$$\begin{aligned}\delta_q(\boldsymbol{\zeta}_{t+1}) &= \ln q\left(\{\zeta_1,\ldots,\zeta_{t+1}\}\right) - \ln q\left(\{\zeta_1,\ldots,\zeta_t\}\right) \\ &= \ln\left|I + F(\zeta_{t+1})B_t^{-1}\right|,\end{aligned} \tag{85}$$

where I is an identity matrix, and $B_t = \sum_{j=1}^{t} F(\zeta_j)$. To achieve the maximum expected

information gain, the next optimal array center can be determined by

$$\zeta_{t+1} = \arg\max_{\zeta} \ln \left| I + F(\zeta_{t+1}) B_t^{-1} \right|. \tag{86}$$

In this optimization problem, there are implicit constraints that come from the configuration of the seismic system. First of all, the target reflections do not behave as an omni-directional active source. Hence, we need to make sure that the receiving array is between the source and the targets all the time to receive the reflected waves. One way to impose this condition is to use a movement step size of radius r from the previous array center position. Hence, the maximum of (86) is calculated on a circle of radius r, where the center of the circle is at the previous optimum array center position.

Another way to impose a constraint on the movement would be to add a penalty term as in [45]:

$$\Psi(\zeta) = \delta_q(\boldsymbol{\zeta}_{t+1}) - \nu \sqrt{(\zeta_{t+1} - \zeta_t)^T \Sigma^{-1} (\zeta_{t+1} - \zeta_t)}, \tag{87}$$

where $\nu \geq 0$ is the penalty factor that must be chosen relative to the size of $\delta_q(\boldsymbol{\zeta}_{t+1})$, and Σ is a diagonal matrix, whose diagonal elements are chosen to ensure the smooth movement of the array from its previous position. The step size is chosen heuristically. Because the array might choose a different step size at each batch, depending on the choice of ν, this approach is more complicated.

5.5 Processing of Experimental Data

An experiment has been conducted in a laboratory setting, where buried mines in a sandbox are used as targets [63]. A shaker is used as a seismic source, and the input signal is a differentiated Gaussian pulse centered at 450Hz. The pulse in the time and frequency domains is shown in Figs. 40(a) and (b), respectively. In the experiment, ground contacting accelerometers are used as the seismic sensors. The target is a TS-50 (anti-personnel) landmine buried at a depth of 1 cm. We estimate the wavenumber for the reflected signals at different frequencies by using the algorithm presented in Chapter 3 [9]. To separate the waves, a linear array of fifteen sensors is used, but only three of them are used in the subsequent imaging step. The raw collected data at four time instants is shown in Fig. 41.

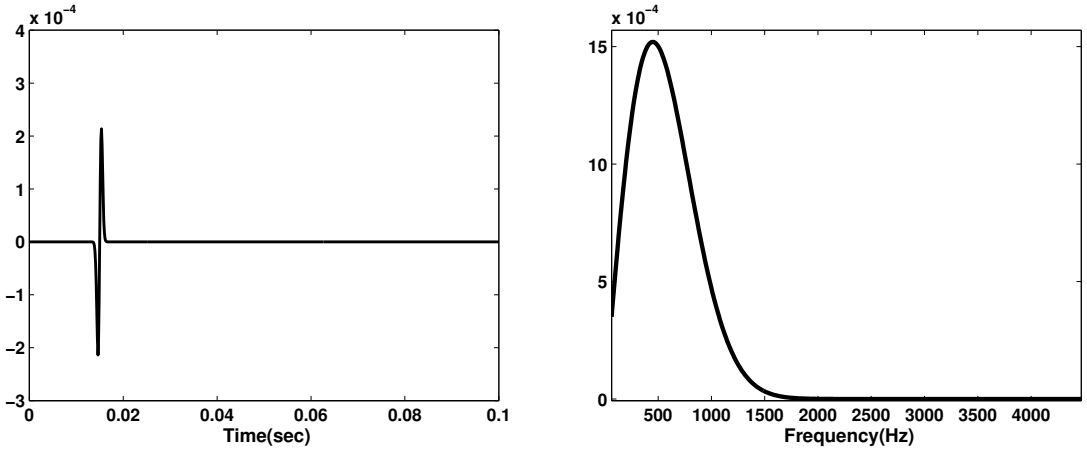

(a) (b)

Figure 40: Probing signal is a differentiated Gaussian pulse. (a) Signal amplitude vs. time. (b) Magnitude of the frequency response vs. frequency.

This figure shows the seismic wave approaching toward the mine during the first three frames; in the last frame the reflection from the mine can be seen clearly. Once the data is collected and the waves are separated the next step is to estimate the target position. The initial estimate is shown as a surface plot in Fig. 42. The surface plot is obtained by using (80) and this cost function is calculated at each point in the 2D grid. The minimum of this function is the target position estimate. However, the inverse of this function is plotted in Fig. 42. Based on the initial estimate, the next optimal array position is determined by using (86). This function is calculated at each grid point as a function of array center position using the estimated target position from the previous step. The surface plots for both the circle and the measurement constraints are shown in Figs. 43(a) and (b). For the circle constraint, a radius of 25 cm is used. For the measurement constraint (87), a relative weighting $\nu = 1.1$ is used, and for the movement penalty matrix Σ, a diagonal matrix with diagonal values of 20^2 is used. The circle constraint plot shown in Fig. 43(a) indicates the present array center position (center of the circle), and the next array position is indicated by the arrow. This position is the peak of the measure calculated on the circle, as shown in Fig. 47(a). The measurement constraint surface plot, shown in Fig. 43(b), indicates two possible directions to move, as given by two arrows.

Once the next optimum array position is determined and the array is moved to a new

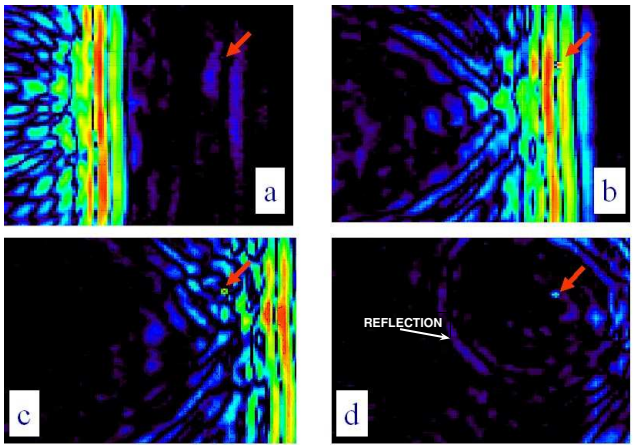

Figure 41: Surface displacement plots showing wave propagation. Location of the mine is shown by an arrow (40dB scale). (a) Rayleigh wave approaching toward the mine, (b) wave reached on top of mine and it starts to resonate, (c) main pulse have passed the mine, (d) reflection from the mine can be seen clearly.

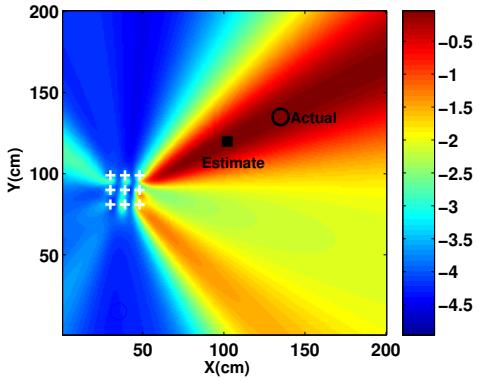

Figure 42: Initial target location estimate is done using the ML cost function (80) (dB scale).

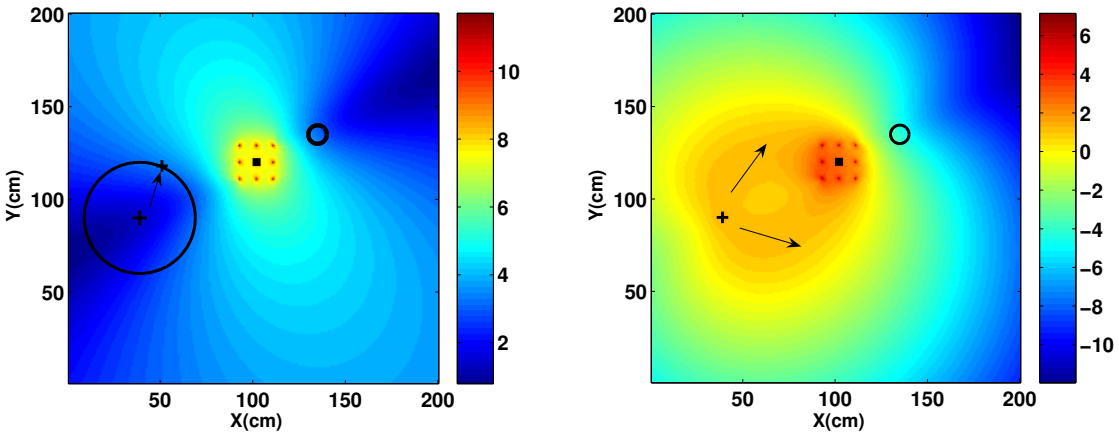

Figure 43: The optimum movement for the next array position can be constrained by (a) A maximum distance within a circle; or by (b) A penalty function. The plotted surface is the determinant of the FIM on a linear scale and (b) is the FIM determinant plus the penalty term. Two possible directions to move are shown by the arrows.

position, a new batch of data is collected. We then append the existing data to the new set of data. The new target position estimate and the next optimum movement are determined by using the cumulative data. Further steps are shown in Fig. 44. With each successive step the target position estimate is improved, along with a decrease in the uncertainty ellipse because the cumulative estimation is effectively increasing the aperture.

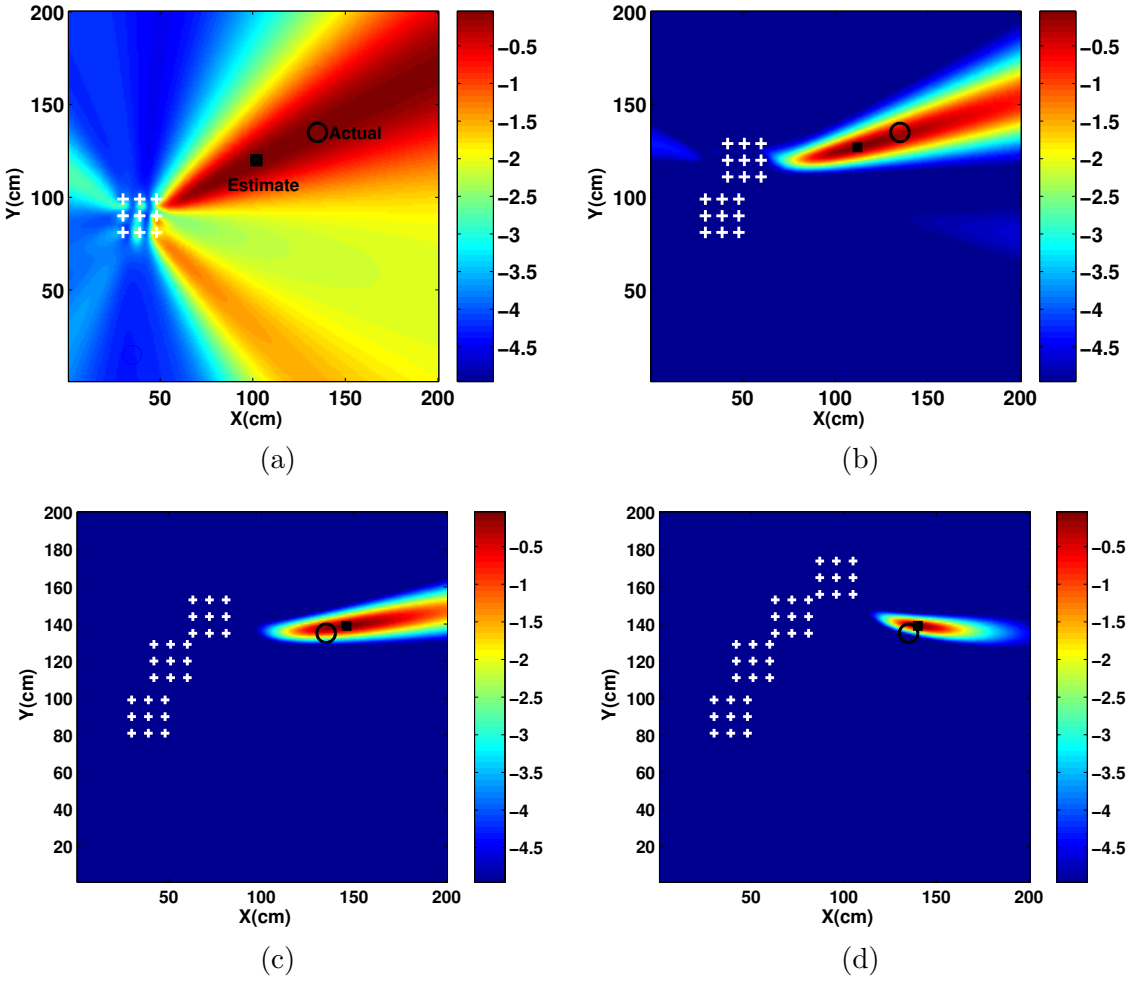

Figure 44: Target position estimates (dB scale) (a) Initial estimate. (b) Estimate after the optimal move as determined by the circle constraint. (c) After two optimal moves. (d) After three optimal moves.

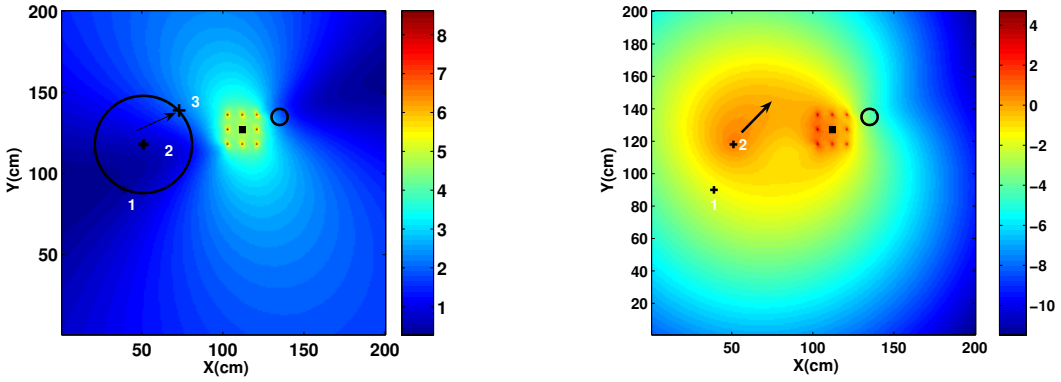

Figure 45: The optimum movement for the next array position at step 2, constrained by (a) A maximum distance within a circle; or by (b) A penalty function. The plotted surface is the determinant of the FIM on a linear scale and (b) is the FIM determinant plus the penalty term. Possible direction to move are shown by the arrow.

The surface plots for the next array position at each successive step are also shown in Figs. 45 and 46. The values calculated along a circle at the first three steps are also shown in Fig. 47. The peak of each plot is used as the next array center position. At the first step, there are two possible directions to move, with one being slightly better. However, as the array move around, and more information is collected about the target, one direction becomes more favorable as compared to the others. This same behavior is also seen when using the measurement constraint surface plots shown in Figs. 43(b), 45(b) and 46(b) respectively.

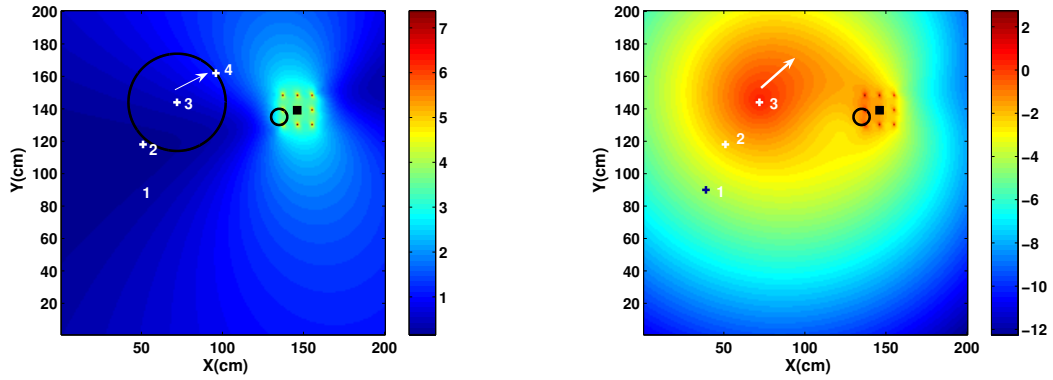

Figure 46: The optimum movement for the next array position at step 3, constrained by, (a) a maximum distance within a circle; or by (b) A penalty function. The plotted surface is the determinant of the FIM on a linear scale and (b) is the FIM determinant plus the penalty term. Possible direction to move are shown by the arrow.

Another important observation is that the array movement determined by the theory of optimal experiments is toward the target. Consequently, the reflected waves from the target also become stronger. The velocity spectrum plots shown in Fig. 48 for all these four positions show that as we move near the target, the reflected mode in the spectrum plots becomes more stronger and well defined. This is another indication that we are moving near the target.

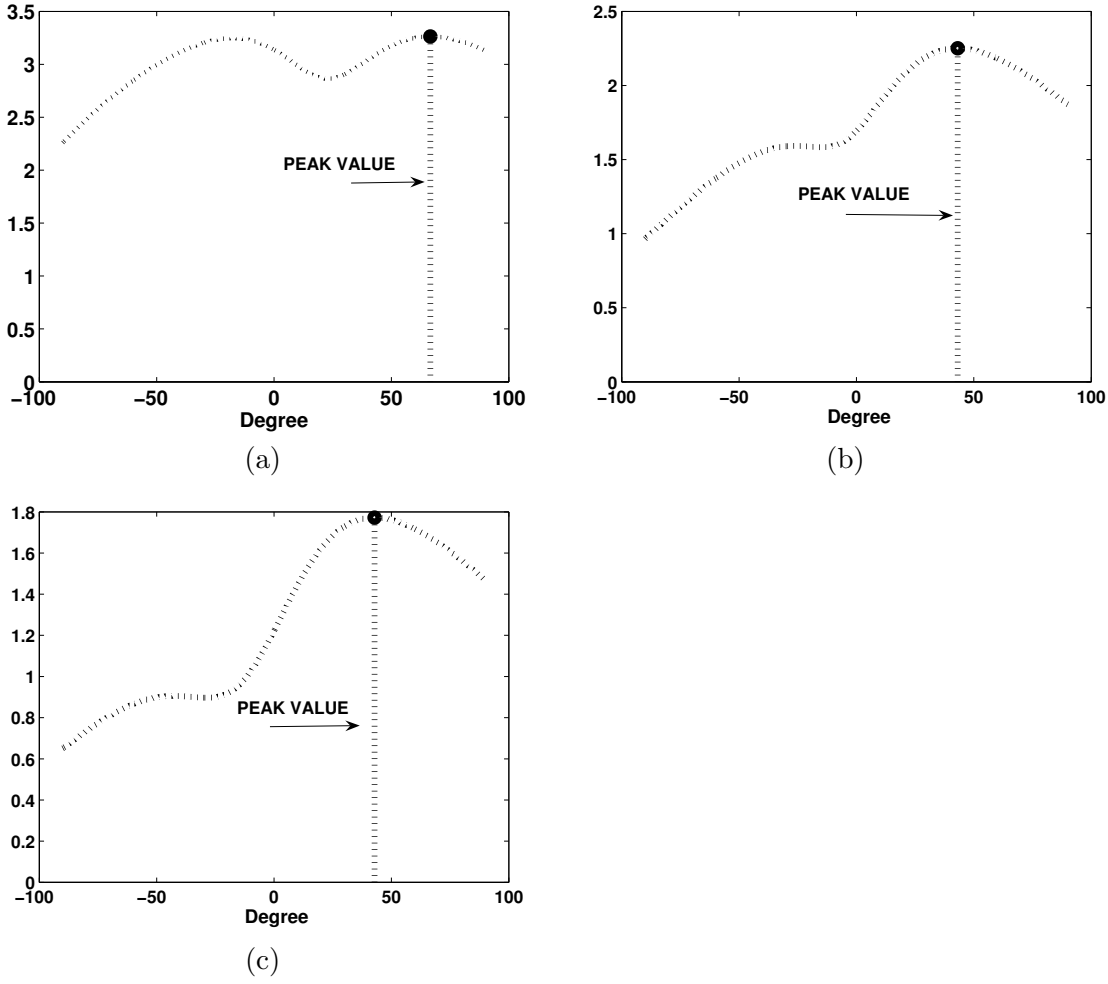

Figure 47: FIM determinant values calculated along a circle (circle constraint) (a) Step 1 (b) Step 2 (c) Step 3

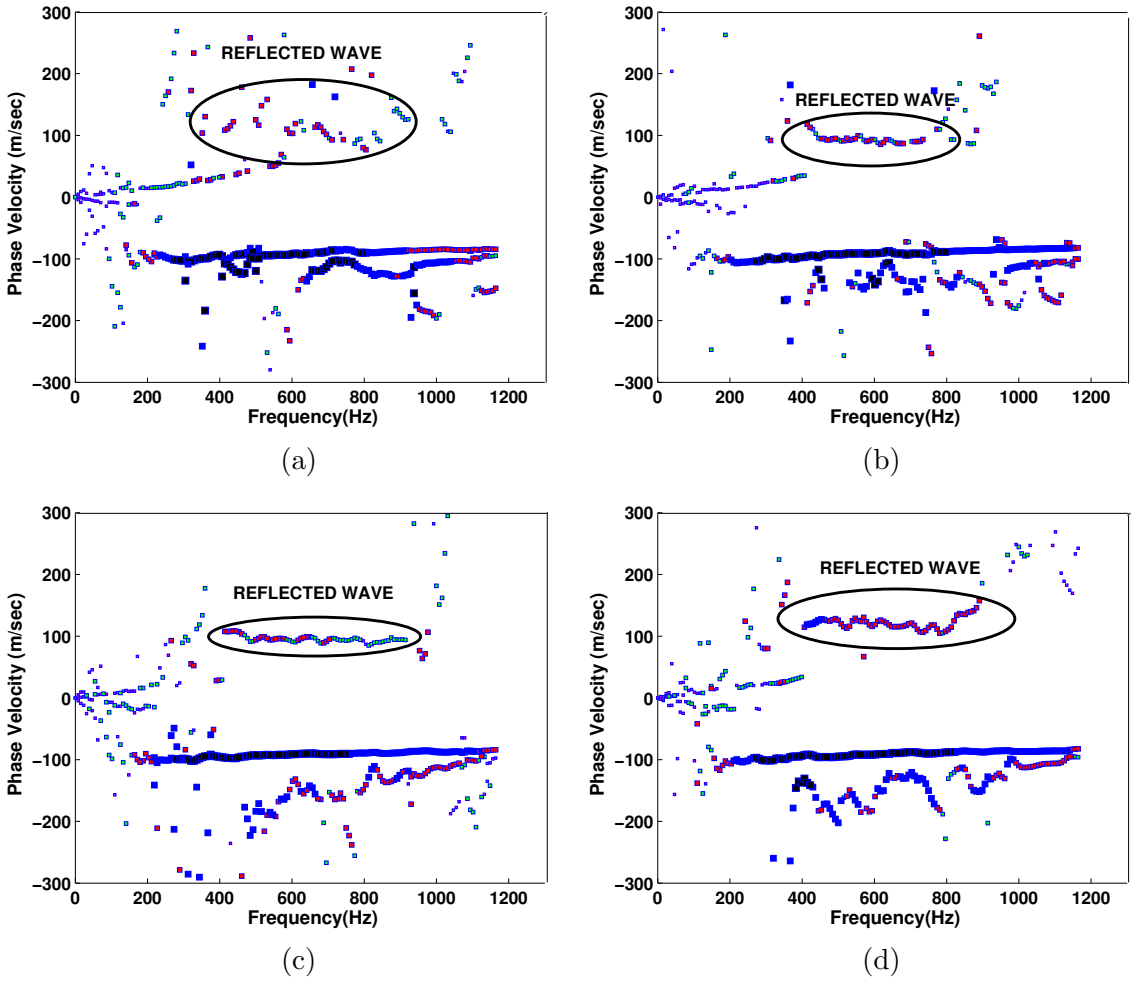

Figure 48: Spectrum analysis result in a well defined reflected wavefront as the array gets near the target after the optimal moves. (a) Initial spectrum analysis. (b) Spectrum analysis after the first optimal move. (c) Spectrum analysis after the second optimal move. (d) Spectrum analysis after the third optimal move.

5.6 Conclusions

The algorithm presented in this chapter shows that it is possible to control a maneuvering array to find buried targets. The data model was presented, along with an algorithm for estimating target position. The performance bound of the location estimate was used to derive an algorithm for optimal maneuvering. Two strategies were formulated to constrain the maneuvers for practical reasons. Both algorithms were verified by using experimental data, containing a single TS-50 AP landmine. The algorithm usually localizes the targets in only few steps, with considerable reduction in time and measurements. As an example, the existing imaging algorithm would have used the data collected over a complete grid of (61×61), with a total of 3721 measurements to locate the same target. Our algorithm uses a total of 180 measurements.

CHAPTER VI

OPTIMAL MANEUVERING: IMPLEMENTATION, ISSUES AND RESULTS

6.1 Introduction

In the previous chapter, an algorithm for optimal maneuvering was presented and its performance verified by processing experimental data containing a single TS-50 AP mine. However, to produce a robust system that can handle realistic situations many questions have to be answered. The motivation for this chapter is to present a set of experiments that imitate a variety of situations. It is impossible to simulate all possible situations, which a working seismic landmine detection system will encounter. However, the set of experiments presented in this chapter will cover most of the important aspects of the problem. In order to test the algorithm a working system was implemented, as described in Section 6.2. Next we present a set of issues that we hope to answer with the experiments.

Issue:1, How to make the algorithm robust for real life situations? A working system has to decide where to start, when to stop and how to make a final decision. To solve this a multi-mode imaging algorithm is proposed in Section 6.3 consisting of three modes. All the experiments presented in this chapter use these three modes to locate and confirm the targets.

Issue:2, Single target (landmine) of different sizes and shapes. This is the most common scenario. There are two main categories of landmines, smaller anti-personnel (AP) mines, and much larger anti-tank (AT) mines. These mines have different internal structures and are buried at different depths. A set of experiments is done using a single TS-50 AP mine, and also with a single VS-1.6 AT mine. The purpose of these experiments were to investigate how the algorithm behaves for single target of different sizes and shapes. The results of these experiments will be presented in

Section 6.4.

Issue:3, Effect of the radius r for the circle constraint. The example in Section 5.5 of the previous chapter and most examples in this chapter use a fixed radius of either 20 or 25 cm for the circle constraint. To see the effects of different values of r on localization, the experimental data was processed with values of the radius r from 20 cm to 30 cm. A criteria for selecting a radius is also proposed which is a function of distance between the current array position and the target position estimate. The results of these experiments will be presented in Section 6.5.

Issue:4, Multi-target case. When there are multiple targets present like the targets can be multiple mines, or mine in the presence of clutter such as rocks. It is envisioned that all realistic problems will be eventually treated as multi-target cases. Thus, we have to come up with an algorithm that can handle multi-target situations. An algorithm is presented in Section 6.6 to handle one target at a time, along with the results of experiments for two mines and several rocks.

Issue:5, Performance in the presence of clutter (rocks). In order to test the performance of the system in the presence of common types of clutter like rocks, several rocks of different sizes and shapes are introduced in the scan region along with the mines. The results of these experiments will be presented in Section 6.7. Some extreme cases are also presented, in which system is not able to locate the mine.

Issue:6, Drunken wave case. The purpose of these experiments is to test how the algorithm behaves when there is a large scale change in the propagation properties of the medium. This change causes the seismic wave to bend and change its path. The results of these experiments will be presented in Section 6.8.

6.2 Real-time Experimental Setup

The processing example in Section 5.5 is one in which the array is formed synthetically, because the actual data is collected with a single sensor only. This data is then grouped along a line to form the linear array necessary for processing. More recently an actual

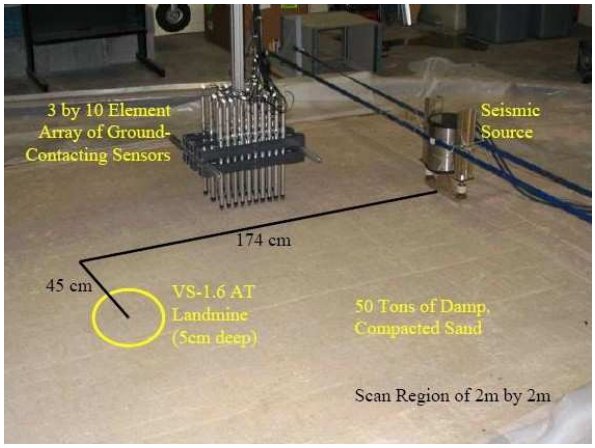

Figure 49: Experimental Setup showing the sensor array of 3 by 10 elements, a fixed seismic source, and the location of the buried target.

array system has been built for use in our laboratory setting. This source and receiver array setup for the real time experiment is shown in Fig. 49. The fixed seismic source and the mobile sensor array consisting of 30 elements are also shown. The movement of the array and the firing of the source is controlled by a Labview interface. The probing pulse is a differentiated Gaussian pulse at a center frequency of 450 Hz. The 2-D rectangular seismic array consists of three lines each containing ten uniformly spaced sensors. The data collected across each line of the seismic array is processed by the technique presented in Chapter 3, and the forward and reverse waves are separated. Three out of the ten sensors in each line are retained to form a 2-D array for imaging. Hence, there are a total of nine sensors arranged in a 3×3 2-D grid.

6.3 Multi-Mode Imaging

The algorithm and a specific processing example for the optimal maneuvering of a seismic sensor was presented in Chapter 5. This algorithm needs an initialization phase to determine where to start the search and where to place the array at the first step. It also needs an ending phase where the final decision would be made. This "end-game" decision involves accurately identifying the locations of the targets to within a prescribed tolerance. The strategy is divided into three steps explained as follows:

6.3.1 Probe Mode

The only clue where to place the array initially is the position of the source, over which we have control. There might be prior knowledge from other sensors about where the target is, but we will not assume such knowledge is available. In this mode two or three fixed array positions very near to the source are used to collect the data initially. Then the imaging algorithm is used to estimate target position. Once we have this estimate of target position we can place the array at its starting position for optimal maneuvering.

6.3.2 Search Mode

The optimal maneuvering presented in Chapter 5 is what we define to be the search mode. After having decided where to place the array during the probe mode, we let the algorithm run. The algorithm performs its steps and moves closer to where the target is located. It also reduces its uncertainty considerably, as compared to the location estimate we obtained during the probe mode.

6.3.3 Detection Mode

Once the search mode gives us the clue where the target might be, the final step is to find the exact location of the target and detect whether or not it is a landmine. The best way to detect the target is to use the resonance/reflection property of the landmines [61, 62]. In order to do this, it is necessary to be right on top of the target. Most of the resonance energy is present in the reflected part of the wave. The spectrum analysis algorithm presented in Chapter 3 will be used for the purpose of separating the resonance/reflection part of the wave. The imaging algorithm and detector framework will be presented in Chapter 7.

6.4 Single Target Case

This is the most common scenario and two experiments will be presented. In the first case, an anti-tank (AT) mine, VS1.6, is buried at a depth of 5 cm. The AT mine is large with a diameter of roughly 20 cm. The first two iterations are the probe phase, and the next three array positions are chosen optimally. All the location estimate results are shown together in Fig. 50, with the final estimate in Fig. 50(d). We observe the same behavior as

before with the array moving toward the target while increasing the effective aperture, and thereby reducing the size of the uncertainty ellipse around the target position estimate. Each iteration takes approximately 40 seconds, including all the data acquisition and processing (150 measurements). So in less than 3 or 4 minutes we are able to find the exact position of the target. This should be compared to the existing method, which finds a target in an area of (2×2) m using measurements on a grid of size (61x61) [11, 62]. The complete scan takes a couple of hours to isolate a resonating target. A radius of 25 cm is used for the circle constraint in this case.

In the second example a TS50 anti-personnel (AP) mine is buried at a depth of 1 cm. The mine is localized with reduced uncertainty in three optimal moves as shown in Fig. 51. The first two are probe phase positions as shown in Fig. 51(a). A radius of 20 cm is used for the circle constraint here.

Both of these examples demonstrate that the algorithm is able to locate a single target of different sizes, shapes and burial depths successfully.

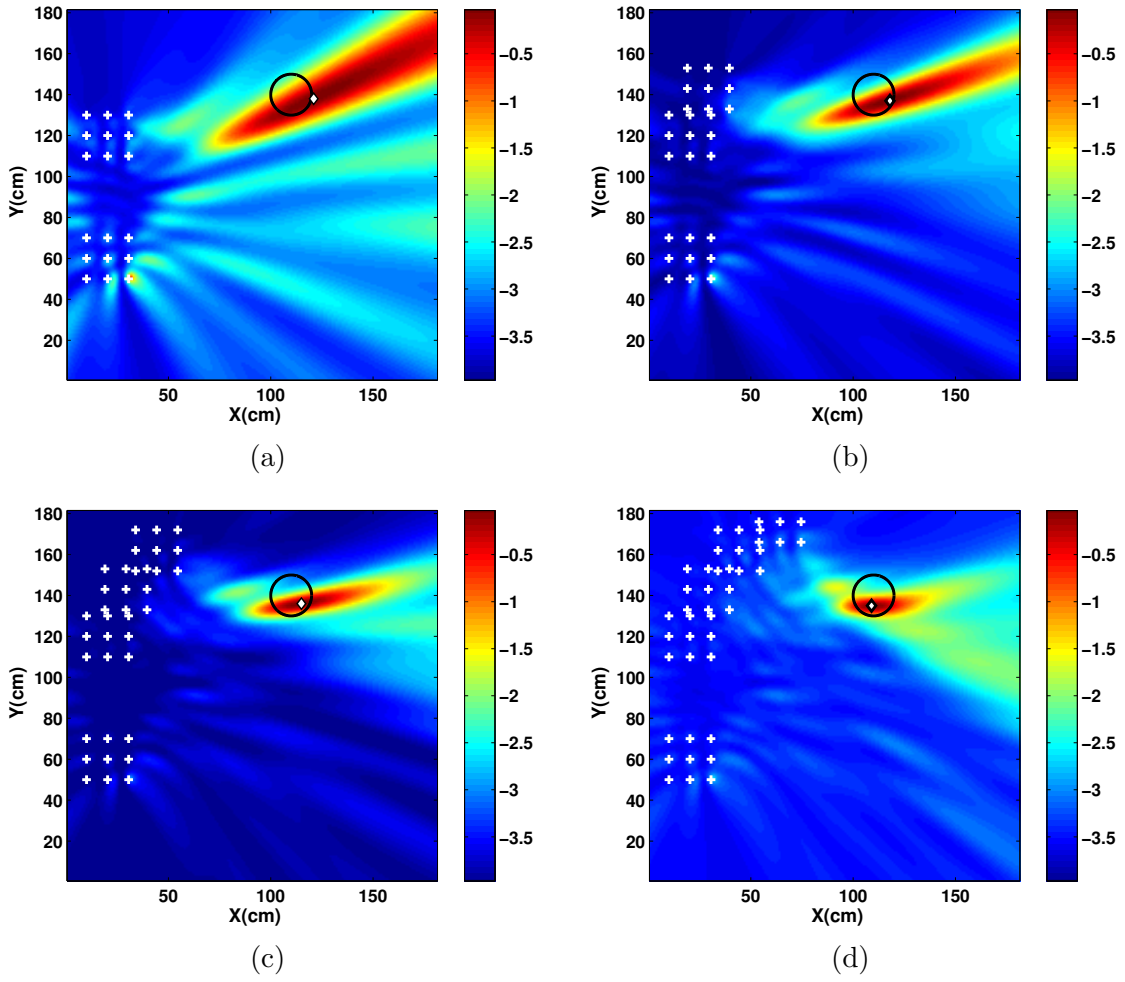

Figure 50: VS1.6 mine at 5 cm depth. Maximum likelihood surfaces at various probing steps (dB scale) (a) After the probe phase. Two fixed array positions with respect to the source are used. (b) After the first optimal move. (c) After the second optimal move. (d) The final target position estimate is shown. The resolution of the image around the true target position is significantly increased after the optimal array movements. The circle indicates the size and position of the mine and the white diamond shows the location estimate.

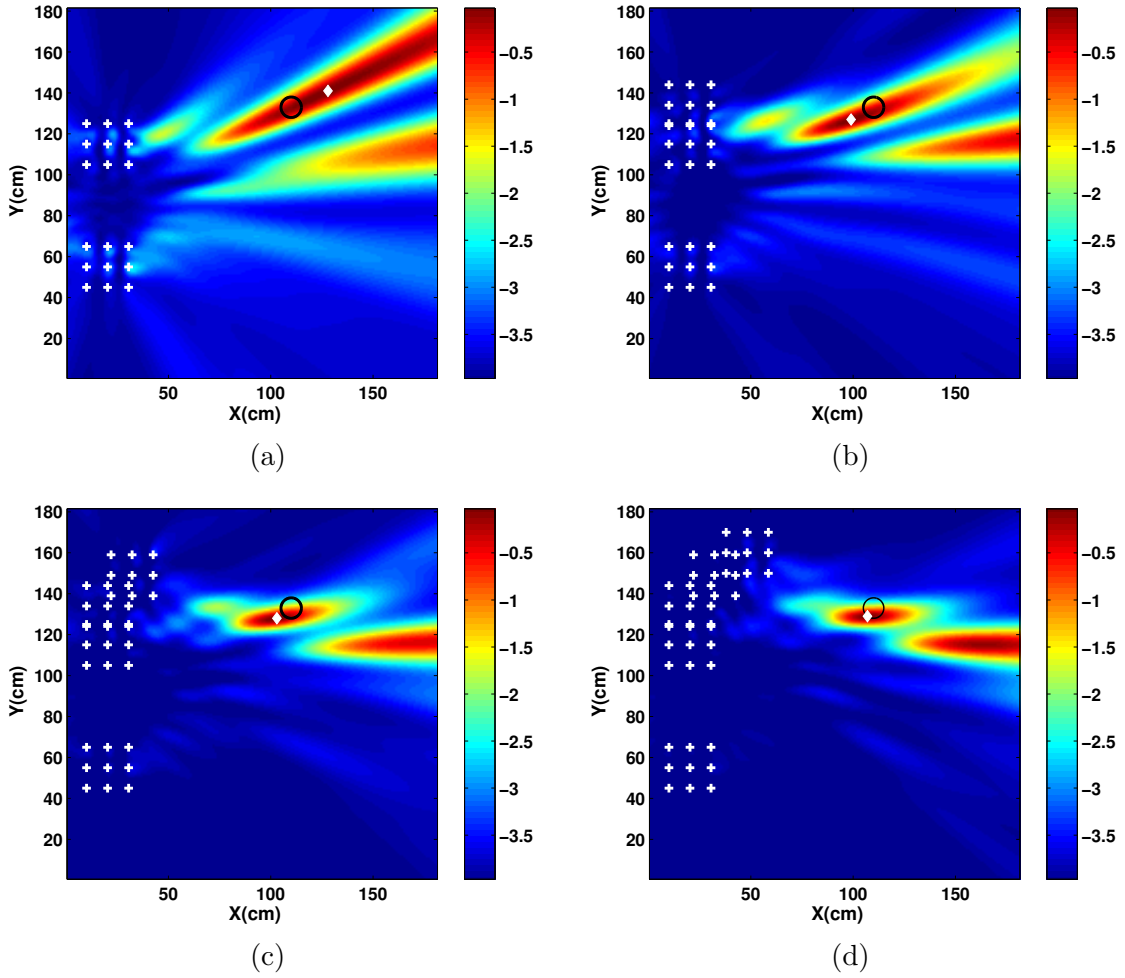

Figure 51: TS50 mine buried at a depth of 1 cm. Maximum likelihood surfaces at various probing steps (dB scale). (a) After the probe phase. Two fixed array positions with respect to the source are used. Smaller black circle shows the size of the AP mine, and the white diamond shows the location estimate. (b) After the first optimal move. (c) After the second optimal move. (d) The final target position estimate is shown.

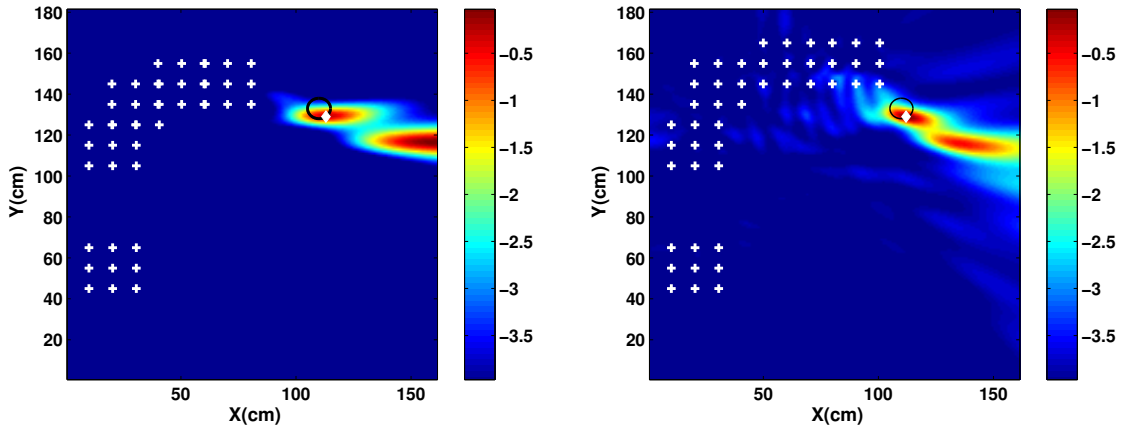

Figure 52: Maneuvering using different values (fixed) of r for the circle constraint. A single TS-50 AP mine at a depth of 1 cm is used. (a) Using $r = 25$ cm, and after three optimal moves. (b) Using $r = 30$ cm, and after three optimal moves.

6.5 Effect of Choice of Radius r for Circle Constraint

The circle constraint for next array position requires a value of radius r. In order to see the possible effects of different values of r on localization, a set of experiments are conducted using the TS50 mine buried at a depth of 1 cm. Three different values of r are used: 20, 25 and 30 cm. The final results after three optimal moves are given in Fig. 51(d) for 20 cm, and in Figs. 52(a) and (b) for 25 and 30 cm, respectively. Comparing all three, it appears that the final uncertainty ellipse size is more or less the same for all three cases. Hence, the value of r doesn't affect the algorithm very much.

If we drop the strategy of using a fixed value of r for all iterations, we can make it adaptive by choosing the radius r as a function of the distance d between the current array position and the target position estimate. Two experiments are conducted with the adaptive radius equal to one half and one third of the distance d. This will also guarantee that the array will always lie between the source and the target. Final results of these experiments are shown in Fig. 53. Again the results look more or less same for two cases.

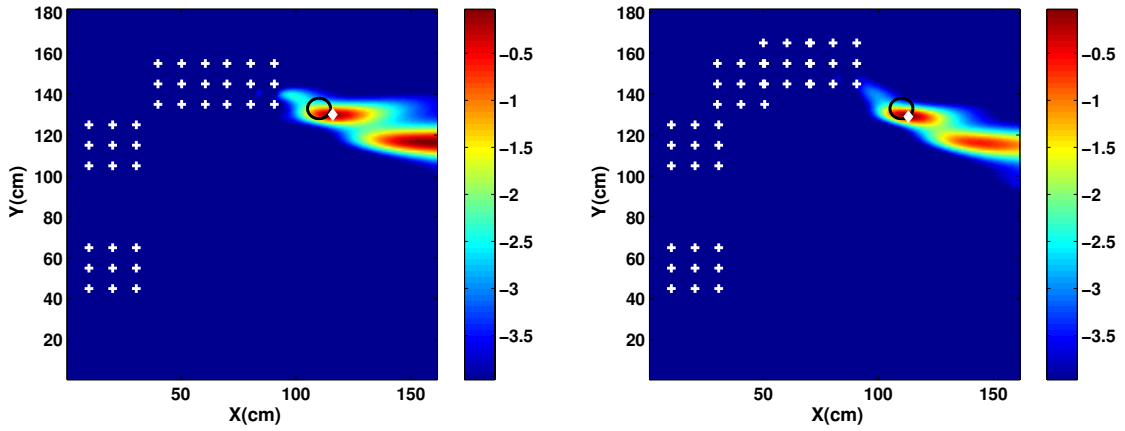

Figure 53: Maneuvering using adaptive values of r for the circle constraint. A single TS-50 AP mine at a depth of 1 cm is used. The r in this case is a function of distance d between the current array position and the estimated target position. (a) Using $r = \frac{d}{2}$, and after two optimal moves. (b) Using $r = \frac{d}{3}$, and after three optimal moves.

6.6 Multi-target Case

The set of experiments in this section are used to illustrate the cases when there are multiple targets to localize. Based on these experimenters, a general strategy will be proposed which can be used for multi-target cases.

6.6.1 Experiment:1

In this experiment we assume that we know the number of targets. Two VS1.6 (AT) mines are buried at the same depth of 5 cm. The goal is to localize both of them with optimal maneuvering. During the probe stage, three fixed array positions with respect to the source are used to find the starting locations for the targets. These array positions are shown in Fig. 54(a), but only the array center positions are shown; the shape and size of the array is same as in Section 6.4. After the initial location estimates have been obtained, then we can start to maneuver the array optimally with the FIM. Since we have two targets in this case, the Fisher information matrix is of size 4×4. The matrix can be partitioned into four 2×2 quadrants related to individual targets and their cross terms.

Since we have to use the Fisher information matrix in (86), there are various options available. One is to use the full 4×4 FIM matrix in (86), and the other is to use a

partitioned approach with two smaller 2×2 FIMs, one for each target. The second case involves multi-objective optimization to satisfy both measures. Using the 4×4 approach the next array position is determined by using (86) with a circle constraint. A circle of radius 25 cm is used, and the array at position-2 is used as the reference with respect to which the next optimal array position is determined. The surface obtained by using the 4×4 FIM is shown in Fig. 54(b) and the values on the circle from -90^o to 90^o are shown in Fig. 54(c). Clearly there are two well defined peaks with one direction favored more than the other. The peak of this plot is picked to generate the next optimal array position. The next array positions are obtained optimally and the surface plot at step 4 and at the last step are shown in Fig. 55. There are two interesting observations, the optimal maneuvers pick one target and move toward it, as the array moves toward target-A, the signature of target-B becomes weaker. At the last step target-A has been localized completely with appreciable reduction in the size of the uncertainty ellipse. Notice that the weak signature of target-B is still somewhat present, and with a very accurate position estimate. However, once we have completely localized one target, we would return to the original starting positions and remove the effects of the already localized target from the array data. The remaining target(s) can then be localized. The technique used will be the one presented in Section 4.3 [7, 70]. It is based on the CLEAN algorithm originally developed for radio astronomy [29]. Suppose that there are M targets, and out of these we have estimated all the positions except the m^{th} target. Then the new array data at a frequency ω_l which can be used for this target is given by:

$$\mathbf{y}_m(\omega_l) = \mathbf{y}(\omega_l) - \sum_{j=1, j \neq m}^{M} \mathbf{g}(\mathbf{p}_j, \omega_l) s_j(\omega_l) \tag{88}$$

where $\mathbf{g}$ is the steering vector whose elements are given by a 2D Green's function, $\mathbf{p}_j$ is the j^{th} target position estimate, and $s_j(\omega_l)$ is the signal reflected from the j^{th} target and its value is calculated using (79). Once we remove the first target using (88), the FIM will be reduced in size . The probe phase for the second target uses the previous starting position as shown in Fig. 56(a). The only difference is that the effect of target-A has already been completely removed from the array data. The new array data is then used to determine the target

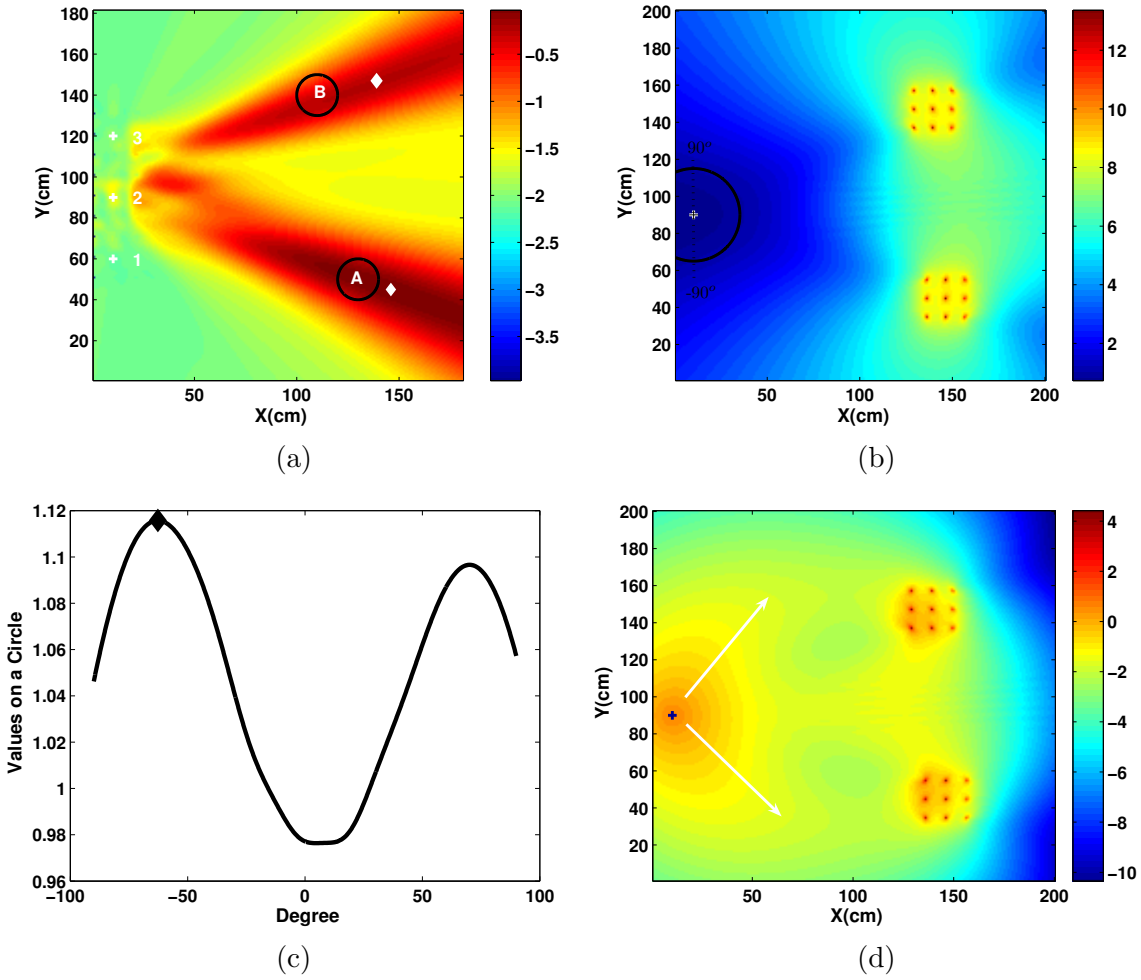

Figure 54: (a) Probe Phase: Initial target location estimate is done using the ML cost function (80) (dB scale). Three fixed array positions centered at 1, 2 and 3 are used. Only center position of array is shown. The position of two targets (circle) and their initial estimates are also shown (diamond). (b) Next optimal array position (linear scale). Surface plot obtained by (86) with a circle of radius of 25 cm (c) Next optimal array position (linear scale). Value obtained on the circle from -90^o to 90^o (d) Next optimal array position (linear scale). Surface plot obtained by (87), using a measurement constraint.

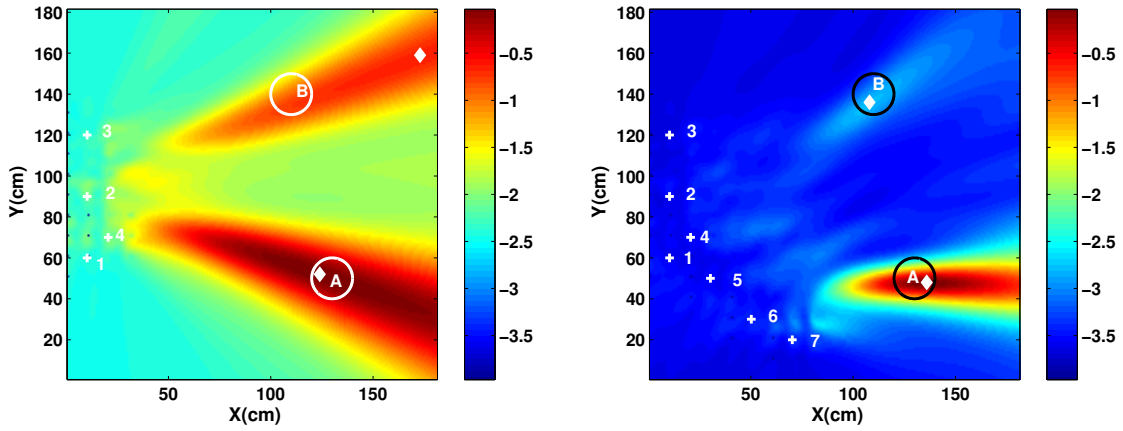

Figure 55: Other optimal maneuvers for the target position estimation are shown (dB scale) (a) Step 4. (b) Step 7 (last step).

position. The next few optimal moves to locate target-B are shown in Fig. 56(b). Clearly this second target has been completely localized in addition to considerable reduction in the size of its uncertainty ellipse.

6.6.2 Experiment:2

In most realistic situations, there is no knowledge of the number of targets. In these situations, a different strategy can be used. At each iteration, it is assumed that there is only one strong target. We locate this target using optimal moves. Once it is localized, we remove the contribution of this target from the array by using the CLEAN algorithm, and proceed to find the next strongest target. We repeat this kind of operation until all the possible targets are localized. An important question to answer in this type of situation is how to be sure that there is nothing left to be located. To answer this question, a power distribution is calculated using the array data at the probe phase only. The power distribution is calculated by [70]:

$$PD(\mathbf{p},\omega) = \sum_{l=1}^{N} \frac{|\mathbf{g}^H(\mathbf{p},\omega_l)\mathbf{y}(\omega_l)|^2}{||\mathbf{g}(\mathbf{p},\omega_l)||^2} \tag{89}$$

This distribution is calculated over the area of interest as a function of position $\mathbf{p}$, $\mathbf{g}(\mathbf{p},\omega_l)$ is the Green's function vector (steering vector) and $\mathbf{y}(\omega_l)$ is the array data at a frequency ω_l. For stopping criteria, a metric is calculated based on matrix norms. The norm of a

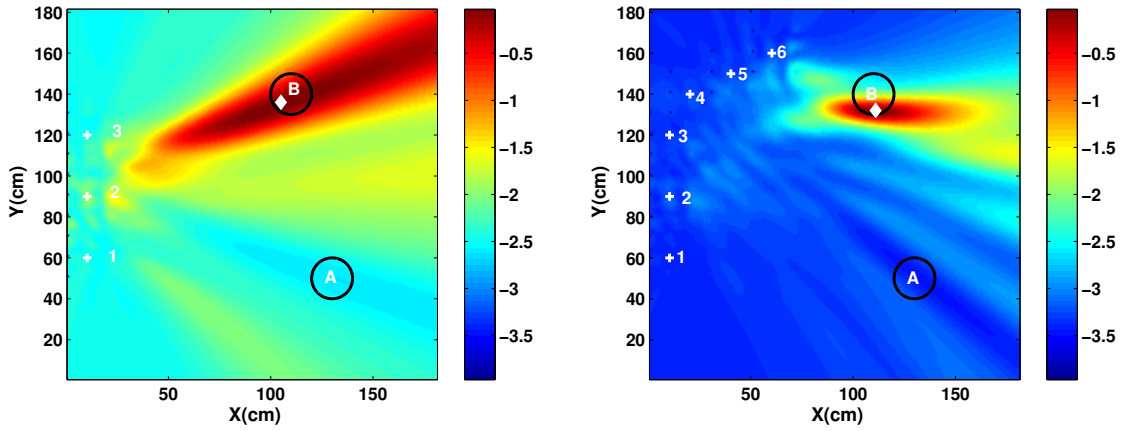

(a) (b)

Figure 56: Target-B position estimates after removing the effect of target-A from the array (dB scale) (a) Probe Phase which uses the array position centered at 1, 2 and 3. (b) Final estimate after three optimal maneuvers.

matrix is a scalar that gives some measure of the magnitude of the elements of the matrix. The norms used are L_1, L_∞ and L_f. These norms are defined as [49]

$$L_1 = \arg \max_{1 \le j \le n} \sum_{i=1}^{m} |a_{ij}| \tag{90}$$

$$L_\infty = \arg \max_{1 \le j \le m} \sum_{i=1}^{n} |a_{ij}| \tag{91}$$

$$L_f = \left(\sum_{i=1}^{m} \sum_{j=1}^{n} |a_{ij}|^2 \right)^{\frac{1}{2}} \tag{92}$$

where a_{ij} represents an element of a matrix. When there are strong targets present in a uniform background, we get a distribution with higher values for matrix norms. However, once we locate the targets, and remove their contributions from the array data, the power distribution deceases along with a reduction in the values of the norms. Hence, one way to decide when to stop is to calculate this distribution along with the metric, after localizing each target. If the values in the metric become too small as compared to the starting value, then this is an indication that there are no stronger targets. To simulate this scenario, an AT mine (VS2.2) and a rock of nearly same size and shape are buried at a depth of 6 cm. Both these targets are nearly at the same distance from the source, with the rock being slightly closer. Both the rock and the mine are shown in Fig. 57. Assuming that

(a) (b)

Figure 57: Experimental setup showing the relative position and size of a VS2.2 mine and a rock, both buried at a depth of 6 cm. (a) Relative position with respect to the source. (b) Relative size.

there is only one target, we let the array maneuver optimally. At the first probe phase, the array seems to locate the rock as compared to the mine. After a few iterations rock is localized with reduced uncertainty. The probe phase and the location estimates after the last optimal move are shown in Fig. 58. After this, the same steps are repeated again, with the contributions of the already localized target removed from the array. This time the array moves toward the second target (the mine) and localizes it in three optimal moves as shown in Figs. 59(a,b).

During the maneuvering we can also calculate the power distribution and three metrics based on the various norms (90,91,92). The power distribution is calculated only when the array is in the probe position as shown in Fig. 58(a). At first there are two strong targets. The histogram of this power distribution is shown in Fig. 60(a), with calculated values of the three norms shown in the first row of Table 3. Then once this target is localized, we can remove its contribution from the array at the same probe position. This power histogram is shown in Fig. 60(b) with the norm values shown in the second row of Table 3. The power histogram when both targets are removed is shown in Fig. 60(c), and the calculated metric values are shown in third row of Table 3. These values should be the same as those for an empty sandbox. These values will be used to define a stopping criteria in the next section.

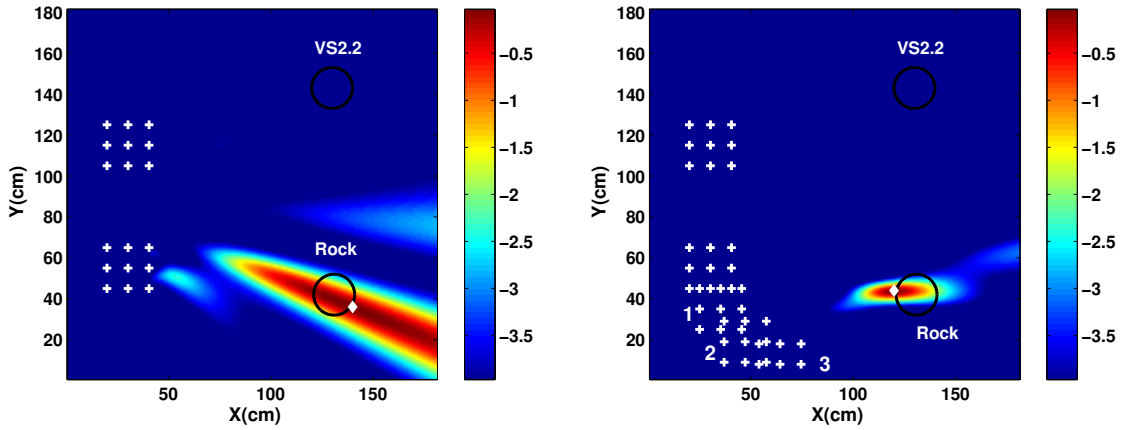

(a) (b)

Figure 58: VS2.2 mine and a rock case. Maximum likelihood surfaces at two steps (dB scale) (a) After the probe phase, two fixed array positions with respect to source are used. (b) After the last (third) optimal move.

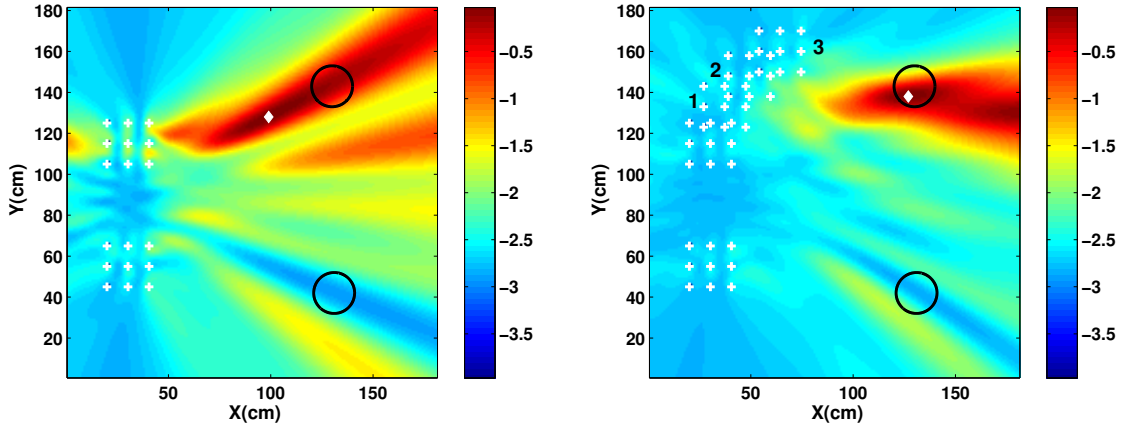

(a) (b)

Figure 59: VS2.2 mine and a rock case. Strongest target contribution has been removed from the array. Maximum likelihood surfaces at two steps (dB scale). (a) After the probe phase, two fixed array positions with respect to source are used. (b) After the last (third) optimal move.

Table 3: Metric calculation for power distribution using matrix norms.

	L_1	L_∞	L_f
Initial	40.28	43.28	31.58
Rock removed	14.57	18.24	12.45
Both rock and mine removed (empty sandbox)	8.31	9.83	7.24

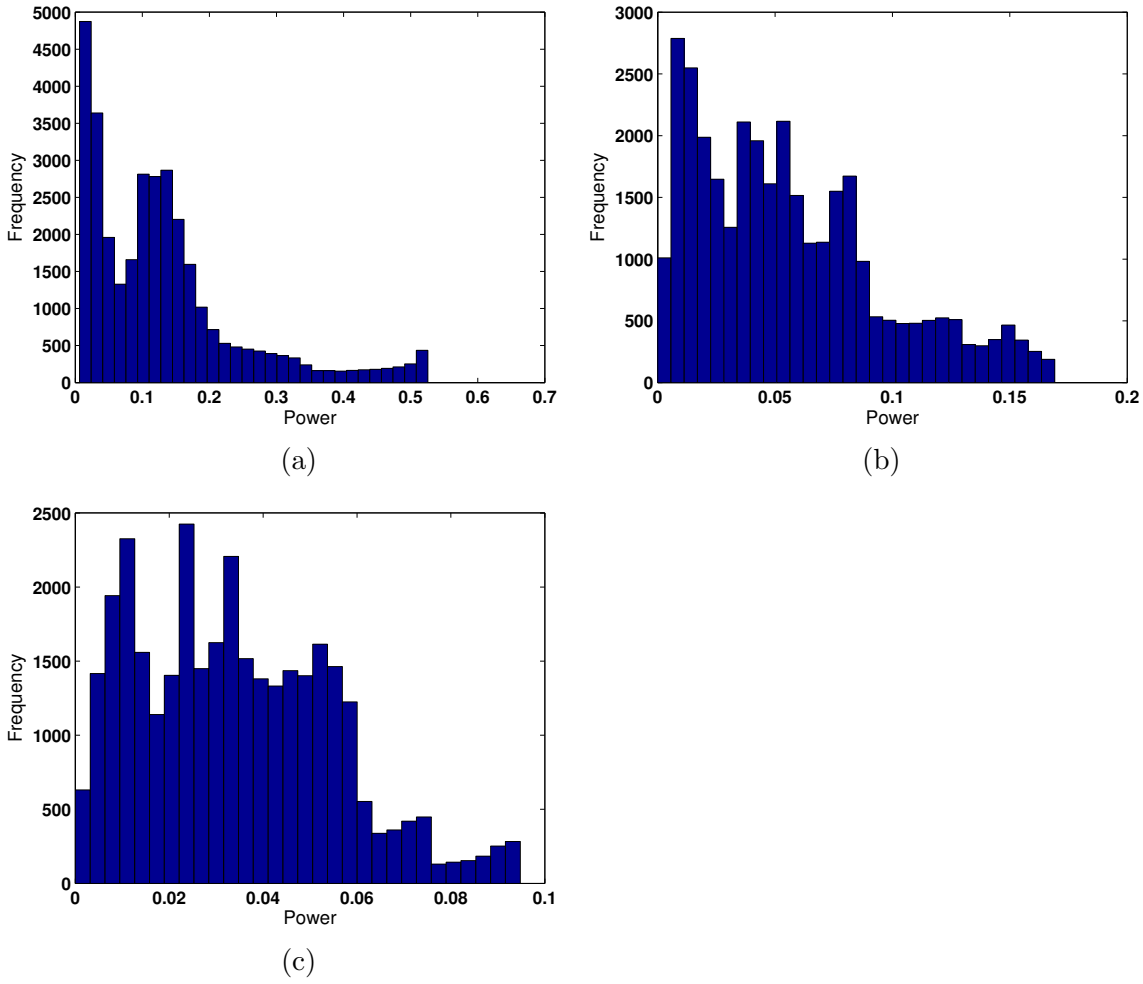

Figure 60: Power histogram at the probe phase. (a) With both targets present. (b) With one stronger target removed (the rock). (c) With both stronger targets removed (both the mine and the rock).

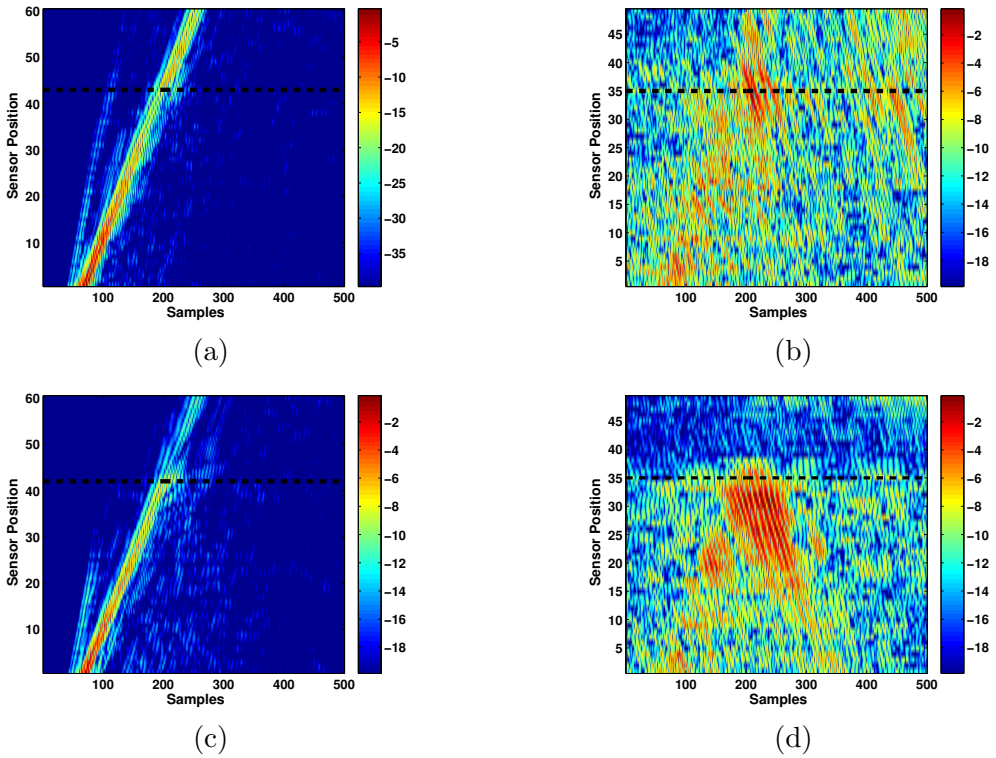

Figure 61: Scans over the localized target positions (dB scale). Targets positions are shown by a horizontal black line. (a) Raw data collected over the VS2.2 mine. (b) Extracted reflected waves for scan over the VS2.2 mine. (c) Raw data collected over the rock. (d) Extracted reflected waves for the scan over the rock.

Once we have localized the targets, we can do further processing to extract their resonance/reflection signature for final confirmation. The algorithm is presented fully in Chapter 7. A linear scan is done along the line connecting the source to the already localized positions. Both reflected waves and forward waves can be extracted from this raw data, which will be used in an energy based algorithm. The raw collected data for the mine and rock case is shown in Figs. 61(a,c), and the reflected waves extracted from these scans are shown in Figs. 61(b,d) for the mine and rock, respectively. The rock signature is very strong, so the array tends to pick this at the first stage as compared to the mine. The energy calculated for these reflected waves using the algorithm outlined in Section 7.2 is shown in Fig. 62. Again the rocks appear somewhat stronger than the mine in this case.

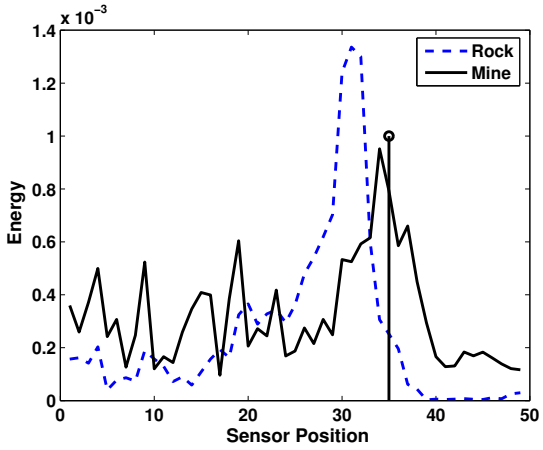

Figure 62: Energy calculation for scans over the VS2.2 mine and the rock (linear scale). The rock signature is stronger than the mine. Position of the mine and rocks are shown by vertical line.

6.6.3 Strategy for Multi-target Cases

Based on the two previous examples we can formulate an ad-hoc strategy for dealing with multi-target cases. In most realistic situations, we don't have any prior knowledge of the number of targets. The simplest strategy is to locate each target one at a time, so we can start by assuming that there is only one strong target. The probe phase might gave an indication of how many targets are there, or it might not. In experiment:1 the probe phase indicates two strong targets, whereas in experiment:2, it indicates that there is only one target, even though there are actually two. Hence, at the first iteration, we can assume that there is only one strongest target, and will try to localize it optimally. Once it is localized, we can remove its contribution from the array by using the CLEAN algorithm, and try to find the next strong target. We can continue with this strategy, but we will need a way to stop. The power distribution will come into play for defining this stopping criteria. At each probe stage, we will also calculate the power distribution, along with its metric as given in Table 3. As we remove each localized target contribution from the array, we will see a reduction in the power metric values. This reduction can be used as a guide to when to stop looking. The metric values for an empty sandbox can be used for this criteria for laboratory experiments. One example of these values calculated for different experiments are shown in Fig. 63. At each run we locate the target, and find the metric. For the next

Table 4: Metric calculations for power distribution for different scenarios shown in Fig. 63.

	L_1	L_∞	L_f
Case 1: Single AT mine and a rock			
Initial	40.28	43.28	31.58
Rock removed	14.57	18.24	12.45
Both rock and mine removed	8.31	9.83	7.24
Case 2: Single AP mine and a 4 rocks			
Initial	21.25	22.58	19.39
Rock removed	12.23	15.33	11.6
Both mine and a single rock removed	9.08	9.68	7.98
Case 3: Single AP mine			
Initial	16.28	16.25	13.07
Mine removed (empty sandbox)	9.34	12.56	7.41

run we remove the already localized target, and then find next target along with metric. The metric converges to nearly the same values after removing all the strong targets from the sandbox. In order to have the lower limits on the values of the metric, we can use the array data for an empty sandbox, that is when there are no targets present. As an example we can use the data set with a single TS50 mine, and calculate the metric value with the contribution of the mine removed from the array. In the case the calculated metric values are 9.34, 12.56 and 7.41 for L_1, L_∞ and L_f respectively. We can use a 15% rule, i.e. whenever any (logical OR operation) of the metric values reach within $\pm 15\%$ of these value we will stop looking for the targets. All these values used in Fig. 63 are shown in Table 4. Therefore, for realistic situations we might have to calibrate the array by using an area without any targets to calculate the bench mark metric values for the stopping criteria. The power distribution will depend upon several factors like types, sizes and burial depths of targets, also the propagation properties of the medium, and dynamic range of seismic source.

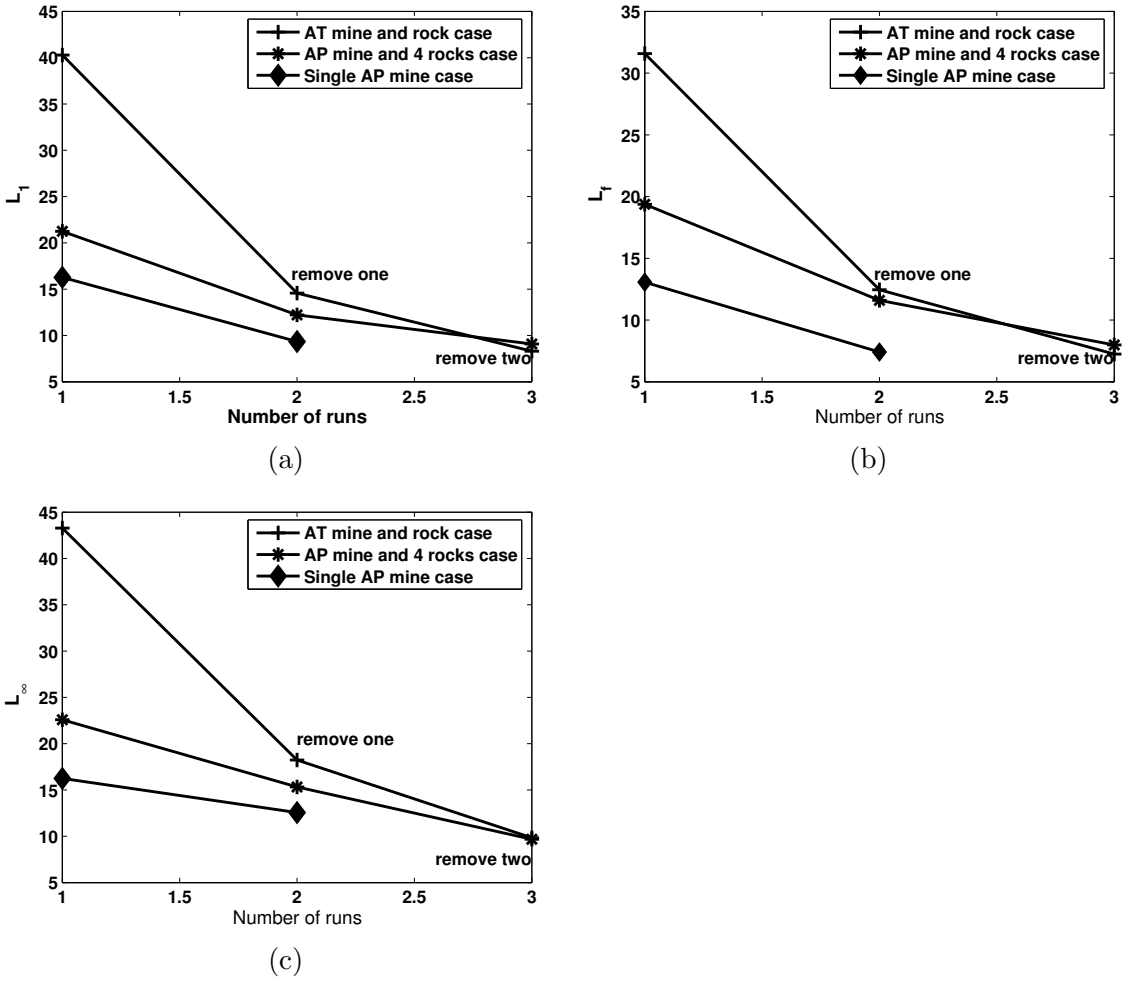

Figure 63: Calculation of three metrics at different run for three different cases with different distribution of targets (mines and rocks). At each run we calculate the strongest target along with the metric. After this, remove this target, and find next strongest and metric. The values should converge to that for an empty sandbox, when all stronger targets are located and removed. (a) L_1 (b) L_f (c) L_∞.

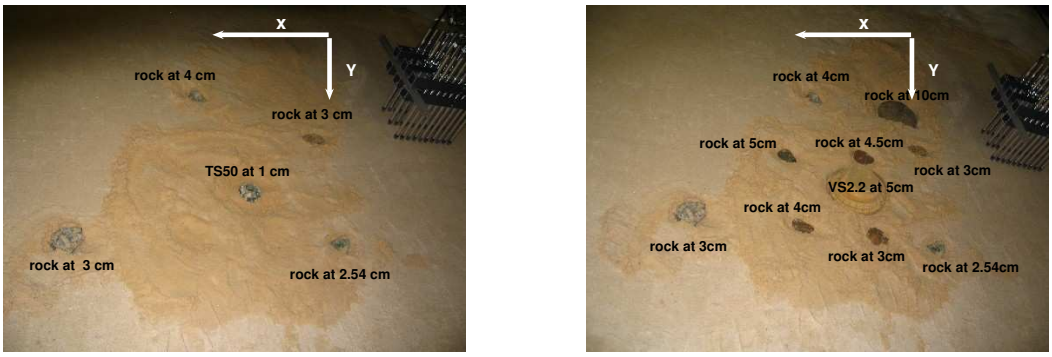

(a) (b)

Figure 64: Experimental setup showing relative positions of mines and rocks (a) TS50 mine buried at 1 cm surrounded by four rocks. (b) VS1.6 mine buried at 5 cm surrounded by nine rocks of various sizes and shapes.

6.7 Targets in Clutter Case

To simulate clutter rocks are introduced in addition to landmines. The fact that landmines resonate, and hence have more reflected energy, can be used to discriminate them from clutter such as rocks. However, rocks also scatter the seismic waves, just like landmines. Therefore, discriminating the rocks from landmines with the method of optimal maneuvers depends upon their relative positions with respect to the source, and their burial depths. In these experiments rocks are introduced to confuse the system in locating mines. One of the experiments is conducted with a TS50 mine surrounded by a large number (8) of rocks. This is done to test how the system behaves for an extreme case. In another experiment a big rock is placed very near to the source, in addition to an AT mine and other rocks. From these experiments we gain some insight on the limiting (extreme) cases, where the system might fail to find landmines.

6.7.1 Experiment:1

The first experiment is with a small TS50 AP mine buried at a depth of 1 cm surrounded by four rocks which are nearly the same size as the mine. The locations and burial depths of the rocks and the mine are shown in Fig. 64(a).

The location estimate using optimal maneuvers is shown in Fig. 65, and the array is

able to pick out the target even in the presence of these rocks. However, an interesting question is what happens if we remove the contribution of this localized mine from the array data. Can we find the rocks after this? The power histogram for this case can give us a clue. The histograms are shown in Figs. 66(a,b), with the mine present and removed, respectively. The metric values for the power distribution for this case are given in Table 4. Clearly after removing the mine, the metric didn't drop close to the stopping criteria. Therefore, we would go ahead and try to locate the next target. The optimal maneuvers after the mine contribution is removed from the array are shown in Fig. 67 which shows that after few optimal moves we can find one of the rocks. After this the metric values as given in Table 4 drops into the range for the stopping criteria, and we quit processing after this. For confirmation linear scans are done over the two localized positions as shown in Figs. 68(a,c). The extracted reflected waves are shown in Figs. 68(b,d). Clearly there is very strong signature from the mine in the form of resonance. The energy can also be calculated for these scans using the algorithm in Section 7.2. As shown in Fig. 69, the mine signature is much stronger than that of the rock.

6.7.2 Experiment:2

In the second experiment whose setup is shown in Fig. 64(b), a VS1.6 AT mine is surrounded by nine rocks. The optimal maneuvers to locate the mine are shown in Figs. 70(a,b,c,d). Since the VS1.6 is a big mine, its signature is very strong as compared to the rocks. Hence, it can be picked out of rocks very easily.

6.7.3 Experiment:3

In an another experiment, a single TS50 AP mine is buried at a depth of 1 cm surrounded by 8 rocks of various sizes and depths. The setup showing the location of mine and rocks is given in Fig. 71(a). The location estimates from the probe phase and first optimal move are shown in Figs. 71(b,c). Clearly the array is not able to find any specific target, however it does find one of the rocks, and moves toward it. However, the resolution of the image overall is very low. It is interesting to plot the power histogram for this case, shown in Fig. 71(d), with the calculated metric values are 12.8, 15.5 and 11.56 for L_1, L_∞ and L_f,

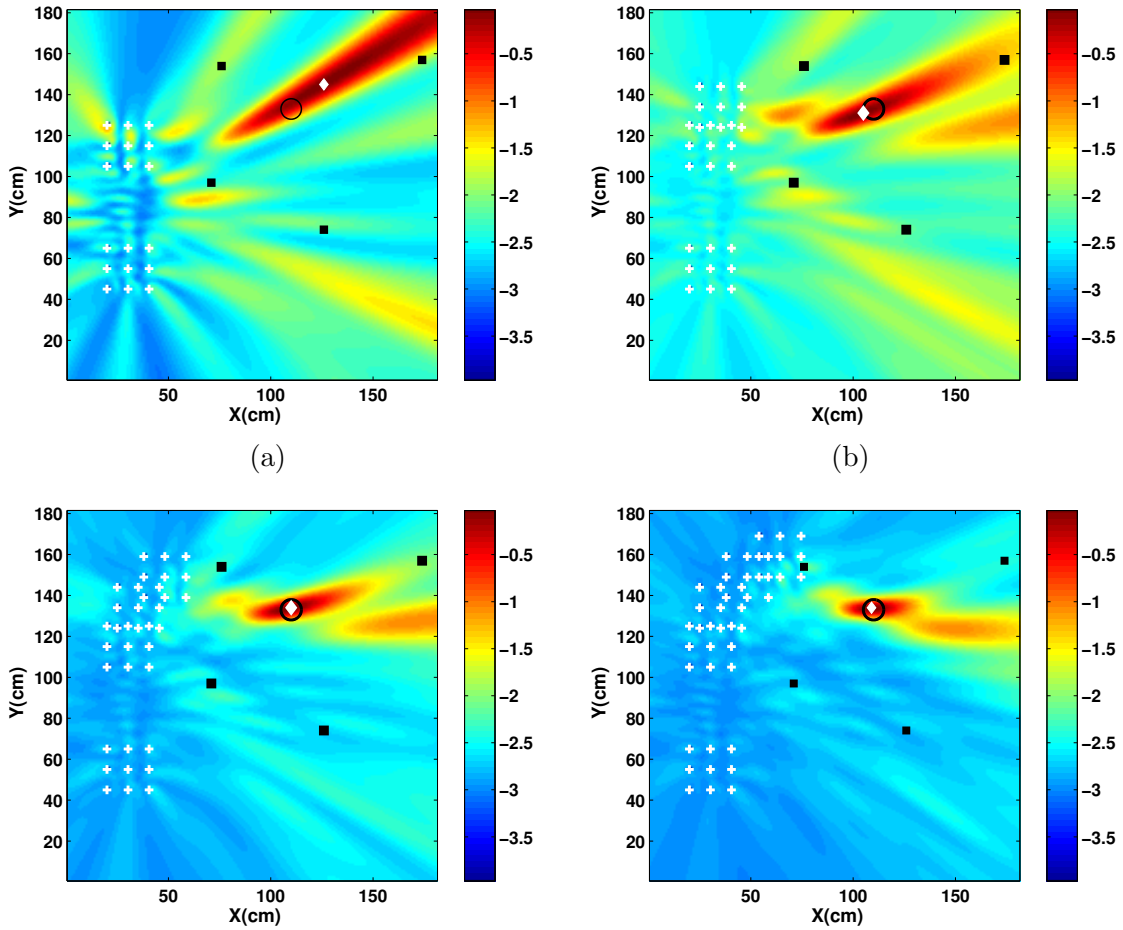

Figure 65: TS50 mine buried at a depth of 1 cm surrounded by 4 rocks. Maximum likelihood surfaces at various probing steps (dB scale). Mine position and size is shown by small black circle, white diamond shows the position estimate, and black squares show the rocks positions. (a) After the probe phase, two fixed array positions with respect to source are used. (b) After the first optimal move. (c) After the second optimal move. (d) The final target position estimate.

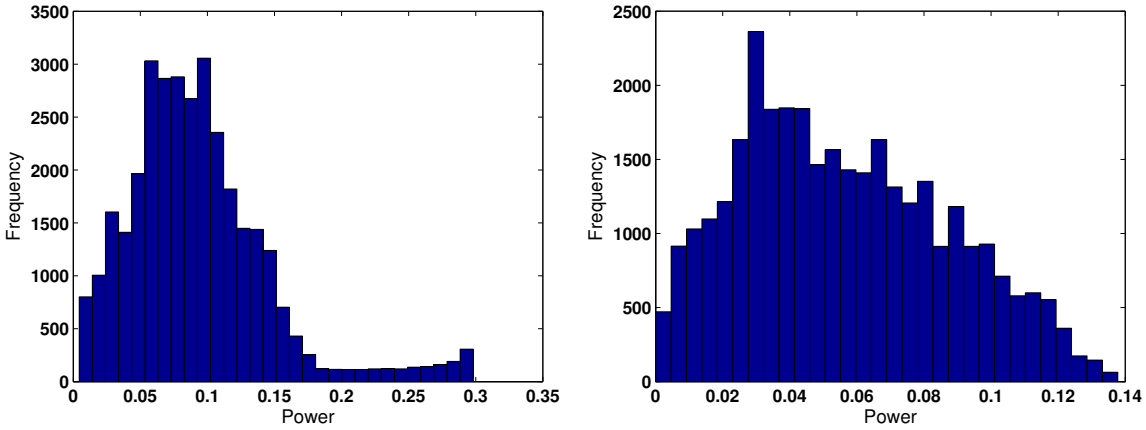

(a) (b)

Figure 66: Power histogram at probe phase for a TS50 mine surrounded by 4 rocks. (a) With mine present. (b) With mine contribution removed from the array.

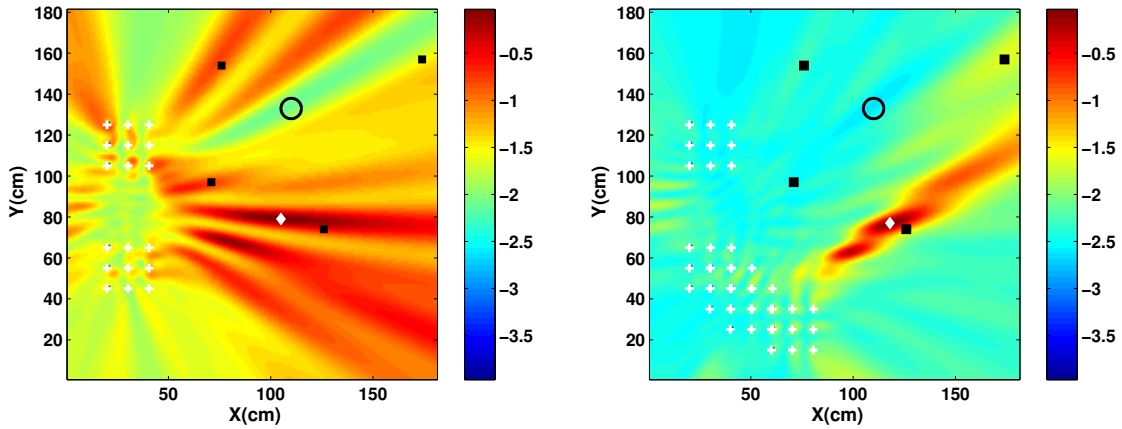

(a) (b)

Figure 67: TS50 mine buried at a depth of 1 cm depth surrounded by 4 rocks. Maximum likelihood surfaces at various probing steps (dB scale). The contribution of the mine is removed from the array at each step. (a) After the probe phase, two fixed array positions with respect to source are used. (b) After final optimal move, where the array locates the rock.

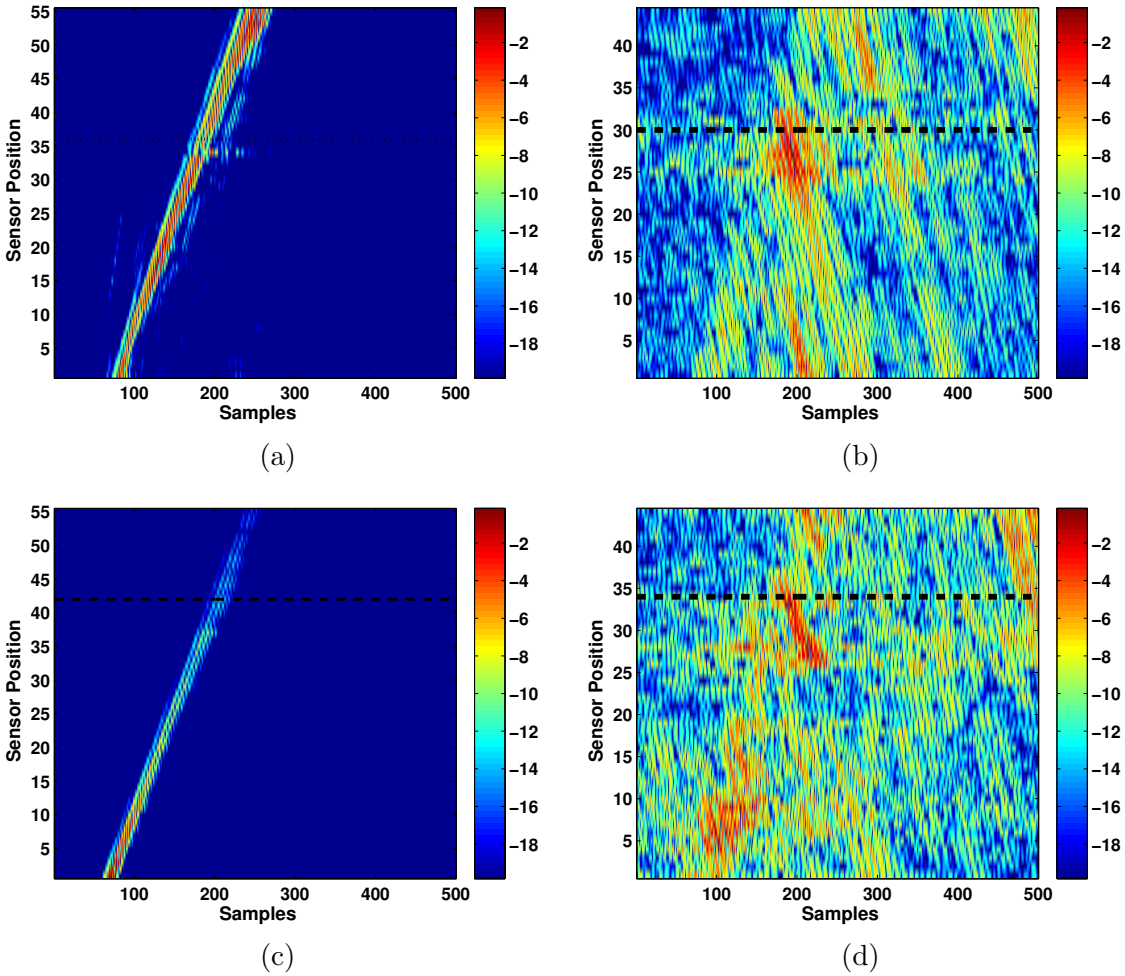

Figure 68: Scans over the localized target positions. Target positions are shown by horizontal black lines (dB scale). (a) Raw data collected over the TS50 mine. (b) Extracted reflected waves for scan over the TS50 mine. Strong resonance can be seen at the mine location. (c) Raw data collected over one of the rocks. (d) Extracted reflected waves for the scan over the rock.

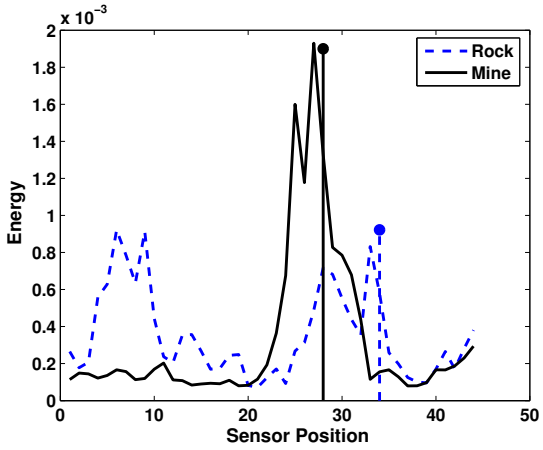

Figure 69: Energy calculation for scans over the TS50 mine and one of the localized rocks (linear scale). The mine signature is much stronger than rock. Positions of the mine and the rock are shown by vertical lines.

respectively. These values are very near to the stopping criteria, which we used in earlier cases. This is the reason that why the array is not able to find anything strong out of all the targets.

6.7.4 Experiment:4

In another experiment a big VS1.6 AT mine is buried at 5 cm along with nine rocks. One of the rocks is of the same size as the mine, and it is buried at a depth of 6 cm, very near to the source. The source in this case is located at x= -42 cm and y= 85 cm. Since the rock is of comparable size to the mine and also very near to the source, the array picks up this rock, and moves towards it. The setup and the optimal moves are shown in Figs. 72(a,b,c,d).

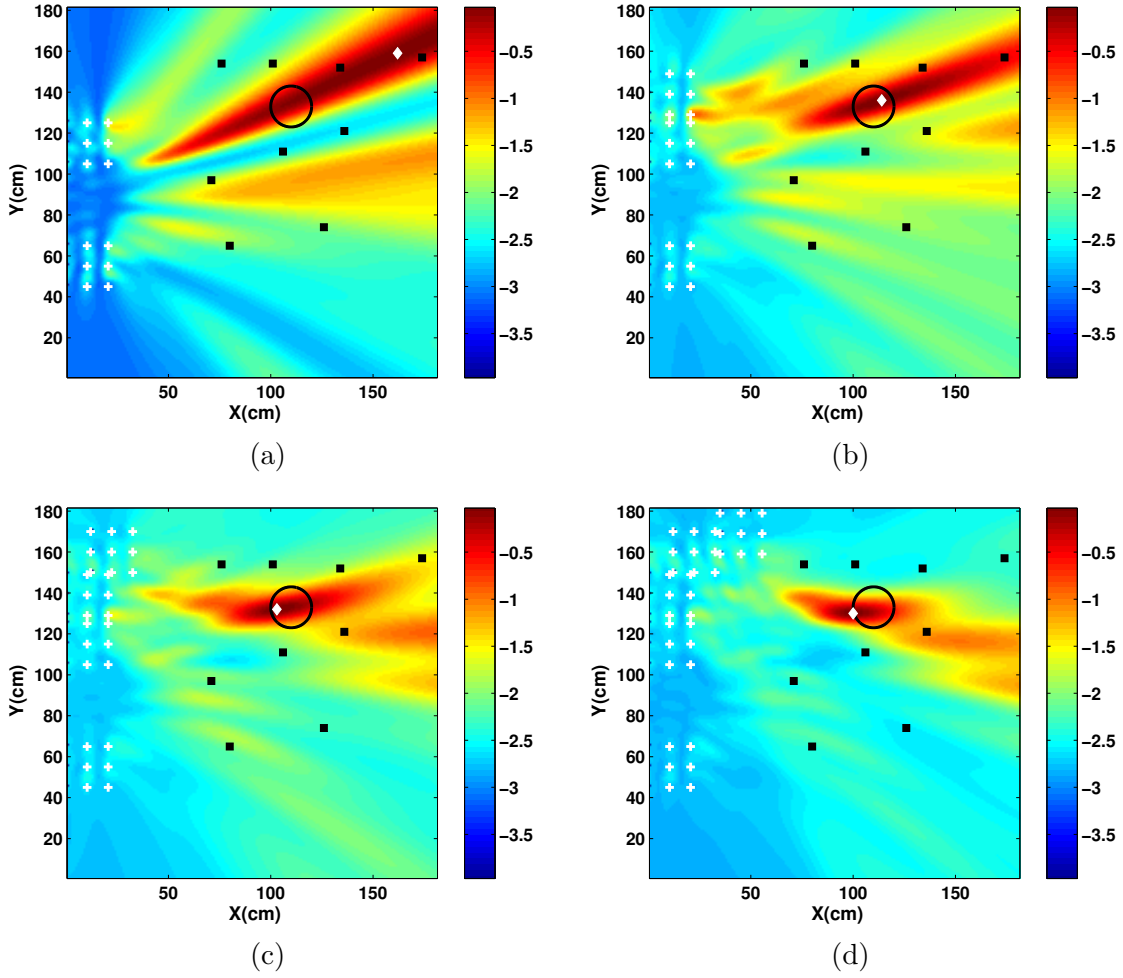

Figure 70: VS1.6 mine buried at a depth of 5 cm depth surrounded by 9 rocks. Maximum likelihood surfaces at various probing steps (dB scale) (a) After the probe phase, two fixed array positions with respect to source are used. (b) After the first optimal move. (c) After the second optimal move. (d) The final target position estimate is shown.

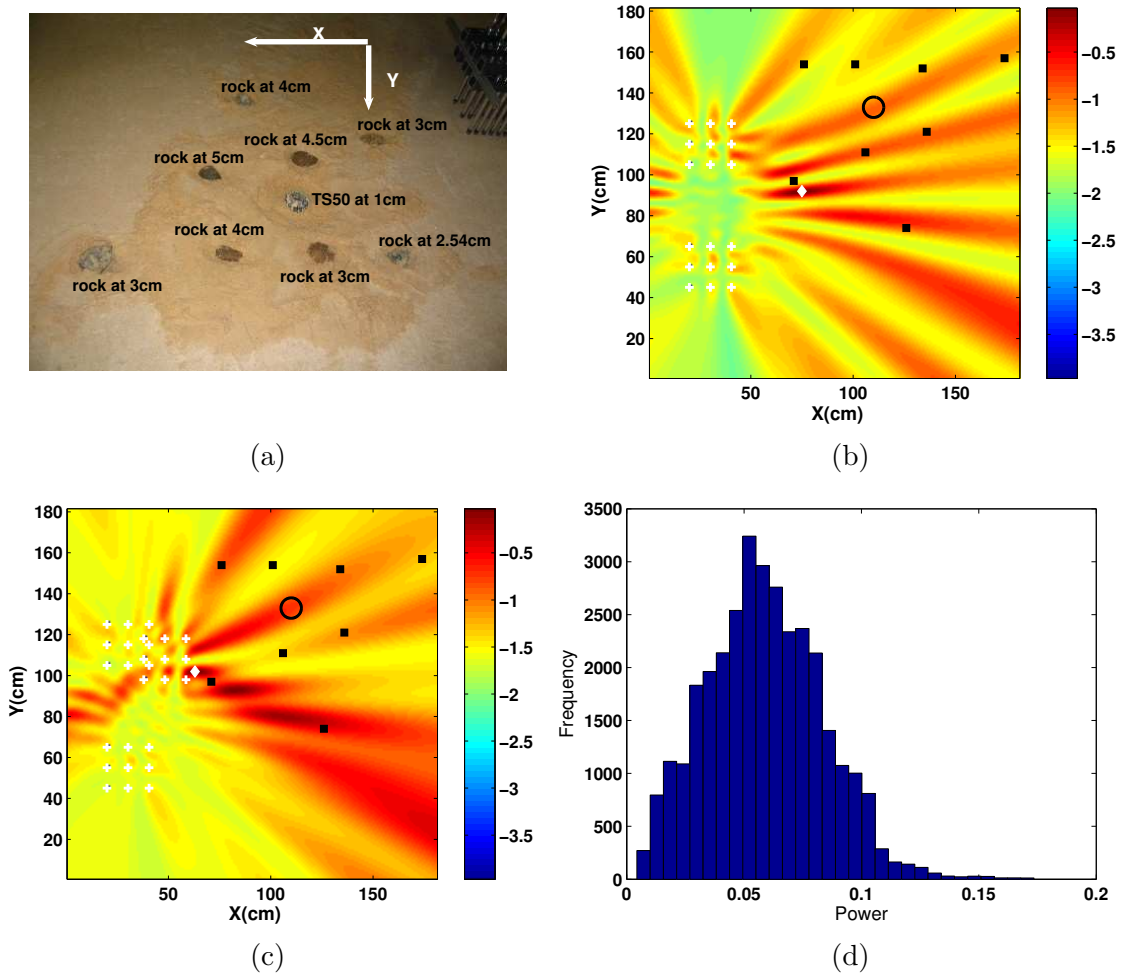

Figure 71: TS50 mine buried at a depth of 1 cm surrounded by 8 rocks. (a) Setup showing the positions and burial depths of the mine and rocks. (b) ML surface at the probe phase. The array seems to pick up one of the rocks, with very low image resolution. (dB scale) (c) ML surface after the first optimal move. The array moves toward one of the rock. (dB scale) (d) Power histogram when the array is at the probe position in (b).

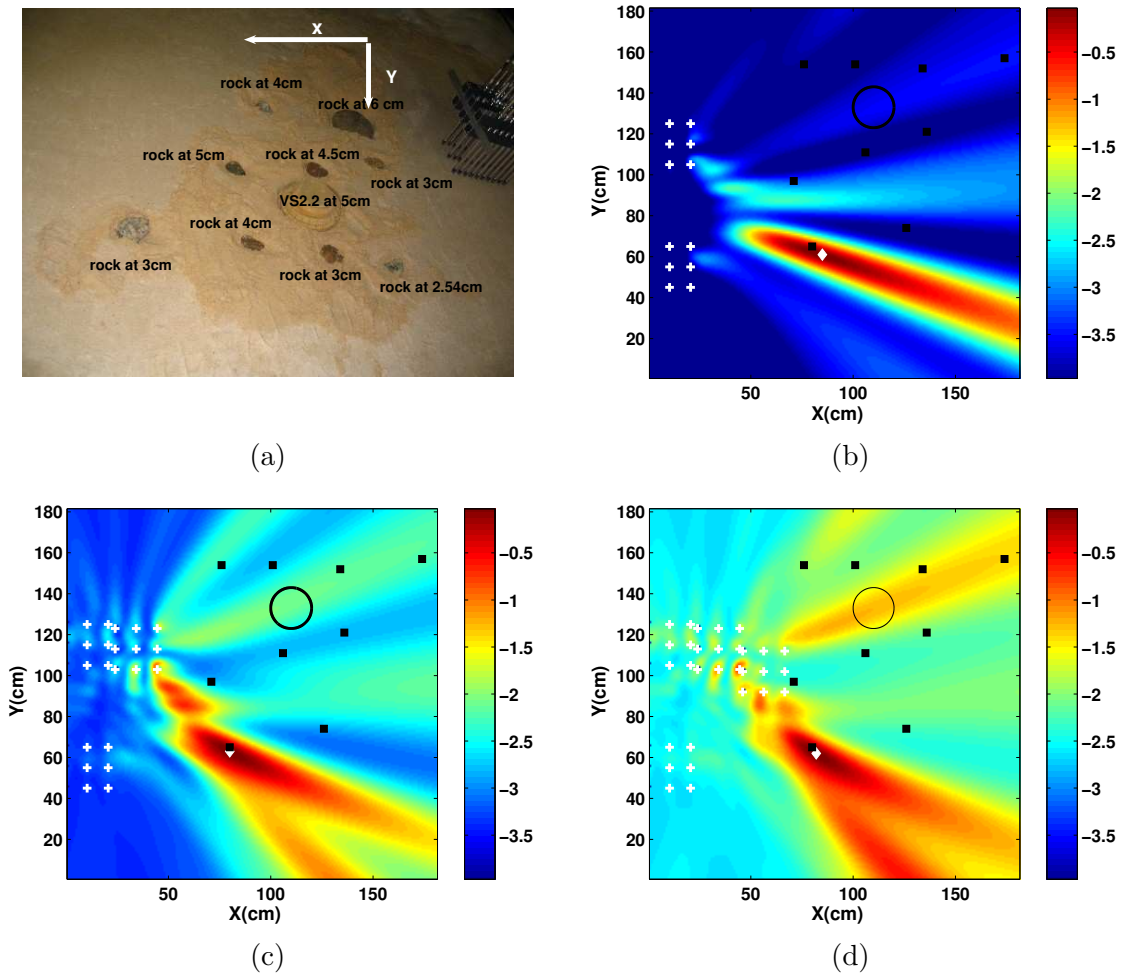

Figure 72: VS1.6 mine buried at a depth of 5 cm surrounded by 9 rocks. (a) Setup showing the positions and burial depths of the mine and rocks. (b) ML surface at the probe phase. The array seems to pick up one of the big rocks located near the source (dB scale). (c) ML surface after the first optimal move. The array seem to moves toward one of the rocks (dB scale). (d) ML surface after the second move (dB scale).

6.8 Drunken Wave Case

The drunken waves are generated whenever there is a drastic surface change in the propagation properties of the intervening medium. With such a change, waves can take a curved route instead of propagating on a straight path. The main pulse might not strike the mine, and hence it will be difficult to locate them. This bending causes problems for back-propagation algorithms which rely on accurate velocity estimation as shown in [64]. The position estimates will be wrong because of the bending of the wave path. Therefore, it will be interesting to see how the optimal maneuvering algorithm handles the drunken wave case. Two cases will be presented for the drunken wave. In the first case, the main pulse of the wave bends and the mine is not placed in the path of main pulse. In the second case, a mine is placed right in the path of bending main pulse of the wave. These drunken waves were generated in a sandbox by changing the soil properties of some portions of the sandbox. These properties can also be affected by water content and the degree of cohesion between sand particles. A TS-50 AP mine, buried at a depth of 1 cm is used for these experiments. A single large shaker is used as a seismic source.

6.8.1 Case 1: Mine is not in the path of main pulse of bended waves

The surface displacement plots for this case are shown in Fig. 73, which shows seismic waves at four different time instants. In the ideal case, waves should pass straight through the center of scan region, but in this case the waves bend and turn to right. It is very difficult to pick the mine from this raw data, and the only indication is in Figs. 73(b,c), where the position of the mine is indicated by an arrow. A weak indication of resonance can be seen at the mine location. The results of applying optimal maneuvering to this case are shown in Figs. 74(a,b,c,d). For this drunken wave, it is surprising that the algorithm is able to pick up the mine with exact location estimates, and reduced uncertainty.

In order to confirm whether the localized position contains a legitimate target, waves are separated as in the previous examples. The raw collected data and extracted reflected waves are shown in Figs. 75(a,b). The reflected waves show a considerable resonance at the mine location, hence confirming that this is a genuine target.

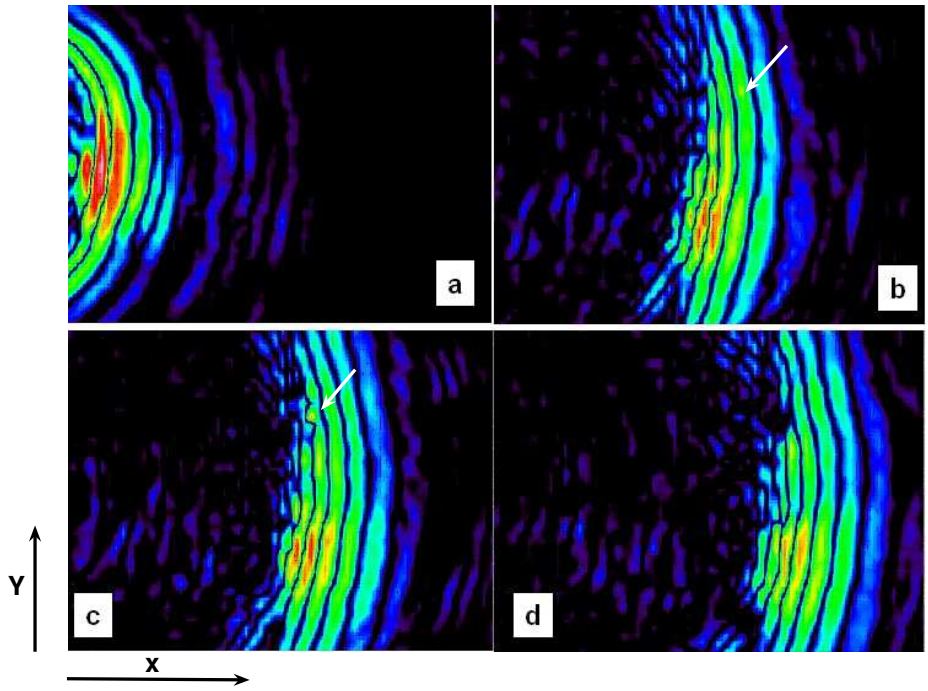

Figure 73: Drunken wave case. Surface displacement showing the interaction of waves with a TS-50 mine buried at a depth of 1 cm, at four instants. Location of mine is shown by an arrow (40 dB scale), (a) wavefronts at the start of the scan region (b) at the middle. Waves start to bend, and the main pulse goes to the right (c) at another instant, a weak resonance can be seen at the mine location (d) main pulse has bent toward the right and out of the scan region.

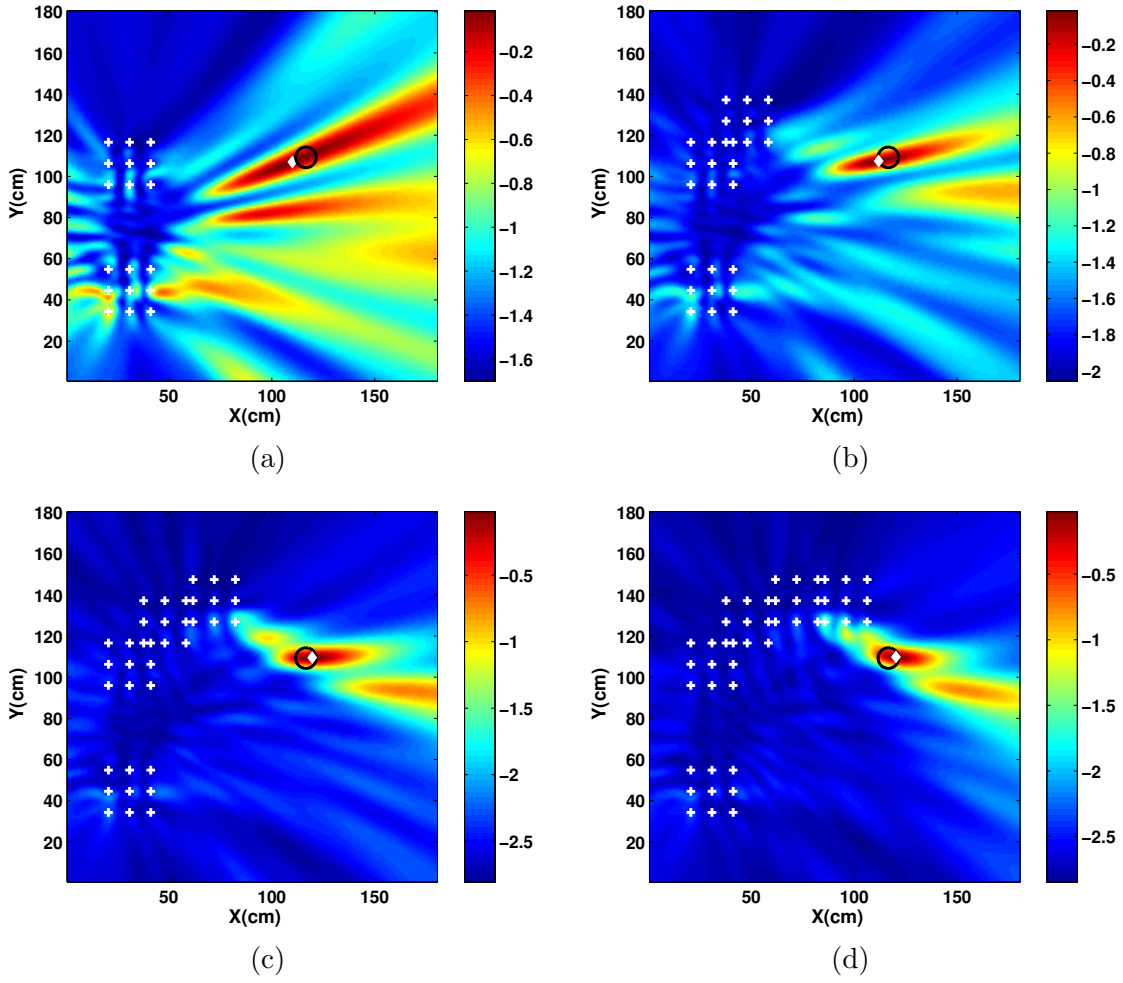

Figure 74: Drunken wave case for a TS-50 mine buried at a depth of 1 cm. Maximum likelihood surfaces at various stages (dB scale). (a) Probe Phase: two fixed array position are used. (b) After the first optimal move. (c) After the second optimal move. (d) After the final move.

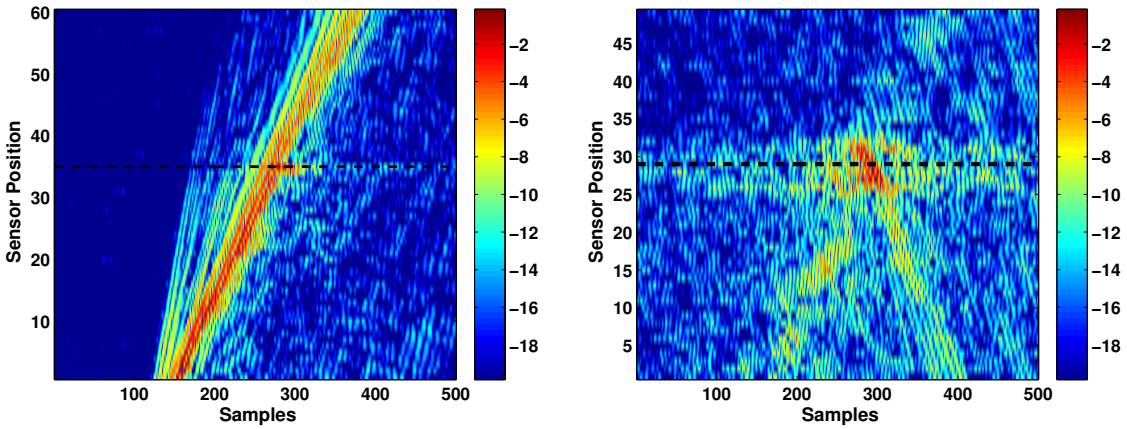

(a) (b)

Figure 75: Drunken wave case. Wave separation at the localized position. Location of the mine is shown by the horizontal line (dB scale). (a) Collected raw data, (b) extracted reflected waves.

6.8.2 Case 2: Mine is in the path of main pulse of bended waves

The surface displacement plots for this case are shown in Fig. 76, which shows seismic waves at four different time instants. The presence of the mine can be seen in Figs. 76(b,c,d), where the position of the mine is indicated by an arrow, and the resonance can be seen at the mine location. The results of applying the method of optimal maneuvers to this case are shown in Figs. 77(a,b,c,d).

For confirmation, the waves are separated as in the previous examples. The raw collected data and the extracted reflected waves are shown in Figs. 78(a,b). The extracted reflected waves show the presence of the mine.

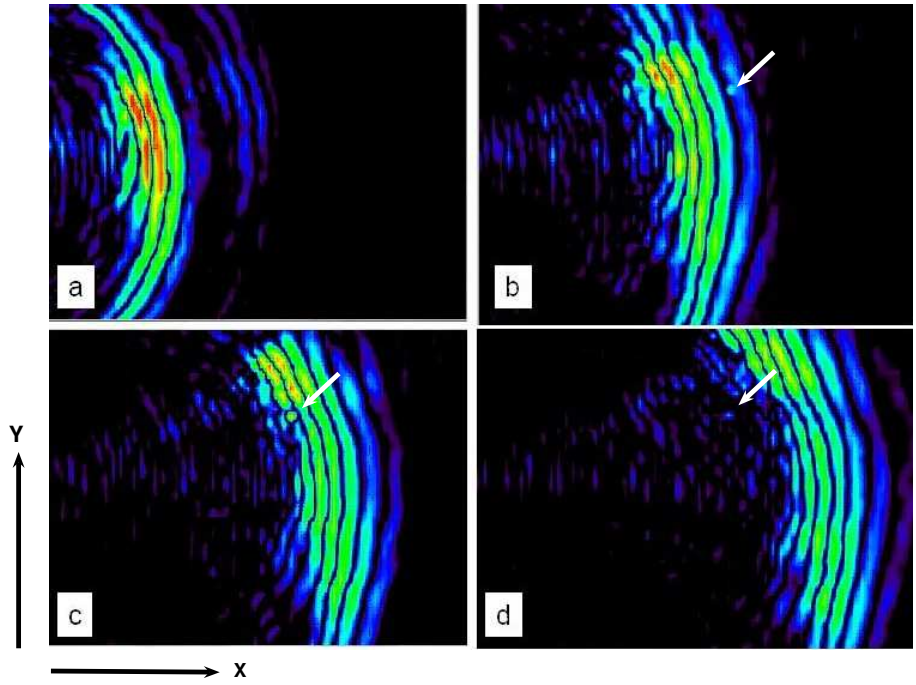

Figure 76: Drunken waves case. Surface displacements showing the interaction of waves with a TS-50 mine buried at a depth of 1 cm, at four instants. Location of the mine is shown by an arrow (40 dB scale), (a) wavefronts at the start of the scan region (b) at the middle. Waves start to bend, and the main pulse goes toward left (c) at another instant, the resonance can be seen at the mine location (d) main pulse has bent toward the left and out of the scan region.

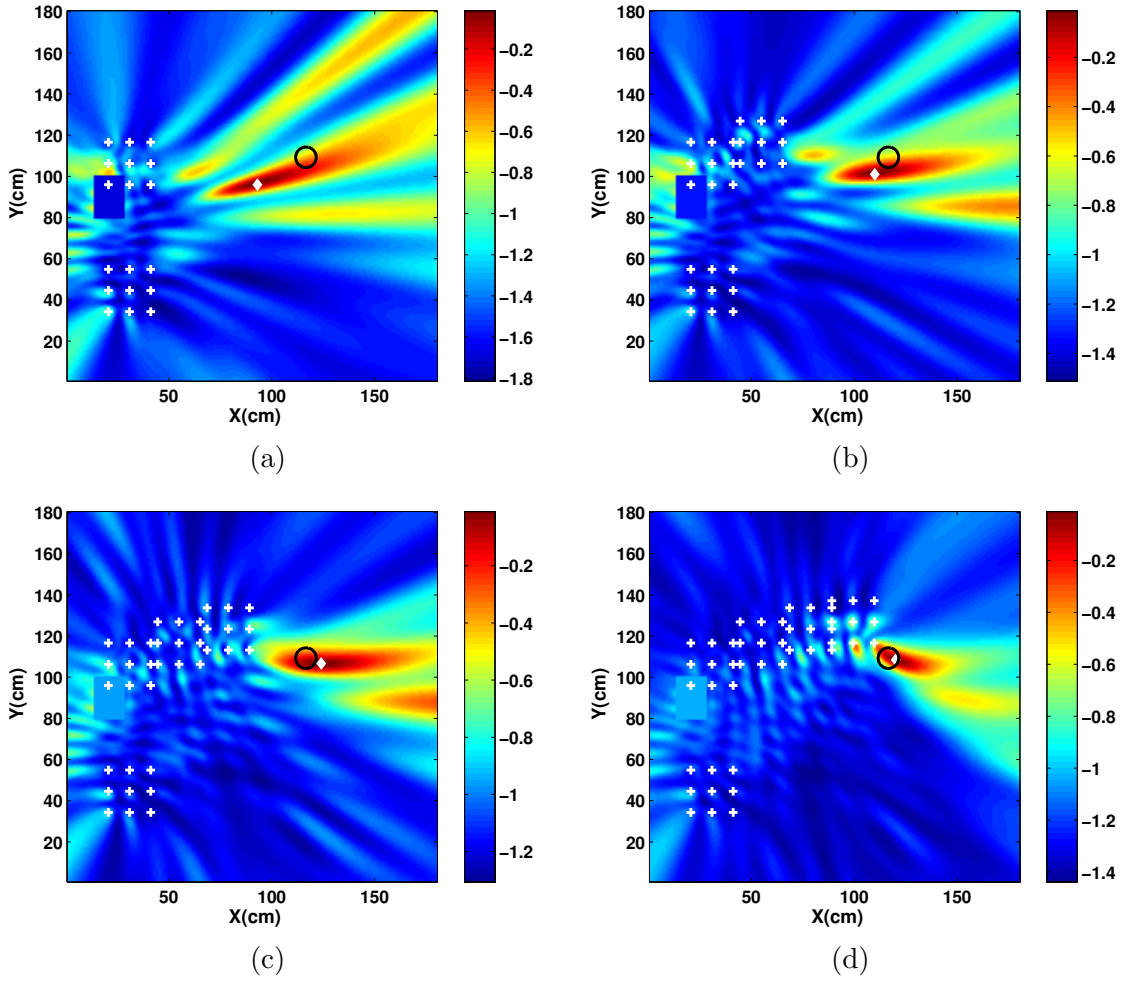

Figure 77: Drunken wave case for a TS-50 mine buried at a depth of 1 cm. Maximum likelihood surfaces at various stages (dB scale). (a) Probe Phase: two fixed array position are used. (b) After the first optimal move. (c) After the second optimal move. (d) After the final move.

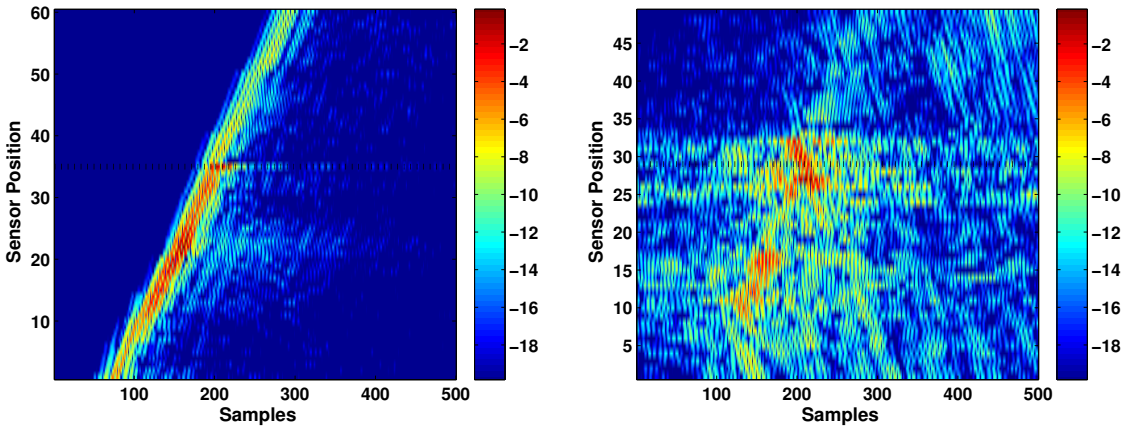

(a) (b)

Figure 78: Drunken wave case. Wave separation at the localized position. Location of the mine is shown by the horizontal line (dB scale). (a) Collected raw data, (b) extracted reflected waves.

6.9 Conclusions

In this chapter, a detailed analysis of a number of experiments were presented which have been conducted for different scenarios. First of all, a multi-phase algorithm was presented consisting of probe, search and detection phases. Results were presented for different kinds of single targets (AP and AT mines). Also, a strategy for the multi-target case was presented, and validated by experiments. In order to prove the robustness of the algorithms, clutter in the form of rocks was introduced along with resonating targets like landmines. The algorithm proved to be quite robust in locating mines in the presence of clutter. However, the performance depends upon the sizes, burial depths and proximity to the seismic source for both the mines and the rocks. Finally, results of the processing for drunken waves was given. These waves are produced when there is a large change in the propagation properties of the medium, and the waves bend instead of going on a straight route. The algorithm was again found to be robust enough to deal with these cases.

CHAPTER VII

DETECTION MODE: IMAGING AND DETECTOR FRAMEWORK

7.1 Introduction

Before the final detection/confirmation stage, we are assuming that the optimal maneuvering phase has detected the presence and location of the target. The next step is to extract any resonance/reflection, and also to formulate the imaging and detector framework. The imaging algorithm presented in this chapter uses the extracted forward and reflected waves and is a generalization of the algorithm presented in Section 1.1.2 [11]. In the proposed algorithm, an energy image is formed by using the product of the extracted forward and reflected waves. This product is very strong at reflectors where the forward and reflected waves are coincident. It is further enhanced by resonance in some man-made targets. Using the energy image, a likelihood detector is formed to make the final detection. This detector is based on the Generalized Likelihood Ratio Test (GLRT) [40, 69], and is used to identify areas with the highest probabilities of having targets [4]. The following sections will describe the imaging algorithm and detector framework.

7.2 Imaging Algorithm

A new localization and detection algorithm can be based on the forward and reflected wave separation performed by IQML on the raw data. If we have a linear array of M sensors with an inter-sensor spacing of Δx, the effective aperture is $M\Delta x$. This linear array can be moved forward on a straight line, Δx at a time. At each array position, IQML separates and reconstructs the forward and reflected Rayleigh waves. If there is a target near the array then we will see a strong reflected wave and possibly a resonance in the extracted data. This reflected wave can be plotted by itself, or an image based on the product of the extracted forward and reflected waves can be formed. Since the only place where the

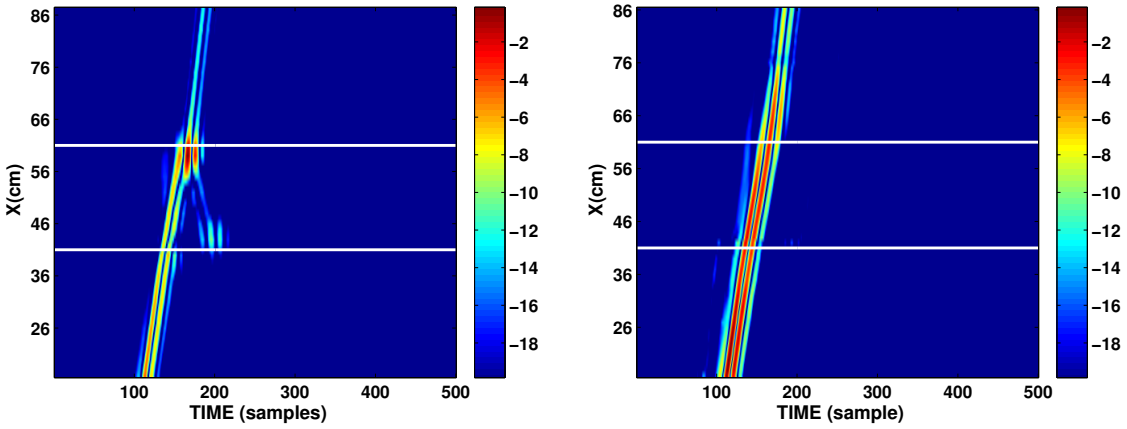

Figure 79: VS-1.6 mine (20 cm diameter) buried at a depth of 5 cm. Front and back edges of the mine are denoted by horizontal white lines (dB scale). Space-time plots of (a) the collected data at the center sensor for all window positions, (b) Extracted forward wave.

reflected and forward waves meet is at the target location, this product image can be used to determine the exact target location.

The effectiveness of this product image for location can be demonstrated with an example using an anti-tank mine (VS-1.6) buried at a depth of 5 cm. A linear array consisting of 31 sensors (window) is moved 1 cm at a time across the target. At each array position the extracted waves are reconstructed at the middle sensor (the 16th) and are saved for use in the final plot. The collected data at the center sensor, for all the window positions, is shown in Fig. 79(a), where the front and back edges of the mine are denoted by two horizontal lines. The VS-1.6 mine is an anti-tank (AT) mine with a diameter of 20 cm. The extracted forward wave is shown in Fig. 79(b), and the extracted reflected wave in Fig. 80(a). All the images are shown on a 20 dB scale, and each image is normalized to its own maximum value so that its peak corresponds to 0 dB. In this example, the extracted reflected wave shows a very strong reflection where the mine is located. The product of the reflected and forward waves is shown in Fig. 80(b), and the position of the land mine is easy to see, especially the back edge.

Another imaging algorithm, which has been applied in the past is an energy-based method (see Section 1.1.2) [11]. In our case, a signal formed from the product of the

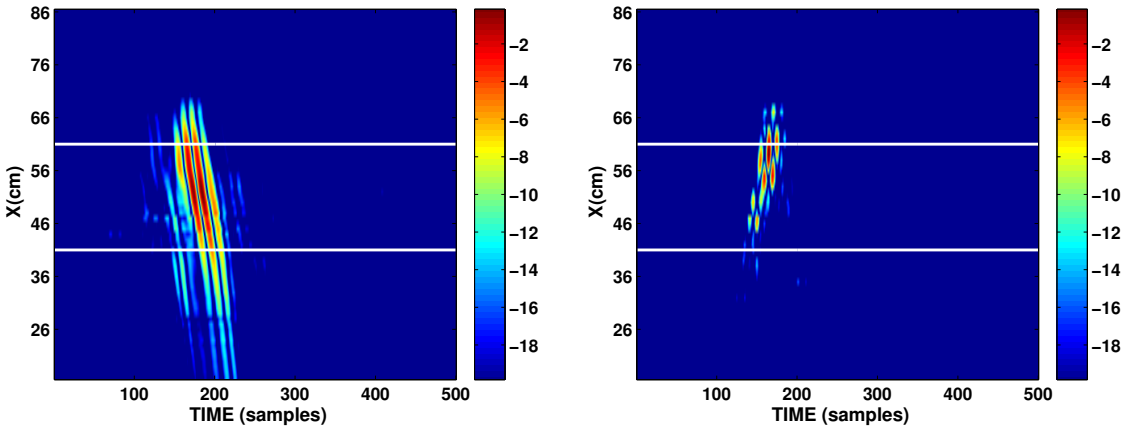

(a) (b)

Figure 80: Imaging of a VS-1.6 mine (20 cm diameter) buried at a depth of 5 cm. Space-time plots (dB scale) of (a) Extracted reflected wave, (b) Product of the extracted reflected wave and the extracted forward wave. Front and back edges of the mine are shown by horizontal white lines.

forward and reflected waves will be used for the energy calculation. At each spatial x position, a window of length N extracts part of the time signal. The center of the time window is based on the time it takes for the Rayleigh wave to travel from the source to the sensor position x. This travel-time calculation requires a group velocity estimate. The group velocity can be calculated directly from the IQML analysis, as given in Section 3.4.2. The estimated group velocity for this example is 81.43 m/sec.

Once we have the group velocity, at each spatial position a window of length N is formed across time, with the center of the window being calculated via:

$$t_c = \frac{D_x}{V_g}, \tag{93}$$

where t_c is the center of the window, V_g the group velocity, and D_x the distance between the source and the sensor position at x. At each spatial position an energy image is formed by:

$$E_x = \sum_{t=t_c-\frac{N}{2}}^{t_c+\frac{N}{2}} y^2(x,t), \tag{94}$$

where y is the signal formed from the product of the extracted forward and reflected waves at each spatial position x. A window of length $N = 40$ is used which corresponds to 5 msec in time. The window at each spatial position along with the center position line is shown

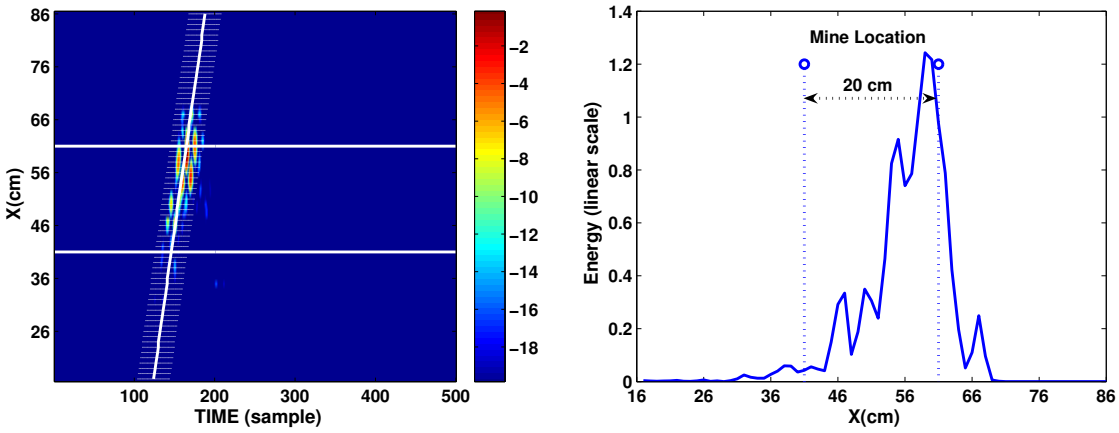

(a) (b)

Figure 81: Energy based algorithm: (a) At each spatial position a window of length 40 across time is applied to the signal obtained from the product of forward and reflected wave (Fig. 80(b)). (b) Energy plot, strongest where the mine is located.

in Fig. 81(a) for all x positions, and the energy calculated is shown in Fig. 81(b). The energy is strongest where the mine is located, thus indicating the spatial position of the mine. Once again, the back edge of the mine gives a stronger response.

In the second experiment, different kinds of mines are buried along with clutter (rocks). The mines are an M-14 buried at 0.5 cm, a VS-1.6 at 5 cm, a Butterfly at 2 cm, a VS-50 at 1.5 cm and a TS-50 at 2 cm. The relative positions and depths of the mines and rocks are shown in Fig. 82. The reflected Rayleigh waves are extracted for three different linear scans across all x positions: scan-1 at $y = 20$ cm, scan-2 at $y = 40$ cm, and scan-3 at $y = 60$ cm. The reflected wave across scan-2 is shown in Fig. 83(a), and we observe three x positions where reflections are strong. In Fig. 83(b) the product of the extracted waves (forward and reflected) is plotted, showing three positions where there are indications of the presence of targets. Similarly, waves extracted across scan-1 and scan-3 positions are shown in Fig. 84. The final image for whole 2-D scan is shown in Fig. 85, clearly indicating the position of all five landmines. There is hardly any indication of the presence of rocks, again verifying the effectiveness of this technique in discriminating mines from clutter.

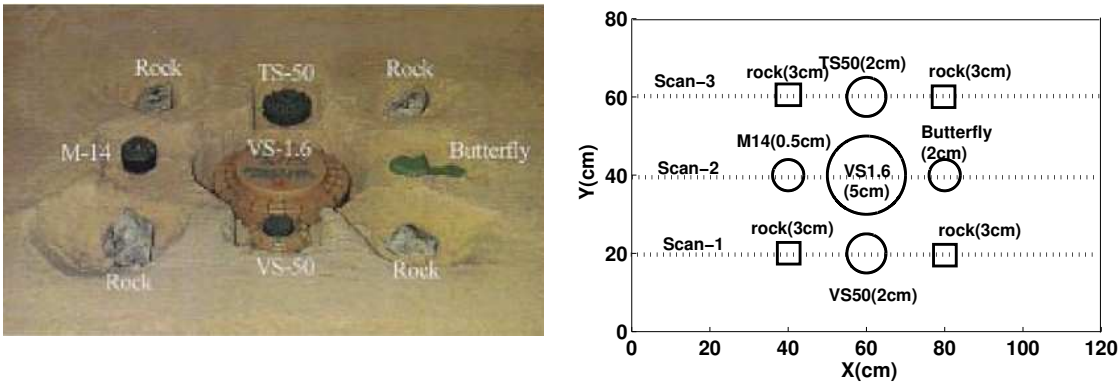

(a) (b)

Figure 82: Experimental setup: (a) Photograph of the mines and rocks prior to burial. (b) Map of the relative positions and depths of the mines and rocks.

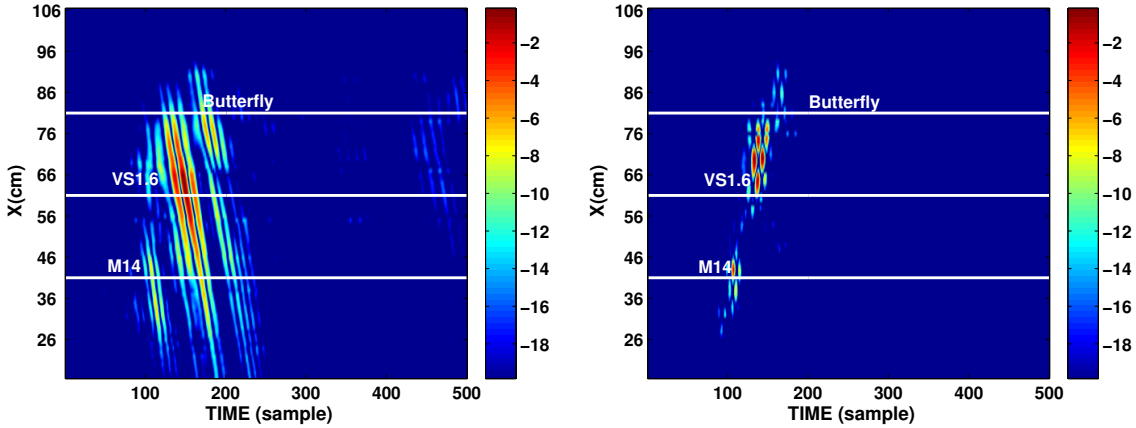

(a) (b)

Figure 83: Space-time plots (dB scale) of the waves along the scan-2 position: (a) Extracted reflected wave, (b) Product of the extracted reflected wave and the extracted forward wave. Positions of the mine centers are denoted by the horizontal lines.

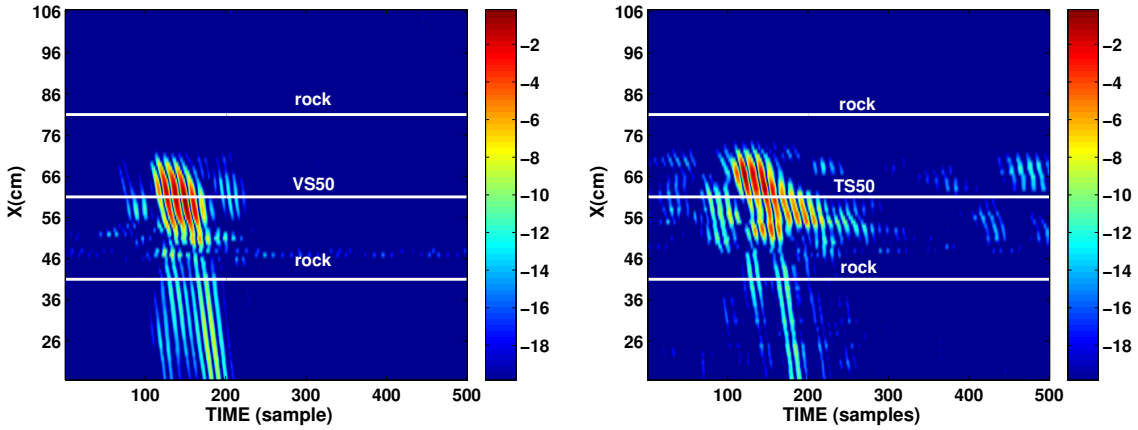

(a) (b)

Figure 84: Space-time plots (dB scale) of the reflected wave extracted via IQML: (a) across scan-1, (b) across scan-3. Positions of the mine centers are denoted by the horizontal white lines.

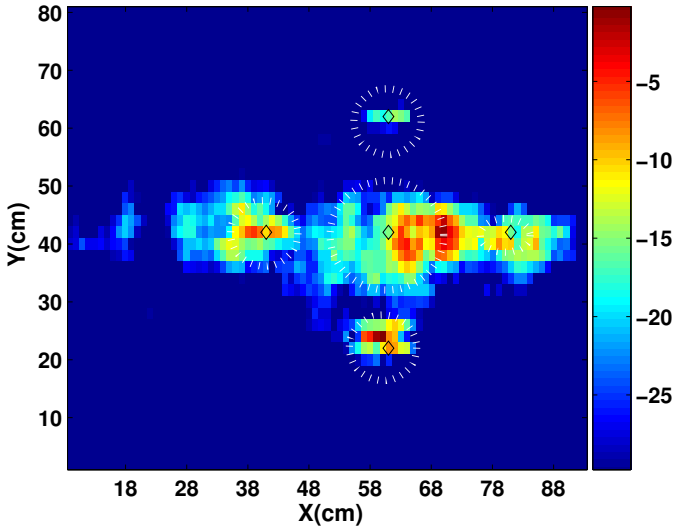

Figure 85: Final image obtained after using all of 2-D scan. Position of mines are indicated by circles (30 dB scale).

7.3 GLRT based Detector Framework

The detector is based on the solution to the problem of detecting an unknown signal in additive noise. Here, we assume that we don't know anything about the signal which we want to detect. The detection problem is generally described by a null hypothesis H_0, where the signal is absent and an alternative hypothesis H_1, where the signal is present [69], i.e.,

$$\begin{aligned} H_0 &: y(l) = n(l) \\ H_1 &: y(l) = s(l) + n(l), \qquad s(l) = ?, l = 1, ..., L \end{aligned} \tag{95}$$

In our case y is the observed signal formed by the product of the extracted forward and reflected waves in a window of length L samples. The noise is assumed to be Gaussian with a covariance matrix K. The conditional probability density function under H_1 is given by

$$p_{\mathbf{y}|H_1,s}(\mathbf{y}) = \frac{1}{\sqrt{|2\pi K|}} \exp\{-\frac{1}{2}(\mathbf{y}-\mathbf{s})^T K^{-1}(\mathbf{y}-\mathbf{s})\} \tag{96}$$

The most popular detector in this case is based on Generalized Likelihood Ratio Test (GLRT) [69]. Under this test the maximum value of the density with respect to the unknown parameters, i.e., the signal values, occurs when $\mathbf{y} = \mathbf{s}$, i.e

$$\max_{\mathbf{s}}\{p_{\mathbf{y}|H_1}(\mathbf{y})\} = \frac{1}{\sqrt{|2\pi K|}} \tag{97}$$

The other model does not depend on the signal, and the GLRT for the unknown signal problem, often termed the square-law detector [33], is

$$\mathbf{y}^T K^{-1} \mathbf{y} \underset{H_0}{\overset{H_1}{\gtrless}} \gamma \tag{98}$$

If the noise is white, a sufficient statistic is the sum of the squares of the observation

$$\Upsilon = \sum_{l=0}^{L-1} y^2(l) \underset{H_0}{\overset{H_1}{\gtrless}} \gamma. \tag{99}$$

If we assume the additive noise is white and Gaussian, with a variance of σ^2, then the sufficient statistic Υ has a probability density given by chi-squared density of degree of freedom L [33]

$$\frac{\Upsilon}{\sigma^2} \sim \chi^2(L), \tag{100}$$

when no signal is present. The threshold γ for this statistic is established by solving $\Pr(\chi^2(L) > \frac{\gamma}{\sigma^2}) = P_{FA}$, for a fixed probability of false alarm. The resulting threshold can then be used in detection by using (99). A regional variance technique is typically used to estimate the noise variance. A guard cell is placed around each test spatial position, and then the noise variance is estimated by using the average of the observed signal power immediately outside the guard region. The guard cell is a rectangular form with the test spatial position at its center. The area outside this guard cell, where the noise power is measured is also a rectangular form surrounding the guard region.

7.4 Experimental Results

7.4.1 Single Target Case

An experiment was performed in a sandbox with a single VS-1.6 (AT) mine buried at a depth of 5 cm. The data is collected over a 2-D grid of size (100×100), covering an area of 1 m^2. One slice of this data set is shown in Fig. 79(a). The first step is to separate the forward and reflected waves by using a spatial window of 31 sensors. Then the imaging algorithm given in the previous section is applied. Figure. 86(a) shows the result of applying the algorithm to the reflected wave only, and Fig. 86(b) is the result using the product of the forward and reflected waves. In the end, the detector is applied and its output is shown in Fig. 86(c), clearly indicating the position of mine.

7.4.2 Multiple Targets in the Presence of Clutter

Another experiment was performed where inert mines and clutter were buried within a scan region of 1.8×1.8 m. The positions of the mines and clutter are shown in Fig. 87(a) [3]. An array of seismic sources is located on one end of the scan region. There are six mines (two AT landmines: VS-1.6 and VS-2.2; four AP mines: TS-50, M-14, VS-50, and PFM-1) and 21 clutter objects such as gun shells, nails, rocks, cans, etc. The result of applying the imaging algorithm is shown in Figs. 87(b,c), where we are able to detect the location of five out of six mines (all except the small M-14). Out of all the clutter objects (other than

[3] Gregg Larson is the creator of Fig. 87(a)

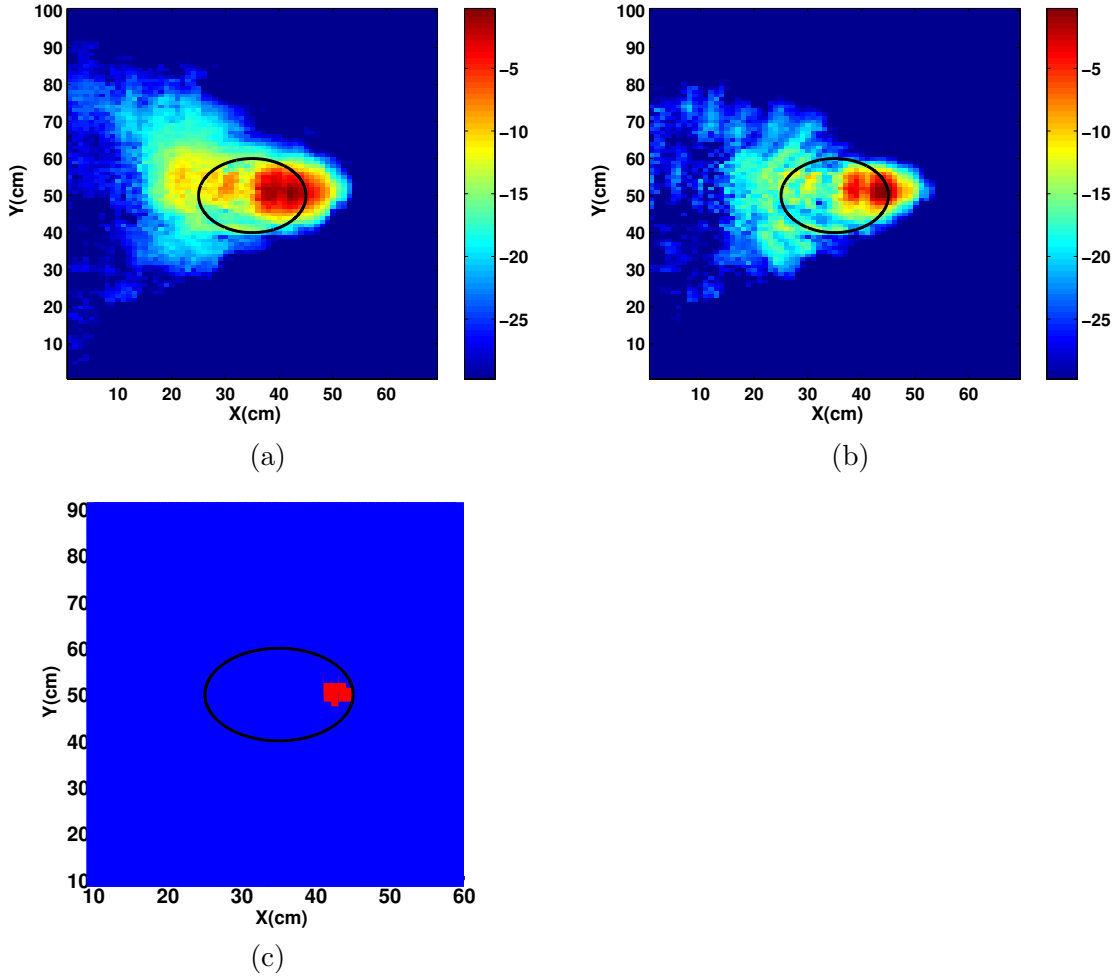

Figure 86: Single VS-1.6 mine buried at a depth of 5 cm. Result of applying the imaging and detection algorithm (30 dB scale). (a) Using only reflected wave. (b) Using both the forward and reflected waves. (c) Detector output (blue = no detection, red = detection), $P_{FA} = 0.1$.

mines) the only things seen in the image and also detected are the two metal soda cans. Using a $P_{FA} = 0.1$, the detector output is shown in Fig. 87(d), clearly indicating the areas with the highest probability of targets.

7.5 Conclusion

In this chapter, a new imaging and detector framework is proposed for final detection stage that would confirm the presence of a landmine. The imaging algorithm uses the waves reflected from the target and also the forward probing pulse. These waves are extracted from the raw collected data. The output of the imaging algorithm can also be used for a detector, whose output is the exact identification of the area with the highest probability of finding landmine. Both algorithms were tested for detecting mines in the presence of different types of clutter (both man-made and natural), and they perform satisfactorily in these difficult cases.

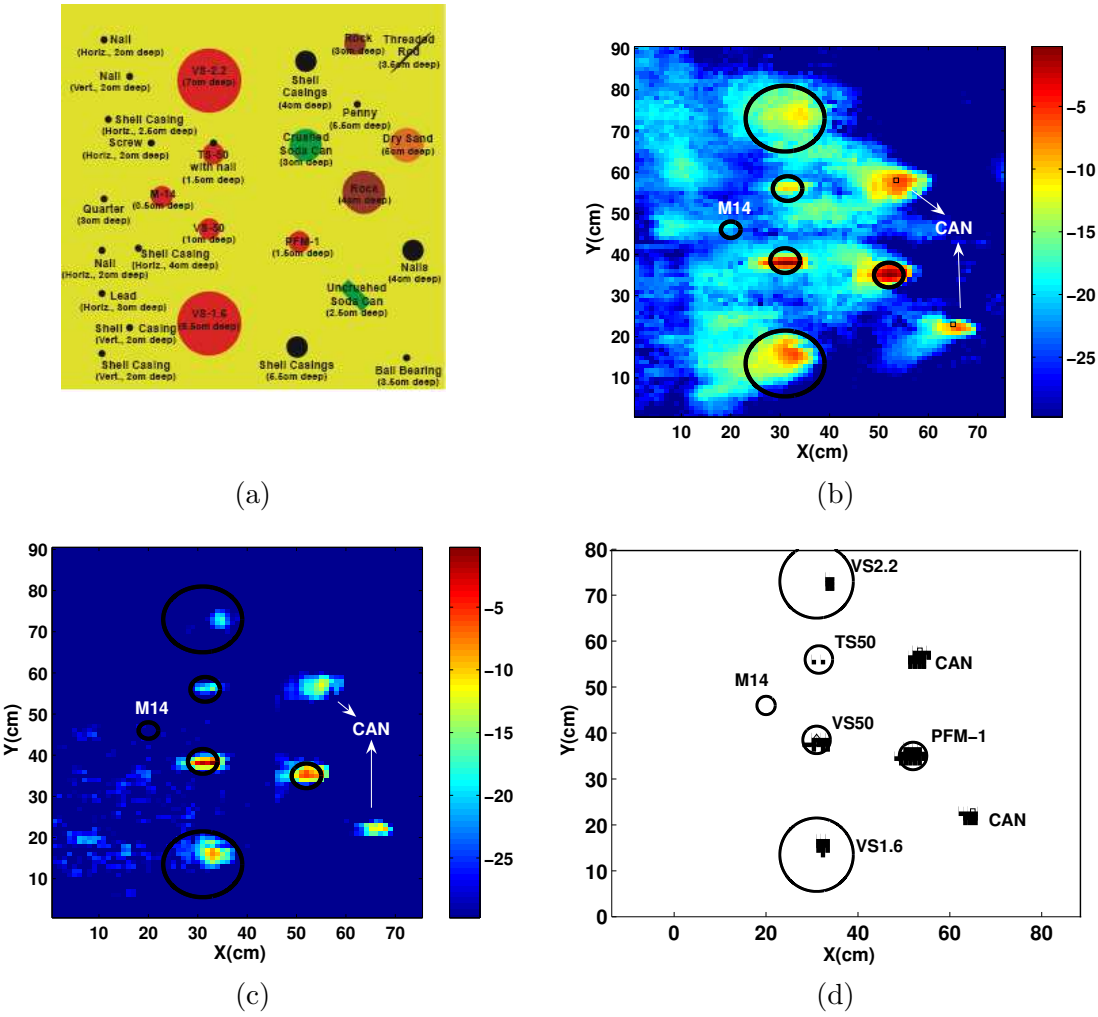

Figure 87: Multiple targets in the presence of clutter (Positions of mines are shown by circles, all the images are at 30 dB scale). (a) Experimental setup showing positions of the mines and clutter. (b) Using only the reflected wave. (c) Using both the forward and reflected waves. (d) Detector output (white = no detection, black = detection).

CHAPTER VIII

CONCLUSIONS

One of the most deadly legacies of the 20th century is the use of landmines in warfare. Anti-personnel landmines continue to have tragic, unintended consequences years after a battle and even after the entire war has ended. As time passes, the location of landmines is often forgotten, even by those who deployed them. These mines continue to be functional for many decades, causing further damage, injury and death. Landmines are basically explosive devices that are designed to explode when triggered by pressure or a tripwire. These devices are typically found on or just below the surface of the ground. The purpose of mines when used by armed forces is to disable any person or vehicle that comes into contact with it by an explosion or fragments released at high speeds. Currently, there are more than 100-million landmines located in 70 countries around the world. Since 1975, landmines have killed or maimed more than 1-million people, which has led to a worldwide effort to ban further landmine use and clear away existing landmines [50].

There is a growing worldwide effort to rid the world of landmines. To do this, we must first locate the millions of landmines that are still buried in dozens of countries around the world. Finding these landmines is extremely difficult, as most mine fields are unmarked. And those that are marked can take years to de-mine. Landmine detection is a slow, methodical process due to the danger involved in locating landmines. There are various techniques available which rely on both human probing and some use of sensors. Various types of sensors include metal detectors (EMI), ground penetrating radars (GPR), thermal neutron sensors (TNA), infrared (IR), chemical, and seismic sensors, etc. Among all these methods, seismic sensing seems to be the most promising. However, one drawback of this technique is that it is slow, time consuming and requires a large number of measurements to make the final detection and confirmation.

In this thesis, we have proposed and implemented a complete landmine detection system using seismic waves. The ability of seismic waves to discriminate between man-made targets and naturally occurring clutter such as rocks, give this method a great advantage as compared to other existing techniques. To reduce the number of measurements and processing time, we have introduced an algorithm for optimal maneuvering of seismic sensors. The algorithm for optimal maneuvering requires three main steps, as described in the previous chapters. The first step deals with seismic wave identification and separation, the second with data models and imaging, and the third with optimal maneuvering to increase the effective aperture of seismic array. For the first step, a new spatial spectrum analysis technique for surface waves was presented in Chapter 3. A parametric model was derived, and the Prony-based algorithm was presented for estimating the parameters of this model. The algorithm was also extended to a multi-channel case, which is useful in predicting the polarization behavior of the surface waves. The various modes of the surface waves could be identified and their parameters could be extracted. These various modes could also be reconstructed again in the time domain. The spectrum analysis technique can also be used to separate the forward and reflected waves in the case of buried targets. The extracted reflected wave can be used to determine the location of the target.

Two new imaging algorithms were proposed in Chapter 4 for the case of fixed linear arrays. One algorithm is based on the near field DOA and range estimates, using a 2-D MUSIC algorithm; the second on the CLEAN/RELAX algorithm. The performance of both algorithms is satisfactory in locating the targets, except that both require a large number of measurements. In order to reduce the number of measurements, an algorithm for optimal maneuvering was proposed in Chapter 5 and its implementation was presented in Chapter 6. The idea is to place the sensors on a mobile platform that is capable of sensing the environment on its own. However, to perform this autonomous maneuvering new algorithms are required. The data model, the algorithm for estimating target positions, and the performance bounds for these position estimates were derived. Next, based on the position estimates and performance bounds, the algorithm for optimal maneuvering was presented. Two constraints for the movement were also defined from the physics of

problem. All the algorithms were tested by using experimental data collected in a laboratory setting. To make a working system robust for realistic situations, a multi-mode algorithm was presented. Cases with single and multiple targets were presented. A strategy to handle multiple targets, that handle one target at a time was also presented. The performance of the algorithm was tested in the presence of common types of clutter such as rocks, and also for conditions where there is a large scale change in the propagation properties of the medium. The mechanism seems to be robust, with ability to locate the targets within a few iterations, with considerable reduction in time and the number of measurements. Finally, in Chapter 7, an imaging and detector framework for confirmation was presented. In this step, the signature of mines in terms of reflection/resonance is extracted, and used to make the final decision. This imaging algorithm and detector framework was tested out in various burial scenarios with different mines and clutter.

REFERENCES

[1] Alam, M., Cevher, V., and McClellan, J. H., "Optimal experiments with seismic sensors." Accepted in Proc. of IEEE International Conference on Acoustics, Speech, and Signal Processing (ICASSP2006), 2006.

[2] Alam, M., Cevher, V., and McClellan, J. H., "Optimal maneuvering of seismic sensors for localization of subsurface targets." Submitted to IEEE Trans. on Geosciences and Remote Sensing, 2006.

[3] Alam, M., Larson, G., McClellan, J. H., and Scott, W., "Optimal experiments with seismic sensors for the localization of buried landmines." Accepted in Proc. of SPIE:Defense and Security Symposium, 2006.

[4] Alam, M. and McClellan, J. H., "Imaging and detector framework for seismic landmine detection," in *Accepted in Fourth IEEE Workshop on Sensor Array and Multi-channel Processing (SAM-2006)*, (Waltham Massachusetts), 2006.

[5] Alam, M., McClellan, J. H., and Scott, W., "Spectrum analysis of seismic surface waves and its applications in seismic landmine detection." Submitted to J. Acoust. Soc. Am (JASA), 2006.

[6] Alam, M. and McClellan, J. H., "Near field imaging of subsurface targets using active arrays and elastic waves," in *Proc. 11th IEEE Digital Signal Processing Workshop*, (Taos ski valley, NM,USA), August 2004.

[7] Alam, M. and McClellan, J. H., "Near field imaging of subsurface targets using wide-band multi-static relax/clean algorithms," in *Proc.IEEE International Conference on Acoustics, Speech, and Signal Processing (ICASSP2005)*, (Philadelphia,PA,USA), March 2005.

[8] Alam, M., McClellan, J. H., Norville, P., and Scott., W., "Time-reverse imaging for the detection of landmines," in *Proc. of SPIE:Defense and Security Symposium*, vol. 5415, (Orlando, Florida,USA), April 2004.

[9] Alam, M., McClellan, J. H., and Scott, W., "Multi-channel spectrum analysis of surface waves," in *Proc. 37th Asilomar Conference on Signals, Systems, and Computers*, (Pacific Grove,Ca,USA), November 2003.

[10] Begot, S., Voisin, E., Artioukhine, E., , and Kauffmann, J., "D-optimal experimental design applied to linear magnetostatic inverse problem," *IEEE Trans. on Magnetics*, vol. 38, pp. 1065–1068, March 2002.

[11] Behoodian, A., McClellan, J. H., and Scott, W., "Signal processing of elastic surface waves for localizing landmines," in *Proc. 33th Asilomar Conference on Signals, Systems, and Computers*, (Pacific Grove,Ca,USA), November 1999.

[12] Bleistein, N., Cohen, J., and Stockwell, J. W., *Mathematics of Multidimensional Seismic Imaging, Migration, and Inversion*. Springer, 2001.

[13] Borcea, L., Papanicolaou, G., Tsokgka, C., and Berryman, J., "Imaging and time reversal in random media," *Inverse Problems*, vol. 18, pp. 1247–1279, 2002.

[14] Bresler, Y. and Macovski, A., "Exact maximum likelihood parameter estimation for superimposed exponential signals in noise," *IEEE Trans. on Acoust., Speech, Signal Processing.*, vol. 34, pp. 1081–1089, Oct 1986.

[15] Campman, X., Wijk, K., Scales, C., and Herman, G., "Imaging scattered seismic surface waves," *Near Surface Geophysics*, vol. 2, pp. 223–230, November 2004.

[16] Capon, J., "High resolution frequency-wavenumber spectrum analysis," *Proc. IEEE*, vol. 57, pp. 1408–1418, 1969.

[17] Cevher, V., *A Bayesian framework for target tracking using acoustic and image measurements*. PhD thesis, School of Electrical and Computer Engineering, Georgia Institute of Technology, Atlanta,Ga,USA, 2005.

[18] Cevher, V. and McClellan, J. H., "Acoustic node calibration using a moving source." Accepted in IEEE Trans. on Antennas and Propagation, 2005.

[19] Claerbout, J., *Fundamentals of Geophysical Data Processing*. McGraw-Hill, 1976.

[20] Dudgeon, D. E. and Mersereau, R. M., *Multidimensional Digital Signal Processing*. Prentice-Hall, 1984.

[21] et. al. Smith., "Measurement and localization of interface wave reflections from a buried target," *J. Acoust. Soc. Am.(JASA)*, vol. 103, 1998.

[22] et. al. Stotts., "Source bearing determination from a tri-axial seismometer using rayleigh wave propagation," *J. Acoust. Soc. Am.*, vol. 115, 2004.

[23] Feforov, V., *Theory of Optimal Experiments*. SIAM, 1972.

[24] Fink, M., "Time reversal of ultrasonic fields-parti:basic principles," *IEEE Trans. on Ultrason. Ferroelec. Freq. Control*, vol. 39, pp. 555–566, May 1992.

[25] Fink, M., Prada, C., Wu, F., and Cassereau, D., "Self focusing in inhomogeneous media with time reverse acoustic mirrors," in *Proc. of IEEE Ultrasonic Symoposium*, vol. 2, pp. 681–686, 1989.

[26] Foti, S., *Multistation methods for geotechnical characterization using surface waves*. PhD thesis, Politecnico di Torino,Italy, 2000.

[27] Gini, F., Lombardini, F., and Montanari, M., "Layover solution in multibaseline sar interferometry," *IEEE Trans. on Aerospace and Electronic Systems*, vol. 38, pp. 1344–1356, Oct 2002.

[28] Hayes, M. H., *Statistical Digital Signal Processing and Modeling*. John Wiley and Sons, 1996.

[29] HöGBOM, J., "Aperture synthesis with a non-regular distribution of interferometer baselines," *Astron. Astrophys. Suppl. Ser.*, vol. 15, pp. 417–426, 1974.

[30] HELFERTY, J. and MUDGETT, D., "Optimal observer trajectories for bearings only tracking by minimizing the trace of the cramer-rao lower bound," in *Proc. 32nd IEEE Conference on Decision and Control*, (San Antonio,TX,USA), pp. 936–939, Dec 1993.

[31] HELFERTY, J., MUDGETT, D., DZIELSKI, J., and KAUFFMANN, J., "Trajectory optimization for minimum range error in bearings-only source localization," in *Proc. Engineering in Harmony with Ocean*, vol. 2, (Victoria ,BC,Canada), pp. 229–234, October 1993.

[32] HUANG, Y. and BARKAT, M., "Near-field multiple source localization by passive sensor array," *IEEE Trans. on Antennas Propagation*, vol. 39, pp. 968–974, July 1991.

[33] JOHNSON, D., "Unknown signal waveform." Connexions(http://cnx.rice.edu/content/m11284/latest/).

[34] JOHNSON, D. and DUDGEON, D., *Array Signal Processing:Concepts and Techniques*. Englewood Cliffs, NJ: Prentic Hall, 1993.

[35] KOMILIKIS, S., PRADA, C., WU, F., and FINK, M., "Characterization of extended objects with d.o.r.t. method," in *Proc. of IEEE Ultrasonic Symoposium*, vol. 2, pp. 1401–1404, 1996.

[36] LAI, C. and RIX, G., "Simultaneous inversion of rayleigh phase velocity and attenuation for near-surface site characterization," tech. rep., Georgia Institute of Technology, School of Civil and Environmental Engineering, 1998.

[37] LAI, C. and RIX, G., "Solution of the rayleigh eigenproblem in viscoelastic media," *Bulletin of the Seismological Soc. of Am.*, vol. 92, pp. 2297–2309, June 2002.

[38] LAI, C. G., *Simultaneous inversion of Rayleigh phase velcoity amd attenuation for near-surface charaterization*. PhD thesis, School of Civil Engineering,Georgia Institute of Technology, Atlanta,Ga,USA, 1998.

[39] LANG, S., KURKJIAN, A., MCCLELLAN, J., MORRIS, C., and PARKS, T., "Estimating slowness dispersion from arrays of sonic logging waveforms," *Geophysics*, vol. 52, pp. 530–544, April 1987.

[40] LANTERMAN, A. D., "Signal detection and estimation." Class Notes, Spring 2002,Georgia Institute of Technology.

[41] LARSON, G., ALAM, M., MARTIN, J., SCOTT, W., MCCLELLAN, J., MCCALL, G., NORVILLE, P., and DECLETY, B., "Surface-wave-based inversions of shallow seismic structure," in *Proc. of SPIE:Defense and Security Symposium*, vol. 5089, (Orlando, Florida,USA), April 2003.

[42] LEHMAN, S. and DEVANEY, A., "Transmission mode time-reversal super-resolution imaging," *J. Acoust. Soc. Am.(JASA)*, vol. 113, pp. 2742–2753, 2003.

[43] LI, J. and STOICA, P., "Efficient mixed-spectrum estimation with applications to target feature extraction," *IEEE Trans. on Signal Processing.*, vol. 44, pp. 1081–1089, Feb 1996.

[44] Li, J., Stoica, P., and Zheng, D., "Angle and waveform estimation via relax," *IEEE Trans. on Aerosp. Electron. Syst.*, vol. 33, pp. 1077–1087, July 1997.

[45] Liao, X. and Carin, L., "Application of the theory of optimal experiments to adapative electromagnetic-induction sensing of buried targets," *IEEE Trans. on Pattern Analysis and Machine Intelligence*, vol. 26, pp. 961–972, August 2004.

[46] Marple, S. L., *Digital Spectral Analysis with Applications*. Englewood Cliffs, NJ: Prentic Hall, 1987.

[47] McClellan, J. H., "Two-dimensional spectrum analysis in sonic logging," in *Proc. International Conference on Acoustic, Speech, and Signal Processing*, (Toyko,Japan), pp. 3105–3111, 1986.

[48] McClellan, J. and Lee, D.-W., "Exact equivalence of the steiglitz-mcbride iteration and iqml," *IEEE Trans. on Signal Processing*, vol. 39, no. 2, pp. 509–512, 1991.

[49] Moon, T. and Stirling, W., *Mathematical Methods and Algorithms for Signal Processing*. Prentice Hall, 1999.

[50] Nations, U., "Assistance in mine clearance: Report of the secretary-general," tech. rep., United Nations, 1994.

[51] NAZARIAN, S., *In situ determination of elastic moduli of soil deposits and pavement systems by spectral-analysis-of-surface waves method*. PhD thesis, School of Civil Engineering, University of Texas at Austin, Austin,Tx,USA, 1984.

[52] Norville, P. and Jr, W. S., "Time-reversal focusing of elastic surface waves," *J. Acoust. Soc. Am.(JASA)*, vol. 118, Dec 2005.

[53] Poor, H., *An Introduction to Signal Detection and Estimation*. Springer-Verlag, 1994.

[54] Prada, C., Manneville, S., Sponlianisky, D., and Fink, M., "Decomposition of the time reversal operator: Detection and selective focusing on two scatterers," *J. Acoust. Soc. Am.*, vol. 97, pp. 62–71, 1996.

[55] Prada, C., Thomas, J., and Fink, M., "The iterative time reversal process: Analysis of the convergence," *J. Acoust. Soc. Am.*, vol. 97, pp. 62–71, 1995.

[56] Prada, C. and Thomas, J., "Experimental subwavelength localization of scatterers by decomposition of the time reversal operator interpreted as a covariance matrix," *J. Acoust. Soc. Am.*, vol. 114, pp. 235–243, 2003.

[57] Pukelsheim, F., *Optimal Design of Experiments*. Wiley Series, 1993.

[58] Sabatier, J. and Xiang, N., "An investigation of acoustic-to-seismic coupling to detect buried antitank landmines," *IEEE Trans. on Geoscience and Remote Sensing.*, vol. 39, pp. 1146–1154, June 2001.

[59] Schmidt, R., "Multiple emitter location and signal parameter estimation," *Proc. RADC Spectral Estimation Workshop*, pp. 243–258, 1979.

[60] Schröder, C. and Jr, W. S., "On the complex conjugate roots of the rayleigh equation: The leaky surface wave," *J. Acoust. Soc. Am.(JASA)*, vol. 110, Jan 2001.

[61] Schröder, C., *On the interaction of elastic waves with buried landmines: An investigation using the Finite-Difference Time-Domain*. PhD thesis, School of Electrical and Computer Engineering,Georgia Institute of Technology, Atlanta,Ga,USA, 2000.

[62] Scott, W., Larson, G. D., Martin, J., and McCall, G. S., "Field testing and development of a seismic landmine detection system," in *Proc. of SPIE:Defense and Security Symposium*, vol. 5089, (Orlando, Florida,USA), April 2003.

[63] Scott, W., Martin, J., and Larson, G., "Experimental model for a seismic landmine detection system," *IEEE Trans. on Geoscience and Remote Sensing*, vol. 39, pp. 1155–1164, June 2001.

[64] Smith, P. and Krumhansl, P., "Feasibility of seismic landmine detection," Tech. Rep. 7677, BBN System and Technologies, 1992.

[65] Staelin, D., Morgenthalers, A., and Kong, J., *Electromagnetic Waves*. Prentice-Hall, 2001.

[66] Steiglitz, K. and McBride, L. E., "A technique for the identification of linear systems," *IEEE Trans. on Auotomat. Contr.*, vol. 10, pp. 461–464, Oct 1965.

[67] Stoica, P. and Moses, R., *Introduction to Spectral Analysis*. Prentice Hall, 1997.

[68] Swindlehurst, A. and Kailath, T., "Passive direction-of-arrival and range estimation for near-field sources," in *Proc. of Fourth Annual ASSP Workshop on Spectrum Estimation and Modeling*, pp. 123–128, August 1988.

[69] Van-Trees, H. L., *Detection, Estimation, and Modulation Theory : Vol. 1*. Wiley, NY, 1971.

[70] Wang, Y., Li, L., Stoica, P., Sheplak, M., and Nishida, T., "Wideband relax and wideband clean for aeroacoustic imaging," *J. Acoust. Soc. Am.(JASA)*, vol. 115, pp. 757–767, Feb 2004.

[71] Zhou, Y., Porat, B., , and Nehorai, A., "Localizing vapor-emitting sources by moving sensor," *IEEE Trans. on Signal Processing*, vol. 44, pp. 2655–2666, May 1996.

[72] Zhou, Y., Yip, P., and Leung, H., "Tracking the direction-of-arrival of multiple moving targets by passive arrays:algorithms," *IEEE Trans. on Signal Processing*, vol. 47, pp. 2655–2666, Oct 1999.

[73] Zywicki, D., *Advanced signal processing methods applied to engineering analysis of seismic surface waves*. PhD thesis, School of Civil Engineering,Georgia Institute of Technology, Atlanta,Ga,USA, 1999.

VITA

Mubashir Alam was born in Abbottabd, Pakistan, in March 1972. He received his B.Sc Degree in Electrical Engineering from N.W.F.P University of Engineering and Technology, Peshawar, Pakistan, in 1996. He was awarded Quaid-i-Azam Scholarship, by Govt. of Pakistan for his higher studies in USA in Electrical Engineering. He completed his MSECE from Georgia Tech in 2000, and will receive his PhD degree in Electrical Engineering from Georgia Institute of Technology in Summer, 2006. His research interests are in array processing, seismic signal processing, statistical signal processing and wireless sensor networks. He was involved in DARPA-ARO MURI project titled, "Multi-Modal Inverse Scattering for Detection and Classification Of General Concealed Targets".